Diss. ETH No 11041

Production of $D^{*\pm}$ Mesons Measured with the H1 Detector at HERA

A dissertation submitted to the

SWISS FEDERAL INSTITUTE OF TECHNOLOGY ZURICH

for the degree of
Doctor of Natural Sciences

presented by

Roland Bernet
Dipl. Phys. ETH Zürich
born July 5, 1964
citizen of Alberswil/LU

Accepted on the recommendation of

Prof. Dr. R. A. Eichler, examiner
Prof. Dr. F. Pauss, co-examiner

1995

Contents

Abstract

In the electron-proton scattering at HERA the charm quarks are produced by the photoproduction process of photon gluon fusion. The cross section depends on the gluon density function of the proton.

In this work a method is investigated to determined the charm production cross section using the decay chain $D^0 \longrightarrow K^0_S \pi^+\pi^-$ with $K^0_S \longrightarrow \pi^+\pi^-$. To achieve a better signal to noise ratio the D^0 mesons are tagged with the decay $D^{*\pm} \longrightarrow D^0\pi^\pm_s$ by measuring the invariant mass difference of the $D^{*\pm}$ meson and the D^0 meson. The charged decay products are measured in the central jet chambers of the H1 detector.

An important part of the procedure of obtaining a cross section is to understand the trigger efficiency. Therefore the drift chamber r-φ trigger performance is studied carefully.

The data used for this analysis were collected in the run period of 1993 and correspond to a total integrated luminosity of 319 nb^{-1}. The obtained charm production cross section is

$$\sigma\,(ep \longrightarrow ec\bar{c}X) \quad = \quad 1.62 \pm 0.87_{\mathrm{stat.}} \pm 0.62_{\mathrm{syst.}}\ \mu\mathrm{b} \quad .$$

Using the Weizsäcker-Williams approximation the corresponding photoproduction cross section can be calculated, and yields

$$\sigma\,(\gamma p \longrightarrow c\bar{c}X) \quad = \quad 12.6 \pm 7.1_{\mathrm{stat.}} \pm 5.2_{\mathrm{syst.}}\ \mu\mathrm{b} \quad .$$

In the appendix the hardware of the drift chamber r-φ trigger of the H1 experiment is described.

Zusammenfassung

In der Elektron-Proton Streuung bei HERA werden die Charm-Quarks durch den Photoproduktionsprozess Photon-Gluon-Fusion produziert. Der Wirkungsquerschnitt ist von der Gluonendichtefunktion des Protons abhängig.

In dieser Arbeit wird eine Methode zur Bestimmung des Wirkungsquerschnitts der Charmproduktion untersucht, der die Zerfallskette $D^0 \longrightarrow K_S^0\pi^+\pi^-$ mit $K_S^0 \longrightarrow \pi^+\pi^-$ benutzt. Um das Verhältnis zwischen Signal und Untergrund zu verbessern, werden die D^0 Mesonen mit dem Zerfall $D^{*\pm} \longrightarrow D^0\pi_s^\pm$ durch die Messung der invarianten Massendifferenz von $D^{*\pm}$ Meson und D^0 Meson ausgewählt. Die geladenen Spuren der Zerfallsprodukte werden in den zentralen Jetkammern des H1 Detektors nachgewiesen.

Ein wichtiger Teil der Wirkungsquerschnittsbestimmung ist das Verständnis der Triggereffizienz. Deshalb wird die Funktionstüchtigkeit des Driftkammer r-φ Triggers genau untersucht.

Die für diese Analyse verwendeten Daten wurden in der Strahlperiode von 1993 aufgezeichnet und entsprechen einer integrierten Luminosität von 319 nb^{-1}. Der daraus erhaltene Produktionswirkungsquerschnitt für Charm-Quarks ist

$$\sigma(ep \longrightarrow ec\bar{c}X) \quad = \quad 1.62 \pm 0.87_{\mathrm{stat.}} \pm 0.62_{\mathrm{syst.}}\ \mu\mathrm{b} \quad .$$

Unter Verwendung der Weizsäcker-Williams Approximation kann der entsprechende Photoproduktionswirkungsquerschnitt berechnet werden. Er beträgt

$$\sigma(\gamma p \longrightarrow c\bar{c}X) \quad = \quad 12.6 \pm 7.1_{\mathrm{stat.}} \pm 5.2_{\mathrm{syst.}}\ \mu\mathrm{b} \quad .$$

Im Anhang wird die Elektronik des Driftkammer r-φ Triggers des H1 Experiment beschrieben.

1 Physics at HERA

The electron-proton storage ring HERA at DESY is the first accelerator in which 820 GeV protons collide with 26.7 GeV electrons at a center of mass energy of 296 GeV. Therefore it is possible to study deep inelastic scattering over a much larger kinematical range in the square of the four momentum transfer Q^2 as well as in *x-Bjorken* compared to measurements of previous fixed target experiments. At small Q^2 the exchange of quasi-real photons dominates electron proton scattering. The photoproduction at very high center of mass energies of the γp system can be studied within included a large charm production cross section, which is determined in this work.

1.1 Kinematics at HERA

The incoming electron scatters with the proton by exchanging a gauge boson and converts to a charged or uncharged lepton on the charge of the gauge boson. In deep inelastic scattering the proton is not conserved. Its partons form a hadronic final state X which can include jets. If the gauge boson is an uncharged γ or Z^0 the event is called a neutral current (NC) event. The lepton in the final state is an electron which can be measured in the detector. In the case of an exchange of a gauge boson W^- the event is called a charged current (CC) event and the lepton in the final state is a neutrino which cannot be directly measured in the detector.

$$\begin{array}{lcccc} \mathrm{NC} & : & e^-p & \longrightarrow & e^-X \\ \mathrm{CC} & : & e^-p & \longrightarrow & \nu_e X \end{array}$$

The two event types are shown in Figure 1.

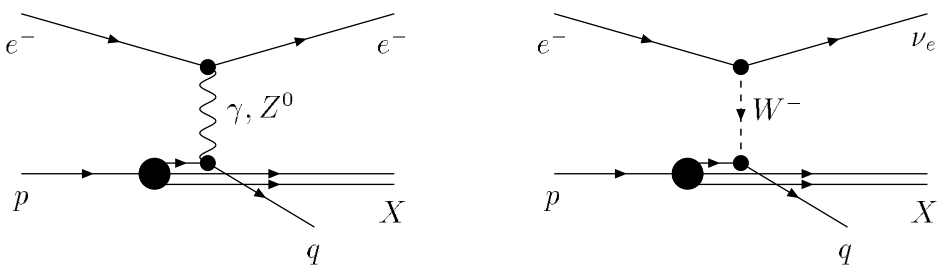

Neutral current   Charged current

Figure 1: Neutral and charged current ep scattering.

The kinematics of the ep scattering is fully determined by two kinematical variables at a fixed known center of mass energy $\sqrt{s}$ of the ep system. Two of the following Lorentz invariant quantities are most frequently used:

- The center of mass energy $\sqrt{s}$ of the ep system

$$s \equiv (p_e + p_p)^2 \approx 4E_eE_p \tag{1}$$

where p_e and p_p are the momenta and E_e and E_p the energies of the electron and the proton.

- The four momentum transfer Q of the gauge boson, which describes its virtuality,

$$Q^2 \equiv -q^2 = -(p_e - p_{l'})^2 \approx 2p_e p_{l'} \quad . \tag{2}$$

- The invariant mass W of the hadronic final state X

$$W^2 \equiv (q + p_p)^2 = m_p^2 + q^2 + 2p_p q \quad . \tag{3}$$

- The energy transfer ν in the proton rest frame

$$\nu \equiv \frac{q \cdot p_p}{m_p} \quad . \tag{4}$$

Another frequently used way to describe the ep system is to use the dimensionless scaling variables x and y. They are defined as follow

$$x \equiv \frac{Q^2}{2\,(q \cdot p_p)} = \frac{Q^2}{2m_p \nu} \tag{5}$$

$$y \equiv \frac{q \cdot p_p}{p_e \cdot p_p} = \frac{\nu}{\nu_{\mathrm{max}}} \quad . \tag{6}$$

The variable x is the Bjorken scale variable [1]. It describes the fraction of the proton momentum the elastic scattered parton carries in the infinite momentum frame, where the proton recoils with high momentum against the electron. The inelasticity of the scattering is described by y, which is equal to the ratio of the actual to the maximum energy transfer in the proton rest frame. Both quantities range from 0 to 1. Neglecting the masses of electron and proton, the variables x and y are connected as follows

$$Q^2 = x \cdot y \cdot s \quad . \tag{7}$$

The squared invariant mass of the hadronic final state W^2 is given by

$$W^2 = Q^2 \cdot \frac{1-x}{x} + m_p^2 \quad . \tag{8}$$

In 1993, the energies at HERA reached $E_p = 820$ GeV and $E_e = 26.7$ GeV corresponding to a center of mass energy $\sqrt{s} = 296$ GeV and a square of maximum four momentum transfer $Q^2_{\mathrm{max}} = 87567\ \mathrm{GeV}^2/c^2$.

There are different procedures to experimentally determine these variables. In NC events the kinematics can be calculated by measuring the polar angle ϑ_e of the scattered electron with respect to the outgoing proton direction and the energy of the scattered electron E'_e

$$y_e = 1 - \frac{E'_e}{E_e} \cdot \sin^2\left(\frac{\vartheta_e}{2}\right) \tag{9}$$

$$Q_e^2 = 4E_eE_e' \cdot \cos^2\left(\frac{\vartheta_e}{2}\right) \quad . \tag{10}$$

Another procedure, independent of the measurement of the electron, is the method of Jacquet-Blondel [2]. It is based on the measurement of the hadronic final state. It is used for CC events and for events where the electron escapes detection or is measured only with a poor resolution

$$y_{\mathrm{JB}} = \frac{1}{2E_e} \cdot \sum_{\text{hadrons } i} (E_i - p_{z_i}) \tag{11}$$

$$Q^2_{\mathrm{JB}} = \frac{1}{1-y_{\mathrm{JB}}}\left(\sum_{\text{hadrons } i} \vec{p_{t_i}}\right)^2 \quad . \tag{12}$$

The summation includes all hadrons measured in the detector. The variables E_i, p_{z_i} and p_{t_i} are the energy, the longitudinal and transverse momenta of the hadron i.

1.2 Photoproduction

1.2.1 General View

The ep scattering at HERA is dominated by quasi-real photons with small four momentum transfer ($Q^2 \approx 0$). The incoming electron is scattered through a large polar angle ϑ. In this case the approximation

$$E_\gamma = y \cdot E_e \tag{13}$$

with

$$y = 1 - \frac{E_e'}{E_e} \tag{14}$$

is valid. The high center of mass energy $\sqrt{s_{ep}} = 296$ GeV of the ep system allows the study of photoproduction in a new kinematical region which lies about one to two magnitudes higher than at fixed target experiments. γp scatterings with a center of mass energy of 150 GeV $\leq \sqrt{s_{\gamma p}} \leq$ 250 GeV are observable. This corresponds to a scattering of 20 TeV photons with a fixed proton target.

The interaction of the photons with protons leads to soft scattering processes where the transverse momentum of the produced particles is very small ($p_t \ll 1$ GeV$/c$) as well as to hard scattering processes where jets with transverse momentum above 10 GeV$/c$ can occur. Until now it has not been possible to find a uniform description for all transverse momentum regions. The photoproduction at HERA is described by three different components (Figure 2):

- **VDM component:** The phenomenological vector dominance model (VDM)[3, 4] is needed to describe processes with small transverse momentum ($p_t \leq 1$ GeV$/c$). The photon fluctuates in a bound virtual $q\bar{q}$ state, a vector meson V with the same quantum numbers as the photon ($J^{PC} = 1^{--}$) — predominantly a ρ^0, ω or ϕ meson — which interacts with the proton. The mediating particle between the proton p and the vector meson V is believed to be in leading order a socalled pomeron $I\!P$, a particle with the quantum numbers of the vacuum. The VDM contains the following parts:

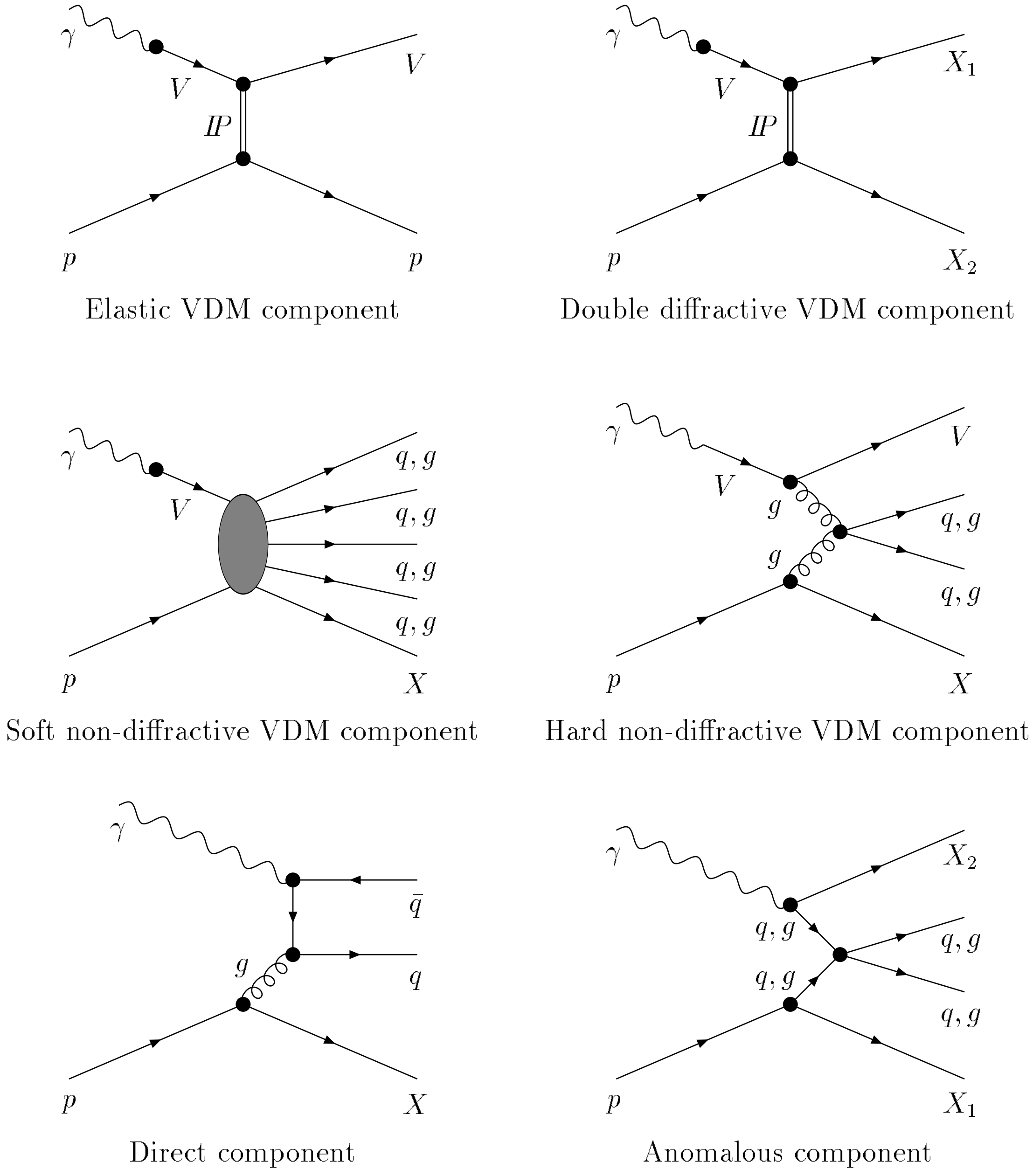

Figure 2: Components of photoproduction: VDM component — elastic and diffractive, soft and hard non-diffractive —, direct component, and anomalous component.

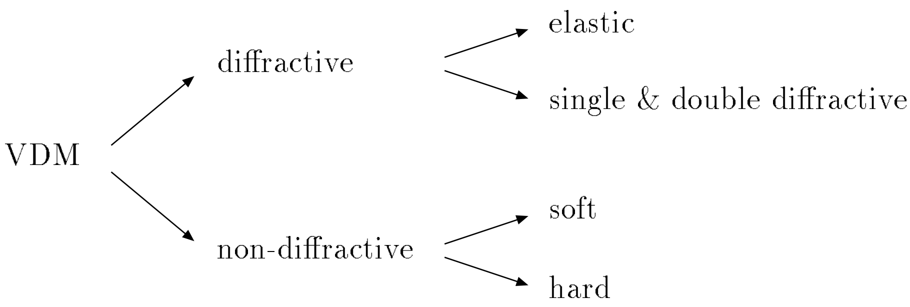

The VDM was successfully used to describe the transverse momentum spectra of particles from $p\bar{p}$ collisions. The hard VDM component reaches transverse momenta above 10 GeV/c at center of mass energies compatible to HERA.

- **Direct component:** The photon interacts as a point like gauge boson. In the photon gluon fusion (PGF) light quark pairs which generate jets, as well as heavy $c\bar{c}$ or $b\bar{b}$ quarks can be produced. Such processes with higher transverse momentum ($p_t \geq 1.5 - 2.0$ GeV/c) can be described by perturbative QCD. A minimum transverse momentum is needed to be able to realize the perturbative calculations.

  In QCD compton scattering (Figure 3) the photon couples directly with a quark in the proton. The final state consists of a quark and a gluon which form jets.

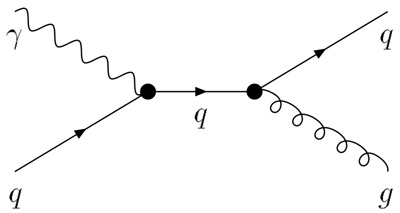

Figure 3: QCD compton scattering.

- **Anomalous component:** The fluctuation of the photon in an unbounded virtual $q\bar{q}$ pair, which interacts in a hard process with the partons in the proton, is called the anomalous component. In addition to the two jets of the hard process and the proton remnant, a fourth jet can be formed from the hadronic photon remnant.

A strict separation between the anomalous component and the hard VDM component relating to the transverse momentum is not possible. The hadronic contents of the photon is described for both components in the quark and gluon number density function of the photon $f_{q/\gamma}(x, \mu^2)$ and $f_{g/\gamma}(x, \mu^2)$. The variable x is the fraction of the momentum of the parton in the photon and μ is the mass scale.

The total photoproduction cross section is the sum of the cross sections of the three components

$$\sigma^{\gamma p}_{\mathrm{tot}} = \sigma^{\gamma p}_{\mathrm{VDM}} + \sigma^{\gamma p}_{\mathrm{direct}} + \sigma^{\gamma p}_{\mathrm{anomalous}} \quad . \qquad (15)$$

1.2.2 The Total γp Cross Section

The total γp cross section can be determined from the differential ep cross section. For quasi-real photons ($Q^2 \approx 0$) the Weizsäcker-Williams approximation [5] is valid which approximates the ep cross section by the product of equivalent number of photons in the electron times the real γp cross section. The differential ep cross section can be written as

$$\frac{\mathrm{d}^2\,\sigma^{ep}}{\mathrm{d}y\,\mathrm{d}Q^2} = \frac{\alpha}{2\pi}\,\frac{1}{Q^2}\cdot \left(\left(1-\frac{2m_e^2}{Q^2}\right)\cdot y\cdot\sigma_T\left(W_{\gamma p}^2\right)+\frac{2\,(1-y)}{y}\cdot\left(\sigma_T\left(W_{\gamma p}^2\right)+\sigma_L\left(W_{\gamma p}^2\right)\right)\right) \quad . \tag{16}$$

Terms of m_p^2/s and m_e^2/s are neglected, but the term m_e^2/Q^2 is retained which gives a correction to the Weizsäcker-Williams approximation at very low Q^2 values. σ_T and σ_L are the γp cross sections of the transverse and longitudinal polarized photons. For quasi-real photons the longitudinal component σ_L can be neglected. The quantity σ_T can be identified with the photoproduction cross section $\sigma_{\mathrm{tot}}^{\gamma p}$

$$\sigma_{\mathrm{tot}}^{\gamma p}\left(W_{\gamma p}^2\right) = \sigma_T\left(W_{\gamma p}^2\right) \quad . \tag{17}$$

This reduces the equation (16) to

$$\frac{\mathrm{d}^2\,\sigma^{ep}}{\mathrm{d}y\,\mathrm{d}Q^2} = \frac{\alpha}{2\pi}\,\frac{1}{Q^2}\left(\frac{1+(1-y)^2}{y}-\frac{2m_e^2}{Q^2}\right)\cdot\sigma_{\mathrm{tot}}^{\gamma p}\left(W_{\gamma p}^2\right) \quad . \tag{18}$$

Integration over Q^2 gives

$$\frac{\mathrm{d}\,\sigma^{ep}}{\mathrm{d}y} = F_{\gamma/e}\,(y)\cdot\sigma_{\mathrm{tot}}^{\gamma p}\left(W_{\gamma p}^2\right) \quad , \tag{19}$$

where

$$F_{\gamma e}\,(y) = \frac{\alpha}{2\pi}\left(\frac{1+(1-y)^2}{y}\cdot\ln\left(\frac{Q_{\mathrm{max}}^2}{Q_{\mathrm{min}}^2}\right)-2m_e^2 y\left(\frac{1}{Q_{\mathrm{min}}^2}-\frac{1}{Q_{\mathrm{max}}^2}\right)\right) \quad , \tag{20}$$

$$\text{with} \qquad Q_{\mathrm{min}}^2 = \frac{m_e^2 y^2}{1-y}$$

is the kinematical photon flux factor. For $Q_{\mathrm{max}}^2 \gg Q_{\mathrm{min}}^2$ the differential ep cross section becomes

$$\frac{\mathrm{d}\,\sigma^{ep}}{\mathrm{d}y} = \frac{\alpha}{2\pi}\left(\frac{1+(1-y)^2}{y}\cdot\ln\left(\frac{Q_{\mathrm{max}}^2}{Q_{\mathrm{min}}^2}\right)-\frac{2\,(1-y)}{y}\right)\sigma_{\mathrm{tot}}^{\gamma p}\left(W_{\gamma p}^2\right) \quad . \tag{21}$$

The term $2(1-y)/y$ in equation (21) represents the correction to the Weizsäcker-Williams approximation after taking into account the m_e^2/Q^2 term in equation (16). The center of mass energy of the γp system is given as

$$W_{\gamma p} = \sqrt{ys\,(1-x)+m_p^2} \quad . \tag{22}$$

At H1 the measurable Q^2 and y regions of the photoproduction, where the electron is measured at a very large angle ϑ_e, are given by the acceptance of the electron detector (described in Section 2.2) which is

$$\begin{array}{rcccl} 3\cdot 10^{-8}\ \mathrm{GeV}^2/c^2 & < & Q^2 & < & 10^{-2}\ \mathrm{GeV}^2/c^2 \\ 0.2 & < & y & < & 0.8 \quad . \end{array} \tag{23}$$

Therefore the center of mass energy of the γp system lies in the region of

$$130\ \mathrm{GeV} \quad < \quad W_{\gamma p} \quad < \quad 265\ \mathrm{GeV} \quad . \tag{24}$$

The weighted average is

$$\langle W_{\gamma p} \rangle \quad = \quad 188\ \mathrm{GeV} \quad . \tag{25}$$

The total cross section of the photoproduction was measured by the H1 collaboration as [6]

$$\sigma_{\mathrm{tot}}^{\gamma p} \quad = \quad 156 \pm 2 \pm 18\ \mu\mathrm{b} \quad . \tag{26}$$

The ZEUS collaboration published a value [7] of

$$\sigma_{\mathrm{tot}}^{\gamma p} \quad = \quad 143 \pm 4 \pm 17\ \mu\mathrm{b} \quad , \tag{27}$$

which agrees within the errors. The measurements are compatible with the calculations of Donnachie and Landshoff [8] and of Abramowicz *et al.* [9] which both are based on Regge phenomenology.

1.3 The Deep Inelastic Electron Proton Scattering

1.3.1 General View

Because of the high center of mass energy $\sqrt{s} = 296$ GeV at HERA it is possible to achieve square of four momentum transfer up to $Q^2 \approx s/c^2 = 87567\ \mathrm{GeV}^2/c^2$. This is about two orders of magnitude higher than at fixed target experiments. In addition HERA allows measurements at very low *x-Bjorken*. At $Q^2 = 10\ \mathrm{GeV}^2/c^2$ x values down to 10^{-4} are possible which cannot be reached with fixed target experiments.

At the limit of high energies the proton can be seen as a system of quasi-free partons which carry the fraction x of the momentum of the proton if the intrinsic transverse momentum is neglected. Deep inelastic electron proton scattering under these circumstances is an elastic scattering of the electron with a quasi-free parton (quark parton model QPM). In this model the cross section is given by the incoherent sum of the cross sections with the partons.

1.3.2 The Proton Structure Function

In leading order electroweak theory the differential cross section for deep inelastic scattering with γ, Z^0 or $W^\pm$ exchange can be written as [10]

$$\frac{\mathrm{d}^2\,\sigma^{ep}}{\mathrm{d}x\,\mathrm{d}Q^2} = \frac{4\pi\,\alpha^2}{x\,Q^4}\left(y^2\,xF_1 + (1-y)\,F_2 + \left(y - \frac{y^2}{2}\right)xF_3\right) \tag{28}$$

$$= \frac{2\pi\,\alpha^2}{x\,Q^4}\left(\left(1+(1-y)^2\right)F_2 - y^2\,F_L + \left(1-\left(1-y^2\right)^2\right)xF_3\right) \quad . \tag{29}$$

The functions xF_1, F_2, F_3, and F_L are the structure functions, all depending on x and Q^2. F_2 is the proton structure function and F_3 describes the non parity conserving part of the cross section. F_L is defined by the transversal structure function xF_1 and F_2 and describes the interaction with the longitudinal polarized photons.

$$F_L = F_2 - xF_1 \tag{30}$$

F_L is equal to zero for spin 1/2 particles as long as the quark masses and the intrinsic transverse momenta are neglected (Callan-Gross relation [11]).

High order QCD effects change this relation and make the longitudinal structure function F_L proportional to α_s the strong coupling constant. This can be neglected to a good approximation except for very small x [12, 13].

In the quark parton model (QPM) F_2 and F_3 can be written in terms of the probability q_f of finding a quark or antiquark of the flavour f with the momentum fraction x. The structure functions are given in the QPM by

$$F_2\left(x,Q^2\right) = \sum_{\text{flavours}} \left(x\,q_f\left(x,Q^2\right) + x\,\bar{q}_f\left(x,Q^2\right)\right)\cdot A_f\left(Q^2\right) \tag{31}$$

$$xF_3\left(x,Q^2\right) = \sum_{\text{flavours}} \left(x\,q_f\left(x,Q^2\right) - x\,\bar{q}_f\left(x,Q^2\right)\right)\cdot B_f\left(Q^2\right) \quad . \tag{32}$$

The summation runs over all flavours in the proton. The coefficients A_f and B_f for the quark flavours f are given by the different couplings of the partons with the electron. For small Q^2 the exchange of Z^0 and $W^\pm$ can be neglected due to their large masses. Hence the coefficients A_f and B_f are reduced to

$$A_f = e^2 \tag{33}$$

$$B_f = 0 \tag{34}$$

with e the charge of the electron.

However the Z^0 and $W^\pm$ couplings become important for high Q^2 and dominate the cross section above $Q^2 = 10^4$ GeV^2. Because the cross section in equation (28) and (29) is proportional to $1/Q^4$ the higher Q^2 region requires high luminosity in order to get reasonable event rates.

1.4 The Production of Charmed Particles

Charmed baryons and mesons are produced in fragmentation of charm quarks. The charm quark has to be first produced in the scattering process itself. This occurs mainly via the process of boson gluon fusion (BGF) as shown in Figure 4. The gauge boson emitted from the electron scatters with a gluon of the proton under production of a heavy $q\bar{q}$ pair. The exchanged gauge boson is a γ or a Z^0. At HERA the ep scattering is dominated by the exchange of photons at low Q^2. The contribution of the gauge boson Z^0 can be neglected due to its high mass. Therefore charm quarks at HERA are mainly produced by photoproduction with quasi-real photons at $Q^2 \approx 0$.
Other processes, which can be neglected, include the production of charm quarks in

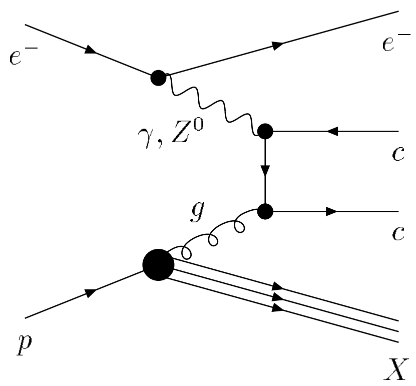

Figure 4: The process of boson gluon fusion (BGF), the main production process for heavy quark pairs such as $c\bar{c}$ pairs.

- the fragmentation of light quarks due to the large charm-quark mass ($m_c \approx$ 1.5 GeV$/c^2$) or the large Z^0 mass in case of a Z^0 boson exchange.

- the coupling of a neutral gauge boson γ or Z^0 on a charm quark in the proton sea (Figure 5) due to the large charm-quark mass ($m_c \approx 1.5$ GeV$/c^2$).

- the coupling of a W^- boson on a light $\bar{d}$ or $\bar{s}$ quark (Figure 5). The cross section of this process depends on the cross section of ep scattering with charged current on light quarks ($\sigma_{\bar{d}}, \sigma_{\bar{s}}$) and their corresponding element of the Cabibbo-Kobayashi-Maskawa (CKM) matrix.

$$\sigma\left(e^- p \longrightarrow \nu_e \bar{c} X\right) = |V_{cd}|^2 \cdot \sigma_{\bar{d}} + |V_{cs}|^2 \cdot \sigma_{\bar{s}} + |V_{cb}|^2 \cdot \sigma_{\bar{b}} \qquad (35)$$

  Charged current processes are suppressed due to the large $W^\pm$ mass.

- the decay of bottom quarks, due to the small production cross section of bottom quarks, two or three orders of magnitude smaller than the charm production cross section.

The photon can interact as a point-like gauge boson (direct component) as well as a particle with a hadronic structure (resolved component). The ratio between these two components to produce charm quarks is dependent on the center of mass energy of the γp system and on the charm-quark mass. The fraction of the resolved component varies from ≤ 5 % at the low energies of fixed target experiments up to ≤ 30 % at the high energies of HERA [14, 16].

The kinematics of the photon gluon fusion (PGF) is described with the variables of ep scattering and three additional quantities [17]. Some of the possible production diagrams are shown in Figure 6.

The gluon which interacts with the photon carries the fraction x_g of the proton momentum

$$p_g = x_g \cdot p_p \quad . \qquad (36)$$

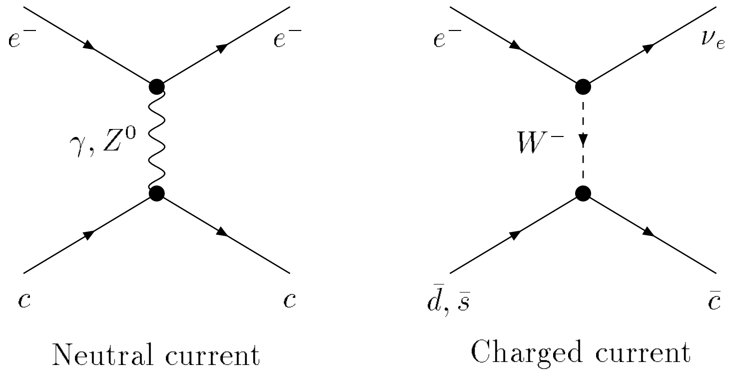

Figure 5: Neutral current and charged current charm production.

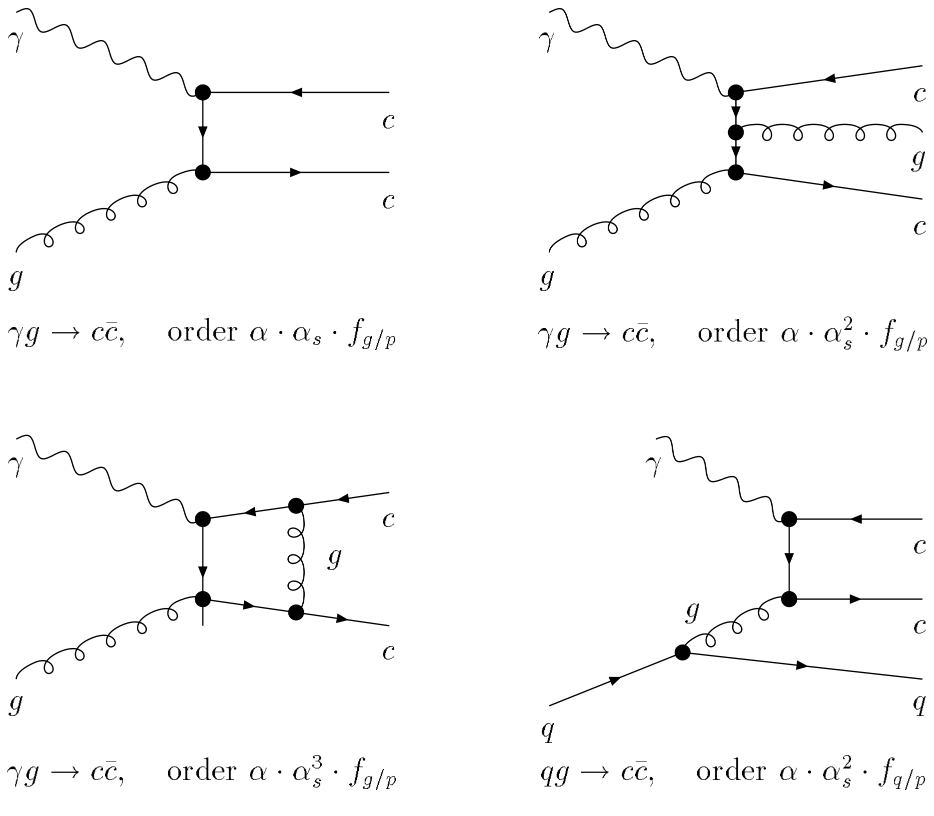

Figure 6: Some diagrams of possible charm production by photon gluon fusion (order $\alpha \cdot \alpha_s$, $\alpha \cdot \alpha_s^2$, and $\alpha \cdot \alpha_s^3$), where $f_{g/p}$ is the gluon number density function of the proton and $f_{q/p}$ is the quark number density function of the proton.

Analogous to the variable y, the ratio of the real to the maximum momentum transfer, z, perpendicular to the proton flight direction is defined as

$$z \equiv \frac{(p_c \cdot p_p)}{(q \cdot p_p)} \quad . \tag{37}$$

The azimuth angle ϕ between the lepton and the hadron plane is given by

$$\cos\phi \equiv \frac{(\vec{p_p} \times \vec{p_e}) \cdot (\vec{p_p} \times \vec{p_c})}{|\vec{p_p} \times \vec{p_e}| \cdot |\vec{p_p} \times \vec{p_c}|} \quad . \tag{38}$$

The center of mass energy of the hard process $\gamma g \longrightarrow c\bar{c}$ is

$$\hat{s} \equiv (p_c + p_{\bar{c}})^2 \approx y \cdot x_g \cdot s - Q^2 \quad . \tag{39}$$

The square of the transverse momentum of the c quarks is

$$p_t^2 = \hat{s} \cdot z \cdot (1-z) - m_c^2 \quad . \tag{40}$$

The total cross section of the production of charm quarks by photon gluon fusion (PGF) can be written with these variables as

$$\sigma_{c\bar{c}}^{\mathrm{PGF}} = \int \mathrm{d}y \int \mathrm{d}Q^2 \int \mathrm{d}x_g \int \mathrm{d}z \int \mathrm{d}\phi \, g\left(x_g, \mu^2\right) \, \hat{\sigma}\left(y, Q^2, x_g, z, \phi, \hat{s}, \mu^2\right) \tag{41}$$

with $\hat{\sigma}$ the cross section of the hard process $\gamma g \longrightarrow c\bar{c}$. $g(x_g, \mu^2)$ is the gluon density distribution in the proton and μ the scale at which the perturbative QCD is calculated.

The gluon density function $g(x_g, \mu^2)$ describes the gluon momentum fraction distribution at a scale μ^2. Due to the k_t-factorization [18] for leading logarithms of x_g the gluon density function $g(x_g, \mu^2)$ is derived from an integration of a generalized proton structure function $\mathcal{G}(x_g, k_t)$ over the transverse momentum up to some limit μ

$$\int_0^{\mu} \mathrm{d}k_t^2 \, \mathcal{G}\left(x_g, k_t\right) = g\left(x_g, \mu^2\right) \quad , \tag{42}$$

where $\mathcal{G}(x_g, k_t)$ is the probability of finding a gluon at longitudinal momentum fraction x_g and transverse momentum k_t. For a small-x gluon its momentum can be of the form $k \approx x_g p_p + k_t$, so that $k^2 \approx -k_t^2$ and k_t also describes the off-shellness of the gluon.

The cross section of the process $e^- g \longrightarrow e^- c\bar{c}$ can be expressed by the cross section of the corresponding photoproduction with the Weizsäcker-Williams approximation. The photon flux factor $F(y)$ given in equation (20) describes the probability for a radiated photon with a momentum fraction y of the electron. After the integration over Q^2, z and ϕ the cross section can be written as

$$\sigma_{c\bar{c}}^{\mathrm{PGF}} = \int \mathrm{d}y \, F\left(y\right) \int \mathrm{d}x_g \, g\left(x_g, \mu^2\right) \, \hat{\sigma}\left(\gamma g \longrightarrow c\bar{c}\right)\left(\hat{s}, \mu^2\right) \tag{43}$$

with $g(x_g, \mu^2)$ the gluon density distribution and $\hat{\sigma}$ the cross section of the photoproduction process $\gamma g \longrightarrow c\bar{c}$.

Ellis and Nason [14] have calculated the cross section of heavy quarks in photoproduction up to the order of $\alpha \cdot \alpha_s^2$. The aim was to describe the photoproduction cross section of heavy quarks at the fixed target experiments.

The prediction of the cross section has large uncertainties. The question is how good the description of the photoproduction of charm quarks with the PGF model and the QCD corrections is. Perturbative QCD is only applicable if the charm-quark mass is large in respect to the scale Λ of QCD. Another uncertainty comes from the unknown gluon density distribution $g(x_g, \mu^2)$.

For the calculation of the charm cross section the following parameters were varied to estimate the errors.

- The charm-quark mass m_c:
  Because of the mass dependence of the result different values of the charm-quark mass of 1.2, 1.5, and 1.8 GeV/c^2 are chosen. The mass value preferred by QCD sum rules is $m_c = 1.64 \pm 0.5$ GeV/c^2 [19].

- The scale of QCD Λ:
  In the $\overline{\mathrm{MS}}$ renormalization scheme[1] [20] the value of Λ depends on the number of active flavours n_f [21]. For the active flavours $n_f = 3, 4, 5$ the following Λ_{n_f} are chosen for the calculation:

$$\begin{aligned} \Lambda_3 &= 310 \pm 110 \text{ MeV}/c^2 \\ \Lambda_4 &= 260 \pm 100 \text{ MeV}/c^2 \\ \Lambda_5 &= 170 \pm 80 \text{ MeV}/c^2 \end{aligned} \tag{44}$$

  For the estimation of the uncertainty the values were varied within the errors.

- The scale μ:
  The choice of the scale $\mu < 2m_c$ leads to problems because this region for μ is not measured and an extrapolation from present data using the Altarelli-Parisi evolution equations shows large instabilities. In order to avoid this problem a value $\mu^2 \approx 4m_c^2 \approx 10$ GeV$^2/c^4$ is chosen. The uncertainties are assumed to be of the order of a factor of two.

- The gluon density distribution $g(x_g, \mu^2)$:
  The scale μ is set to a fixed value $\mu_0^2 = 10$ GeV$^2/c^2$ for the whole calculation. The gluon density distribution [21] used at the fixed scale μ_0^2 is

$$g\left(x_g, \mu_0^2\right) = 0.24 \cdot x_g^{0.36} \left(1 - x_g\right)^{\beta(x_g)} \tag{45}$$

  with

$$\beta\left(x_g\right) = 7.7 + 5.5 \ln\left(\ln\left(\frac{1}{1 - x_g}\right)\right) \quad . \tag{46}$$

[1] Modified minimal subtraction renormalization scheme.

The results of the calculation of Ellis and Nason [14] are shown in Figure 7 with the measurements of the different fixed target experiments. The middle curve corresponds to the choice $\Lambda_4 = 260$ GeV, $\mu^2 = 10$ GeV^2 and the charm-quark mass $m_c = 1.5$ GeV$/c^2$. The estimates of the errors due to variation of μ and Λ are added in quadrature to give the outer lines.

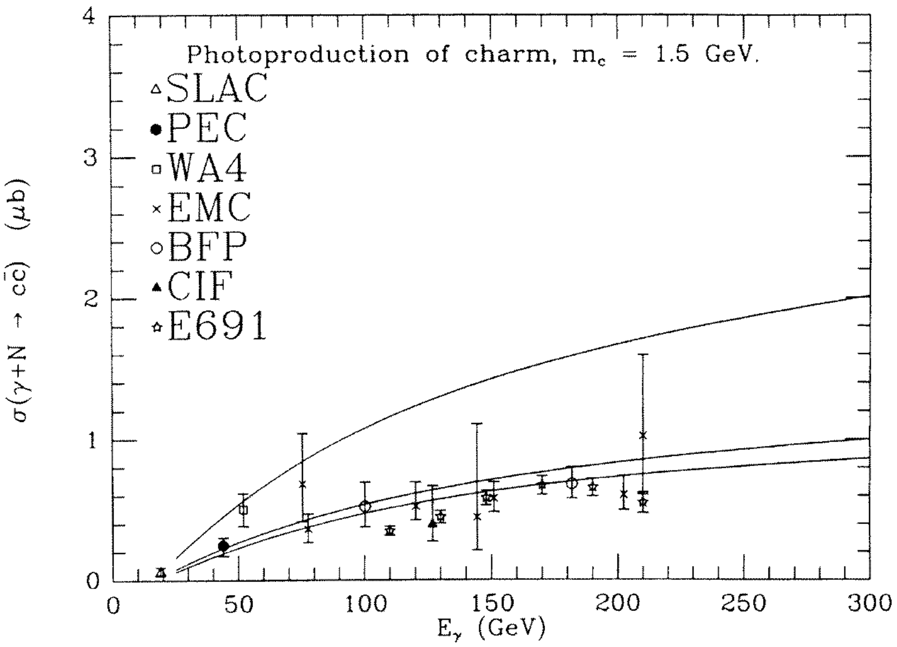

Figure 7: The total cross section for the photoproduction of a pair of charm quarks versus the photon energy E_γ. The middle curve corresponds to the choice $\Lambda_4 = 260$ GeV, $\mu^2 = 10$ GeV^2 and the charm-quark mass $m_c = 1.5$ GeV$/c^2$. The band of values represents an estimate of the theoretical uncertainty due to the variation of all parameters except the mass of the charm quark which is fixed at 1.5 GeV$/c^2$ [14]. The data points are taken from the following references: E691 [22], PEC [23], SLAC [24], WA4 [25], EMC [26], BFP [27], and CIF [28]. The WA4 result is the inclusive cross section for D^0 production. The CIF data and the EMC data at 16.8 GeV, 23.3 GeV, and 28.1 GeV center of mass energies are inclusive cross sections for $D^0(\bar{D}^0)$ production.

Based on calculations of the cross section for fixed target experiments predictions for the production of heavy quarks at HERA energies were made. The energy distribution of quasi-real photons is given by the Weizsäcker-Williams approximation. The resulting charm cross section for nominal beam energies ($E_e = 30$ GeV, $E_p = 820$ GeV) at HERA for different charm-quark masses are given in Table 1. The hadronic component has been included, using the photon structure function of Drees and Grassie [29]. The contribution of resolved photons to the charm cross section was predicted to be less than 30 % [14, 16].

A comparison of the x_{F} and p_t distribution, calculated by Ellis and Nason, with

m_c [GeV/c^2]	$\sigma_{c\bar{c}}$ [μb]
1.2	$1.24^{+0.53}_{-0.35}$
1.5	$0.68^{+0.26}_{-0.18}$
1.8	$0.41^{+0.14}_{-0.10}$

Table 1: Prediction of the charm cross sections at HERA for different charm-quark masses [14].

resent data of photon nucleon scattering experiments indicate a charm-quark mass about 1.5 GeV/c^2 [30]. The Feynman x variable x_{F} is, in contradiction to *x-Bjorken*, defined as

$$x_{\mathrm{F}} \quad = \quad \frac{p_L}{p_L^{\max}} \quad , \tag{47}$$

where p_L and $p_L^{\max}$ are the longitudinal momentum of the particle and its maximum possible longitudinal momentum in the center of mass frame.

1.5 The Decay of Charmed Particles

The charm quarks formed by different hard subprocesses fragment into hadrons. They are separated by their quark configuration into charmed mesons ($c\bar{q}$), charmed baryons (cqq) and charmonium-states ($c\bar{c}$). In the next sections only charmed mesons are discussed.

Charmed vector mesons decay through the strong and the electromagnetic interactions to lighter pseudo-scalar D mesons.

In D mesons the charm quarks are stable with respect to the strong force, but they decay weakly and have therefore a relatively long life time of the order of a pico-second. The charm quark converts to the lighter strange or down quark. The excited states of the D mesons decay strongly or electromagnetically to their ground states. A list of ground state and first excited state D mesons is given in Tables 2 and 3. There is a good opportunity to study the weak interaction under the influence of the strong interaction. The measurement of the decay channels gives a possible test of the Standard Model; the discovery of forbidden decay channels would be an indication of new physics.

meson	quark contents	mass [MeV/c^2]	full width [MeV]	decay channel
$D^{*\pm}$	$c\bar{d}$, $\bar{c}d$	2010.0 ± 0.5	< 0.131	$D^0\pi^\pm$, $D^\pm\pi^0$, $D^\pm\gamma$
D^{*0}, $\bar{D}^{*0}$	$c\bar{u}$, $\bar{c}u$	2006.7 ± 0.5	< 2.1	$D^0\pi^0$, $D^0\gamma$
$D_S^{*\pm}$	$c\bar{s}$, $\bar{c}s$	2110.0 ± 1.9	< 4.5	$D_S^\pm\gamma$

Table 2: First excited states of the D mesons (D^* resonances, $J^P = 1^-$) [31].

meson	quark contents	mass [MeV/c^2]	life time [ps]
$D^\pm$	$c\bar{d}$, $\bar{c}d$	1869.4 ± 0.4	1.057 ± 0.015
D^0, $\bar{D}^0$	$c\bar{u}$, $\bar{c}u$	1864.6 ± 0.5	0.415 ± 0.004
$D_S^\pm$	$c\bar{s}$, $\bar{c}s$	1968.5 ± 0.7	0.467 ± 0.017

Table 3: Ground states of the D mesons ($J^P = 0^-$) [31].

In the Standard Model the decay of heavy quarks is described by weak charged currents. They decay to lighter quarks and a virtual $W^\pm$ boson. The $W^\pm$ boson decays on its part into two leptons or into a quark and an antiquark. The decay with a final state of hadrons and leptons is called a semi leptonic decay, and with only hadrons, a hadronic decay. By annihilation, also leptonic decays are possible. In Figure 8 some of these decay diagrams are shown. In the final state of the spectator graphs the D meson always decays in a K meson. Those ground states are listed in Table 4.

meson	quark contents	mass [MeV/c^2]	life time [ns]
$K^\pm$	$u\bar{s}$, $\bar{u}s$	493.677 ± 0.016	12.371 ± 0.029
K^0, $\bar{K}^0$	$d\bar{s}$, $\bar{d}s$	497.672 ± 0.031	
K_S^0	$\frac{1}{2} \cdot (d\bar{s} + \bar{d}s)$	497.672 ± 0.031	0.08926 ± 0.00012
K_L^0	$\frac{1}{2} \cdot (d\bar{s} - \bar{d}s)$	497.672 ± 0.031	51.7 ± 0.4

Table 4: Ground states of the K mesons ($J^P = 0^-$) [31].

There are many different decay channels with one or more pions and kaons in the final state . The branching ratios of these decay channels are all rather small.

1.6 The Choice of the Decay Channel

The produced charm quarks are identified in this analysis by the decay of D^0 mesons, which are often produced in the fragmentation of the charm quark or by decay products of excited states of D mesons.

The D^0 meson decays through the weak process. There are many different decay channels each with a small branching ratio. To measure experimentally the invariant mass of the D^0 meson with the information of the tracking chambers the decay products must be charged. The two most easily studied decay channels, with reasonably large branching ratios, are

$$D^0 \longrightarrow K^-\pi^+ \tag{48}$$

$$\begin{aligned} D^0 &\longrightarrow K_S^0\pi^+\pi^- \\ &\quad \hookrightarrow \quad \pi^+\pi^- \quad . \end{aligned} \tag{49}$$

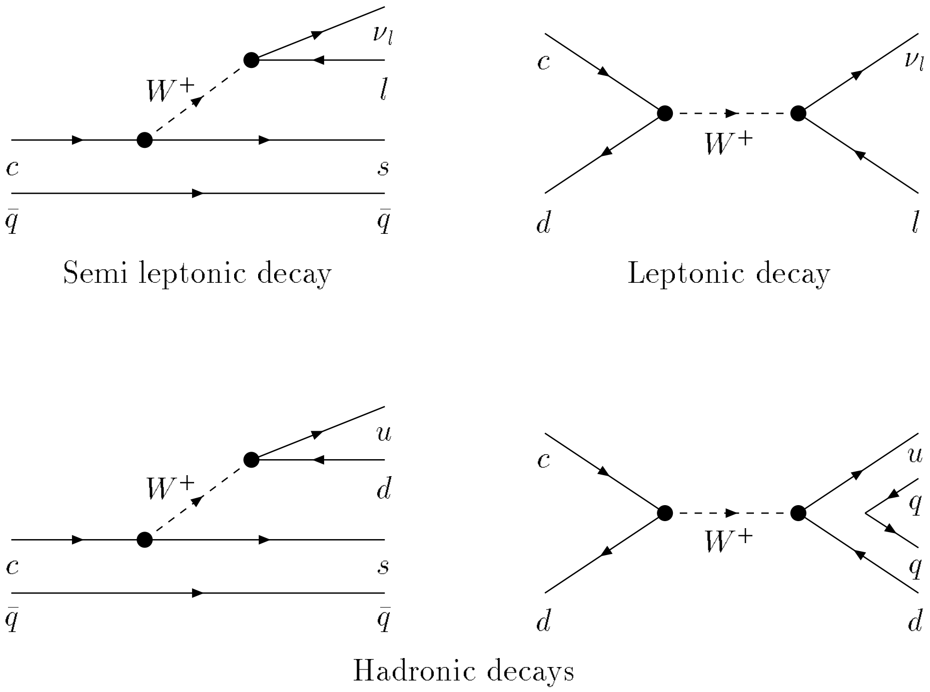

Figure 8: Leptonic, semi leptonic, and some hadronic decay of charmed mesons. The diagrams on the left side are called spectator graphs. The diagrams on the right side are annihilation graphs, where the quark and the antiquark convert to a gauge boson.

The branching ratios for these channels are [31]

$$
\begin{array}{lllll}
 & \mathcal{B}\left(D^0 \longrightarrow K^-\pi^+\right) & = & (4.01 \pm 0.14) & \% \\
 & \mathcal{B}\left(D^0 \longrightarrow \bar{K}^0\pi^+\pi^-\right) & = & (5.3 \pm 0.6) & \% \\
\text{with} & \mathcal{B}\left(K^0_S \longrightarrow \pi^+\pi^-\right) & = & (68.61 \pm 0.28) & \% \quad .
\end{array}
\tag{50}
$$

In this analysis the channel $D^0 \longrightarrow K^0_S\pi^+\pi^-$ was chosen because of the possibility of suppressing the background due to the second vertex of the K^0_S meson decay and the previously gained experience in the reconstruction of K^0_S mesons.

Nevertheless it turns out that the D^0 decays are hard to isolate. The available signal to estimate the charm cross section is too small. With the method of charm-tagging, which is described in Section 7.5, a much better charm signal is achieved.

1.7 The Branching Ratios

The probabilities of the fragmentation of a charm quark into the different possible hadrons are not very well known. Using recent measurements at e^-e^+ storage rings the following estimation can be made:

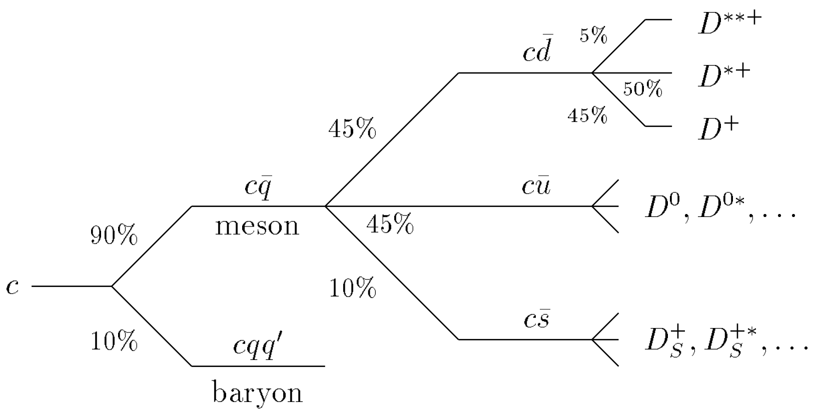

The ratio of mesons to baryons follows from the measurement of the production cross section of Λ_c baryons [32]. Three possible antiquarks are available to the charm quark to produce a D meson. Measurements of the production rate of D_S mesons [33] as well as of $s\bar{s}$ quark pairs in comparison to $u\bar{u}$ quark pairs in fragmentation [34] give an approximate 10 % probability for the production of strange D mesons. For the remaining fraction of D mesons it can be assumed that the same amount of charged ($c\bar{d}$) as neutral ($c\bar{u}$) mesons are produced due to isospin symmetry as long as the quark mass differences can be neglected. The estimation of the fraction of the D^* mesons of all produced D mesons leads to problems. The naive expected fraction between pseudo-scalar and vector mesons is 1 : 3 due to the possible spin states. However experiments favour a ratio of 2 : 3 for charmed mesons. The fraction

$$R = \frac{V}{P+V} \quad , \tag{51}$$

where V and P signify vector (V) and pseudo-scalar (P) charmed mesons, respectively, was measured by the ALEPH collaboration [35] to be

$$R = 0.60 \pm 0.08_{\mathrm{stat.}} \pm 0.05_{\mathrm{syst.}} \tag{52}$$

and by the NA14/2 collaboration [30] to be

$$R = 0.64 \pm 0.10 \quad . \tag{53}$$

In addition to the pseudo-scalar (D) and vector mesons (D^*), higher excited states can occur, leading to an additional uncertainty in the determination of the ratio.

The probability of the fragmentation of the c quark into a D^{*+} meson has been measured with the subsequent decay by the ALEPH collaboration [35] as

$$(P_{c \to D^{*+}}) \cdot \mathcal{B}\left(D^{*+} \longrightarrow D^0 \pi_s^+\right) = (18.5 \pm 1.3_{\mathrm{stat.}} \pm 2.0_{\mathrm{syst.}})\ \% \quad , \tag{54}$$

where the $D^{*\pm}$ meson decays to a D^0 meson and a pion. The branching ratio for the decay channel of the $D^{*\pm}$ is given as [31]

$$\mathcal{B}\left(D^{*+} \longrightarrow D^0 \pi_s^+\right) = (68.1 \pm 1.3)\ \% \quad . \tag{55}$$

Hence it follows for the production of D^{*+} mesons from a c quark

$$P_{c\to D^{*+}} \quad = \quad (27.2 \pm 2.4_{\text{stat.}} \pm 3.4_{\text{syst.}})\ \% \quad . \tag{56}$$

The $D^{*\pm}$ meson decays to a D^0 meson and a pion. The D^0 meson decays into a $\bar{K}^0$ meson which decays with a probability of 50 % as a K^0_S meson. The K^0_S meson is the short lived decay state of the $\bar{K}^0$ meson and decays into two pions. The branching ratio for these decays are [31]

$$\begin{array}{rlcl} & \mathcal{B}\left(D^0 \longrightarrow \bar{K}^0\pi^+\pi^-\right) & = & (5.3 \pm 0.6)\ \% \\ \text{with} & \mathcal{B}\left(K^0_S \longrightarrow \pi^+\pi^-\right) & = & (68.61 \pm 0.28)\ \% \quad . \end{array} \tag{57}$$

The D^0 meson can decay in a $\bar{K}^0$ meson and two opposite charged pions in a resonant or in a nonresonant decay. In the branching ratio (57) the nonresonant part of the decay with a branching ratio of [31]

$$\mathcal{B}\left(D^0 \longrightarrow \bar{K}^0\pi^+\pi^-\right)_{\text{nonresonant}} \quad = \quad (1.43 \pm 0.26)\ \% \tag{58}$$

is included.

Altogether the probability to get from a $c\bar{c}$ quark pair at least one $D^{*\pm}$ meson which decays to a D^0 meson and through a K^0_S meson in five pions is

$$P\left(c\bar{c} \to D^* \to \ldots \to 5\pi\right) \quad = \quad (0.67 \pm 0.15)\ \% \quad . \tag{59}$$

The probability to get from a $c\bar{c}$ pair two $D^{*\pm}$ mesons which both decay by the above mentioned decay channel is negligibly small.

2 The Experiment

2.1 The Electron Proton Storage Ring HERA

The storage ring HERA is the first electron proton collider and came into operation in autumn 1991. An overview of the accelerator facility is given in Figure 9.

The electrons and the protons are accelerated and stored in two separated pipes in a ring 15 to 20 m underground. The earlier accelerators LINAC, DESY and PETRA were in some parts modified and used as preaccelerators.

The electrons are produced thermo electrically and accelerated to an energy of 450 MeV with the linear accelerator LINAC II. They are then injected into the electron synchortron DESY II where their energy is increased to 7.5 GeV. In PETRA II they achieve an injection energy of 14 GeV for HERA. The electron ring in HERA is designed for energies up to 30 GeV and can store the electrons over several hours. The required magnetic field of 0.165 T is achieved with normal conducting magnets in contrast to the proton ring in HERA. The electrons lose through synchotron radiation 127 MeV energy at each turn. The total power loss of the accelerator system is about 6.5 MW.

The protons are gained from negatively charged hydrogen atoms. They are produced in a ion source of an energy of 18 keV, focused with a high frequency quadrupole magnet and accelerated to an energy of 500 keV. After the linear accelerator LINAC III they achieve a momentum of 50 MeV/c. The protons are stripped by a thin foil when they enter the proton synchotron DESY III. The protons reach PETRA II with a momentum of 7.5 GeV/c and are accelerated to the injection energy for 40 GeV of the proton ring at HERA in the same pipe as the electrons but in a counter-clockwise rotating direction. In HERA they are accelerated in separate pipes to the design energy of 820 GeV. The superconducting bending magnets achieve a magnetic field of 4.65 T. The superconducters are cooled with liquid helium at a temperature of 4.2 K from a special cooling system of DESY. The required power is less than 20 kW.

There are four locations in HERA where the electrons and the protons can collide. The center of mass energy of the ep system is $\sqrt{s} = 314$ GeV at nominal beam energies. In comparison to previous ep scattering experiments with a fixed target the square of maximum four momentum transfer at HERA is $Q^2_{\max} \approx s/c^2 = 98400\ \mathrm{GeV}^2/c^2$ i. e. about two times higher. To get the same center of mass energy with a fixed target experiment it would be necessary to accelerate the electrons to an energy of 52 TeV which is not, at present, possible. With HERA we have access to an entirely new kinematical regime.

In 1993 the electron beam had an energy of 26.7 GeV corresponding to a center of mass energy $\sqrt{s} = 296$ GeV and a square of maximum four momentum transfer $Q^2_{\max} \approx s/c^2 = 87576\ \mathrm{GeV}^2/c^2$. The accelerator is able to run with 220 bunches of each kind. To achieve the design luminosity of $1.5 \cdot 10^{31}\ \mathrm{cm}^{-2}\mathrm{s}^{-1}$ HERA has to run with 210 bunches each containing $0.8 \cdot 10^{13}$ electrons and $2.1 \cdot 10^{13}$ protons. In this situation the currents are 58 mA and 163 mA respectively. The electron and proton beams intersect at each crossing point every 96 ns. Arising from the total cross section one expects only 10^5 ep interactions a second, whereas there is about 10 times more interactions between protons and gas molecules in the beam pipe at the interaction zone of the detectors.

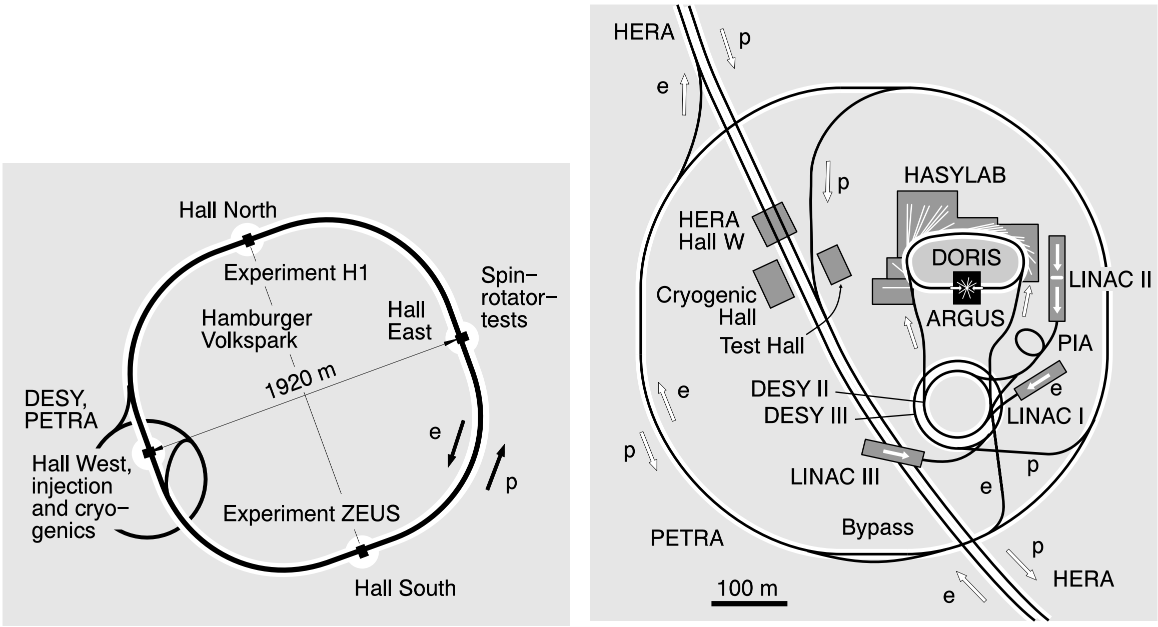

Figure 9: The storage ring HERA on the left with its preaccelerators LINAC, DESY and PETRA on the right.

The radial extensions are $\sigma_{xe} = 280\ \mu$m and $\sigma_{ye} = 37\ \mu$m for the electron beam and $\sigma_{xp} = 265\ \ \mu$m and $\sigma_{yp} = 84\ \mu$m for the proton beam. The profile of the beams are of similar dimensions. That is not the case for the length of the bunches. The proton bunches are more than 10 times longer than the electron bunches and therefore the interaction zone extends over 50 cm (1993 beam conditions). These parameters are summarized in Table 5.

At two of the four interaction zones, experiments were installed in spring 1992. The experiment H1 is installed in the north hall, the experiment ZEUS [36] in the south hall. Two new experiments, HERA-B [38] and HERMES [39], are planned for the remaining two interaction zones.

2.2 The H1 Detector

This chapter briefly describes the H1 detector. A detailed discussion of the H1 detector can be found in [37].

Figure 10 gives a schematic view of the detector. In the same figure the coordinate system is defined for the H1 experiment as used in the H1 collaboration. The z direction is identical with the proton flight direction. Starting from the interaction point the detector consists of the following components:

- **Central Tracker $\boxed{2}$:** It consists of six cylindrical chambers which cover a range in theta of $20° \leq \vartheta \leq 170°$. They are used for reconstruction of charged particles, particle identification and triggering.

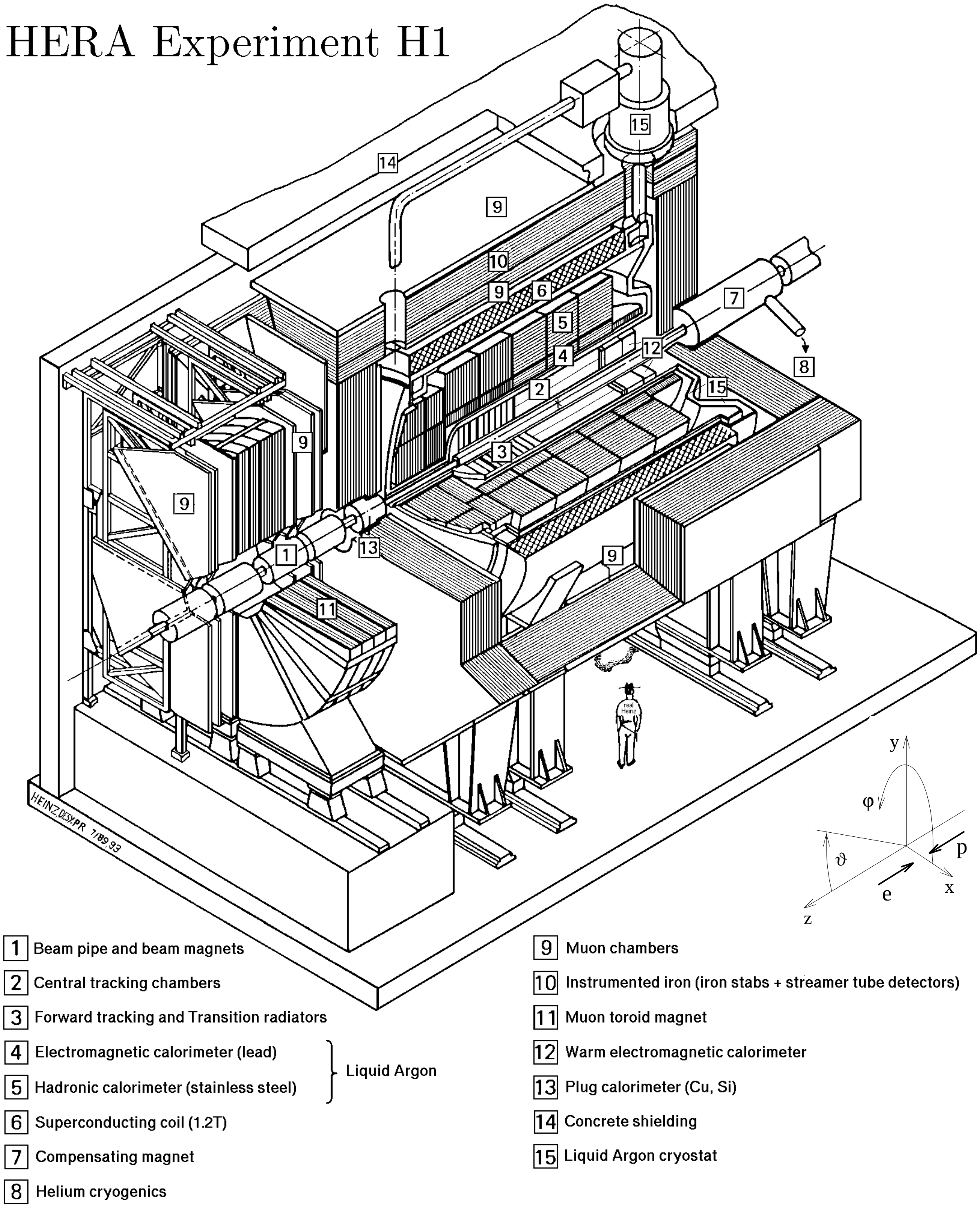

Figure 10: The H1 detector with its main components. On the right the coordinate system as used in the H1 collaboration is defined.

parameter	p beam design	e beam design	p beam 1993	e beam 1993	unit
Length	6336		6336		m
Beam energy	820	30	820	26.7	GeV
Injection energy	40	14	40	12	GeV
Number of bunches	210	210	94	90	
Particles per bunch	$10 \cdot 10^{10}$	$3.8 \cdot 10^{10}$	$3 \cdot 10^{10}$	$3.6 \cdot 10^{10}$	
Current per bunch	760	290	210	265	μA
B field	4.68	0.165	4.68	0.149	T
σ_x at interaction point	0.29	0.26	0.27	0.28	mm
σ_y at interaction point	0.07	0.02	0.08	0.04	mm
σ_z at interaction point	110	8	200	10	mm
Center of mass energy	314		296		GeV
Luminosity	$1.5 \cdot 10^{31}$		$0.15 \cdot 10^{31}$		$\mathrm{cm}^{-2}\mathrm{s}^{-1}$
HF frequency	52.05 208.2	499.7	52.05 208.2	499.7	MHz

Table 5: Summary of HERA parameters [37].

- **Forward Tracker** $\boxed{3}$ **:** It consists of three identical supermodules with drift and proportional chambers. It completes the tracking system in the forward direction and measures particles at a polar angle $7° \leq \vartheta \leq 20°$.

- **Liquid Argon Calorimeter (LAC)** $\boxed{4}$ $\boxed{5}$ **:** It surrounds the tracking system in the forward and barrel region. It comprises an electromagnetic part with lead absorbers which measures the electron energy with a resolution of the order of $12\ \%/\sqrt{E\ [\mathrm{GeV}]}$ and a hadronic part with stainless steel absorber. Its resolution is about $55\ \%/\sqrt{E\ [\mathrm{GeV}]}$. The absolute energy scale for the electromagnetic part is presently known within 3 % for the backward region and 5 % for the forward region. For the hadronic part, the absolute energy scale is measured within 7 %. In the very forward region the calorimeter is completed by a silicium-copper plug. It measures the energy deposition at $0.6° \leq \vartheta \leq 3°$ between the LAC and the beam pipe.

- **Backward Electromagnetic Calorimeter (BEMC)** $\boxed{12}$ **:** It completes the energy deposition measurement in the backward direction ($151° \leq \vartheta \leq 177°$). This lead scintillator calorimeter provides a good electromagnetic but a poor hadronic energy measurement. Just in front of the calorimeter is the backward multiwire proportional chamber giving an accurate space point for tracks. The energy scale for electrons is known to an accuracy of 2 %. Its resolution is about $10\ \%/\sqrt{E\ [\mathrm{GeV}]}+42\ \%/E\ [\mathrm{GeV}]$.

- **Time of Flight System (ToF):** 2 m upstream of the interaction zone just behind the BEMC two scintillator walls are installed. The accurate time resolution of 2 ns allows the identification of particles crossing the detector from outside (upstream).

- **Magnet** $\boxed{6}$ $\boxed{7}$ **:** The superconducting solenoid, of diameter 6 m, surrounds the H1 calorimeter, providing a homogeneous field of 1.2 T parallel to the beam axis in the tracking region of the H1 detector. At the proton entrance side of the solenoid, the compensating coil is located. Its purpose is to provide a longitudinal field integral $\int B_z \, \mathrm{d}z$ opposite to that of the main magnet. This is to compensate the solenoid's influence on the beam.

- **Muon System** $\boxed{9}$ $\boxed{10}$ **:** Muons escaping the H1 detector are recorded in the instrumented iron, on an octagonal yoke surrounding the solenoid. It also allows measurement of the hadronic energy leakage. The system is completed by a forward muon system with its own toroidal magnet to measure high energy muons in the energy range 5 GeV $\leq \mathrm{E}_\mu \leq$ 200 GeV and muon chambers outside of the iron yoke.

- **Luminosity System:** It consists of two crystal calorimeters for the measurement of collinear photons and electrons scattered at very small angles. The photon detector is installed at $z = -103$ m, the electron detector (e-tagger) at $z = -33$ m. The system provides an accurate measurement of the luminosity using the Bethe-Heitler process $ep \longrightarrow ep\gamma$ which is proportional to the luminosity and has a well known cross section. Furthermore it measures electrons scattered at very small angles ($\vartheta \leq 5$ mrad) and photons from initial state bremsstrahlung.

2.3 The H1 Tracking System

A schematical view of the tracking system of H1 is given in Figure 11. The innermost chamber is a double layer multiwire proportional chamber (CIP) [41] giving a fast but rough φ and z position of a track. It is followed by a z-drift chamber (CIZ) with a spatial z resolution of 300 μm [40]. Two jet chambers (CJC) [42] measure the r-φ projection of a track within an accuracy of 210 μm. The inner chamber (CJC1) is divided into 30 φ-sectors each with 24 sense wires, the outer chamber (CJC2) into 60 φ-sectors with 32 layers. The sense wires are stretched parallel to the beam axis. The cells are tilted by 30° in order to give optimal track reconstruction. The tilt compensates the Lorentz angle of the drifting electrons in the magnetic field. Thus the drift direction is almost perpendicular to the track which leads to a better spatial resolution. Further, all tracks with a transverse momentum p_t above 400 MeV/c cross at least once the sense wire plane. For this sense wire, the drift distance for the drift electrons is as short that the drift time is shorter than 50 ns. This property allows the assignment of a bunch crossing time to each track. They not only cross the sense wire plane, they also cross the cell boundaries which leads to the possibility of distinguishing between hits and their mirror hits. For short track segments the ambiguity is resolved with staggered sense wires. An overview of the parameters of CJC1 and CJC2 is given in Table 6. Between the two jet chambers another z-drift chamber (COZ) and two layers of a multiwire proportional chamber (COP) are placed. The signals of CIP and COP are only used for triggering.

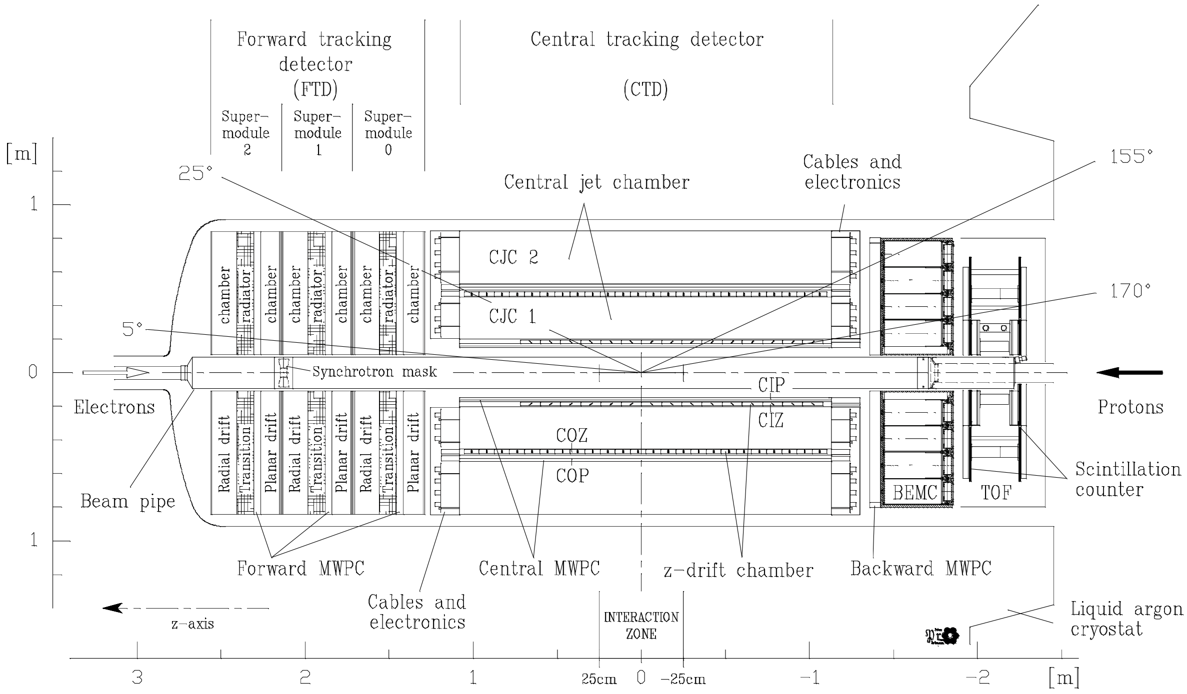

Figure 11: Side view of the H1 tracking system [40].

Taking into account the asymmetry in electron and proton beam energies there is a forward tracking system to detect tracks at small angle ϑ. It consists of three identical modules each with a multiwire proportional chamber (FPC), a radial drift chamber and a planar drift chamber. The FPC gives fast signals for triggering purpose while the radial drift chamber gives an accurate measurement in r-φ plane ($\sigma_{r\varphi} = 200\ \mu$m, design value) and the planar drift chamber measures the x-y projection within 170 μm (design value). In the backward direction in front of the BEMC are installed four layers of a multiwire proportional chamber (BPC). Normally hits in three out of four planes are required which leads to an efficiency of 89 % [43] in 1993.

parameter	CJC1	CJC2	unit
Active length	2200		mm
Inner radius R_i	203	530	mm
Outer radius R_o	451	844	mm
Number of cells	30	60	
Number of sense wires per cell	24	32	
Number of potential wires per cell	50	66	
Number of filed wires per cell	10	10	
Number of cathode wires per cell	49	65	
Sense wire distance	10.16		mm
Maximum drift distance at R_i	22.9	28.5	mm
Maximum drift distance at R_o	44.5	43.1	mm
Gas mixture Ar/C_2H_6	50 : 50		%
Sense voltage	1170		V
Field gradient	120		V/mm
Drift velocity	≈ 54.2		μm/ns
Lorentz angle	≈ 42		$^\circ$
$\sigma_{r\phi}$	145		μm
σ_z	25		mm
$\sigma_{dE/dx}$	10		%
Double hit resolution	2.5		mm

Table 6: Central jet chamber parameters [42].

3 The H1 Trigger System

HERA is the first of a new series of accelerators, which make greater demands on trigger technologies. The task of the trigger is to look for the interesting events within the huge amount of background events.

The limiting factor of recent experiments to store the data is the transfer rate with which data can be written onto permanent storage media. For a conventional tape device this recording speed is roughly 0.5 MByte/s. Experiments tend to require the saving of an ever-increasing amount of data. The amount of data, collected per measuring time, is the product of the event size and the event rate. The event rate is correlated with the luminosity which was continuously increased to obtain the statistics to make observable even very rare processes. The event size is proportional to the number of readout channels which also has to be maximized if the best possible spatial granularity is desired. Therefore it is necessary that the trigger has a high rejection power for high-rate background processes and a high efficiency in selecting physics events. The parameters of the central data acquisition of H1 are summarized in Table 7.

parameter	value	unit
Number of channels[2]	270000	
Raw data size	3	MByte/event
Zero suppressed data size	50 – 100	kByte/event
Bunch crossing rate	10.4	MHz
Expected background rate[3]	10	kHz
Maximum data logging rate	5 – 10	Hz
Trigger suppression factor needed	$10^4 - 10^5$	

Table 7: Central data acquisition parameters [44].

3.1 Background Sources

The background is mainly caused by processes other than ep collisions. HERA suffers from the problems of *pp* machines as well as those of *ee* machines. The *ep* cross section is small in comparison to that of protons colliding with beam residual gas and the electrons cause a relatively poor vacuum due to synchotron radiation.

Not only is the background situation at its worst, but also the time between two bunch crossings (96 ns) is very short and leads to problems in event classification. Table 8 compares the parameters of HERA with other current or planned machines.

[2] 1995: Additional 214000 channels from the central and backward silicon tracker detector.
[3] About 100 kHz at design luminosity.

parameter	TEVATRON	LHC [4]	HERA	LEP	unit
Particles collided	$p\bar{p}$	pp	ep	ee	
σ_{physic}	$40 \cdot 10^6$	$80 \cdot 10^6$	$10 \cdot 10^3$ [5]	≤ 40 [6]	nb
σ_{gas} [7]	$A^{\frac{2}{3}} \cdot 40 \cdot 10^3$	$A^{\frac{2}{3}} \cdot 40 \cdot 10^3$	$A^{\frac{2}{3}} \cdot 40 \cdot 10^3$	150	μb
$\frac{\sigma_{\text{physic}}}{\sigma_{\text{gas}}}$	$\frac{1}{6}$	$\frac{1}{6}$	$\frac{1}{24000}$	$\frac{1}{3800}$	
Luminosity $\mathcal{L}$	$7.5 \cdot 10^{30}$	10^{34}	$1.6 \cdot 10^{31}$	$1.1 \cdot 10^{31}$	cm^{-2}s^{-1}
Beam current I_p	6.9 (p) 2.0 ($\bar{p}$)	536	163	—	mA
Beam current I_e	—	—	58	3	mA
Vacuum	10^{-9}	10^{-9}	10^{-7}	10^{-7}	Pa
Beam life time	10 – 40	10	3 – 10	20	h
Bunch distance	3.5	0.025	0.096	11	μs
Beam energy	0.9 – 1.0	7.0	0.03 0.82	0.055	TeV

Table 8: Background situation at different kind of colliders [31].

The main sources for background events are:

- **Proton Beam Pipe Interaction:** Off-momentum protons hit the beam pipe structure, mostly collimators, upstream from the detector. At design luminosity a rate of 50 kHz is expected in the interaction zone. Electron beam pipe interactions are of less importance due to smaller beam current and the shorter produced particle shower.

- **Proton Gas Interaction:** Protons may hit residual gas molecules within the interaction zone. The cross section for such processes is given by $\sigma_{pN} = A^{2/3} \cdot 40$ mb with A the atomic mass of the nucleon N hit by the proton. These interactions are enhanced by the relatively bad vacuum due to the synchotron radiation of the electrons. The proton gas interaction rate can be estimated as 1 kHz/m for design luminosity and a vacuum of 10^{-7} Pa. Electron gas interactions are negligible due to the small cross section $\sigma_{eN} \approx 200$ μb.

- **Synchotron Radiation:** Electrons and protons are accelerated in separate beam pipes. However at the interaction point they have to cross each other at an angle of 20 mrad. This is achieved by bending the electron beam with a radius of

[4] The triggering task at LHC is not so much to suppress background interactions but to select the searched processes from the average of 10 to 20 pp collisions per bunch crossing.

[5] The photoproduction cross section at H1 was determined as $\sigma^{ep}_{\text{tot}} \approx 11$ μb [6], other physic processes have much smaller cross sections.

[6] LEP at the Z^0 resonance energy.

[7] A = atomic mass of the residual gas nucleon hit by the proton; $A \approx 16$ [46].

1360 m over a length of 13.6 m. As this happens just a few meters away from the interaction point, synchotron radiation is seen in the detector.

- **Cosmic Rays:** Cosmic muons crossing the interaction zone of the detector, are background events for leptonic decays of mesons containing heavy quarks such as J/ψ.

3.2 The H1 Trigger Scheme

Given the constraints above, it is obvious that a final trigger decision cannot be found in a single step. H1 has therefore a trigger system with four levels in order to reduce dead time. Each level is only started when the event has been accepted by the previous level. An overview is given in Figure 12 and in Table 9.

To reduce the overall dead time, the first trigger level (L1) is designed to be dead time free. It makes use of pipelines to store the data. This extends the decision time to 2.3 μs despite the short bunch crossing time of 96 ns.

The L1 trigger has to deal with an input rate of about 50 kHz. At a positive level 1 decision (L1-Keep) the pipelines are stopped and the level 2 trigger (L2) is started. It is allowed to use 20 μs to send a L2-Keep otherwise the event is rejected. In the case of an acceptance the front end processors start to read-out the data. In parallel, a flexible level 3 trigger system (L3) refines the decision. The L3 trigger has to send a L3-Keep or a L3-Reject signal. On a reject signal the data readout of the front end processors is interrupted and a front end ready (FER) signal is sent. At this signal all pipelines are cleared and all front end components are prepared for data taking. In case of a L3-Keep the data readout is completed before a FER signal is sent to get ready for the next event. The level 4 trigger (L4) [47], a processor farm, works asynchronously on the full event data. All data passing the L4 processor farm are written to a storage device.

Each L1 trigger makes its decision on the data from its own trigger subsystem. Due to the short decision time the L1 and L2 triggers have to be hardware triggers. Nevertheless neural networks are becoming fast enough to fulfill the requirements as has already been shown in one proposal [48]. The data from all trigger subsystems, a subsample of the full event data, are available to the L2 trigger to operate on. The input data for L3 are the same as for L2 but it is designed as a software trigger. Its decision time is finite but not yet fixed. It has to be shorter than the total readout time of the front end because it is meant to interrupt the readout. The design decision time is 800 μs.

The length of the pipelines and therefore the decision time available to L1 were kept as short as possible. The reason for this was mainly cost. Memory was expensive at the time when HERA was planned. For future experiments this has to be considered carefully because a shorter decision time requires the triggers to be more complicated if they have to fulfill the same tasks. The costs of memories for the pipelining has to be weighed against additional costs of more complicated electronic circuits.

There is also a minimum length for the pipelines. It has to be longer than the maximum drift time of the drift chambers, which is of the order of 1 μs, to give the

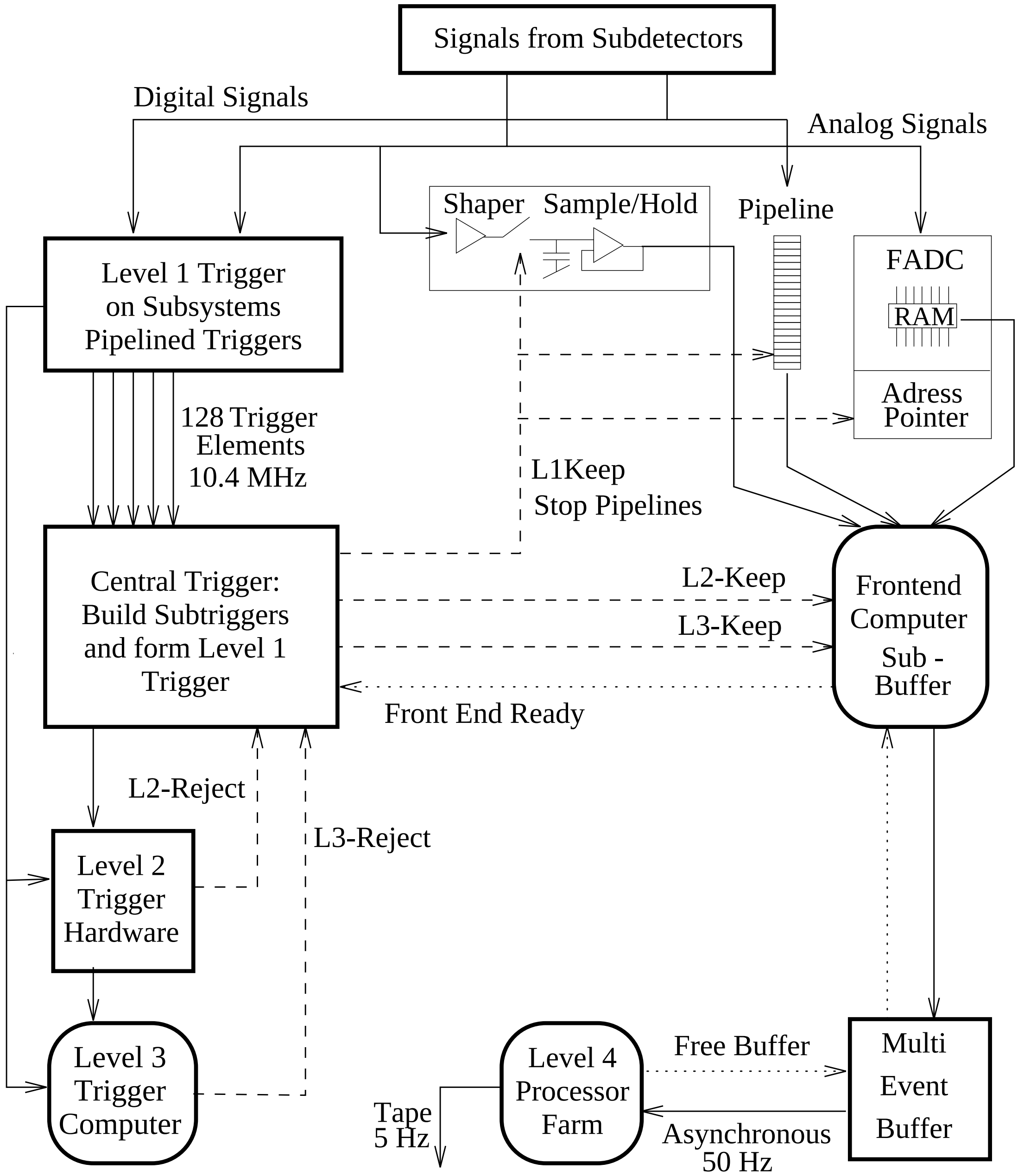

Figure 12: The H1 trigger concept with indicated data flow and steering signals from the H1 trigger and the data acquisition system.

first level trigger the opportunity to have all information available for its decision. Also propagation delays in cables in this size of experiment of a few hundred nano-seconds are no longer negligible. The time until the trigger decision is distributed to the various spatially separated subsystems has also to be included in the pipeline length.

The ultimate goal of the L4 trigger would be to run the whole event reconstruction program on the event data to get all physical variables before coming to a decision.

The L4 input rate is limited by the transfer rate of the data from the subsystem and by the computing power available in the processor farm. The front end readout speed is limited to about 40 Hz for 60 kByte sized events. At higher data rates significant dead time is introduced. The output data flow of the processor farm has to be smaller than the amount of data the storage device is capable of storing.

trigger level	level 1	level 2	level 3	level 4	level 5
Maximum decision time	2.5 μs	20 μs	800 μs		
Input event rate	$\approx$ 50 kHz			50 Hz	5 – 10 Hz
Output event rate	50 Hz			5 – 10 Hz	5 – 10 Hz
Designed output event rate	1 kHz	200 Hz	50 Hz	5 – 10 Hz	5 – 10 Hz
Introduced dead time	0 μs	20 μs	$<$ 800 μs		
Data	from own subtrigger system	from all subtrigger system	from all subtrigger system	from all detectors	from all detectors
Implementation	hardware, front end subsystem, synchro-nous	hardware, front end system, synchro-nous	software, front end processor, synchro-nous	15 RISC[8] VME[10] processors, synchro-nous	SGI[9] , asynchro-nous
Action	stop data pipeline	start data readout	start event building or abort data readout	verification of trigger decision, event filtering	event recon-struction, event clas-sification

Table 9: Overview of the H1 trigger levels.

[11]Reduced Instruction Set Computer.
[12]Silicon Graphics Inc.
[13]Versatile Module Europe [67].

3.3 The First Level Triggers

To have a powerful trigger system to reject background a combination of information from different subsystems, i. e. of energy measurement and precise tracking information is necessary.

The L1 trigger consists of different trigger subsystems based on the information of certain subdetectors. They are shown in Figure 13. Each of them provides some output. They are called trigger elements. They are fed into the central level 1 trigger (CTL1) [49], where groups of trigger elements can be combined to form any possible logic which can produce a L1-Keep. These logics are called subtriggers. The CTL1 can handle up to 128 of these subtriggers.

To adjust the trigger to different run conditions, as high or low luminosity or large or small background rates, it is possible to prescale each subtrigger individually. Only a certain fraction of a subtrigger leads to a L1-Keep signal and is read-out. This procedure allows the recording of very rare occurring events within the large amount of photoproduction events.

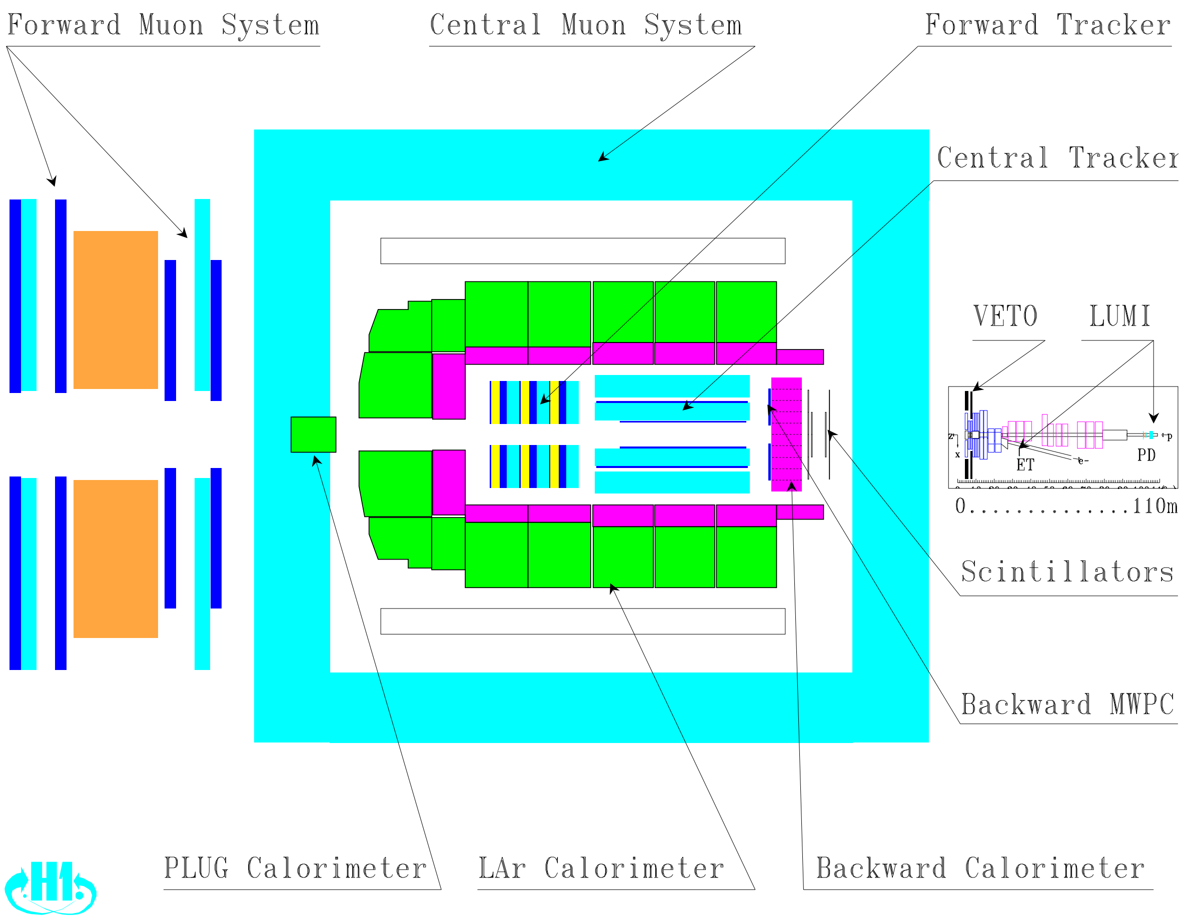

Figure 13: From the first level triggers used detector components.

In the following, the trigger subsystems are described:

- **Cosmic Scintillators:** Large scintillators located at bottom of the H1 detector are used to trigger cosmic ray events mainly for calibration of the detector.
- **Time of Flight System** [50] **:** Two scintillator walls are located upstream behind the BEMC to veto background events with a primary vertex upstream. Particles with a vertex within the detector have a longer distance to the scintillator walls than particles coming from upstream. The time difference is about 12 ns as Figure 14 shows.

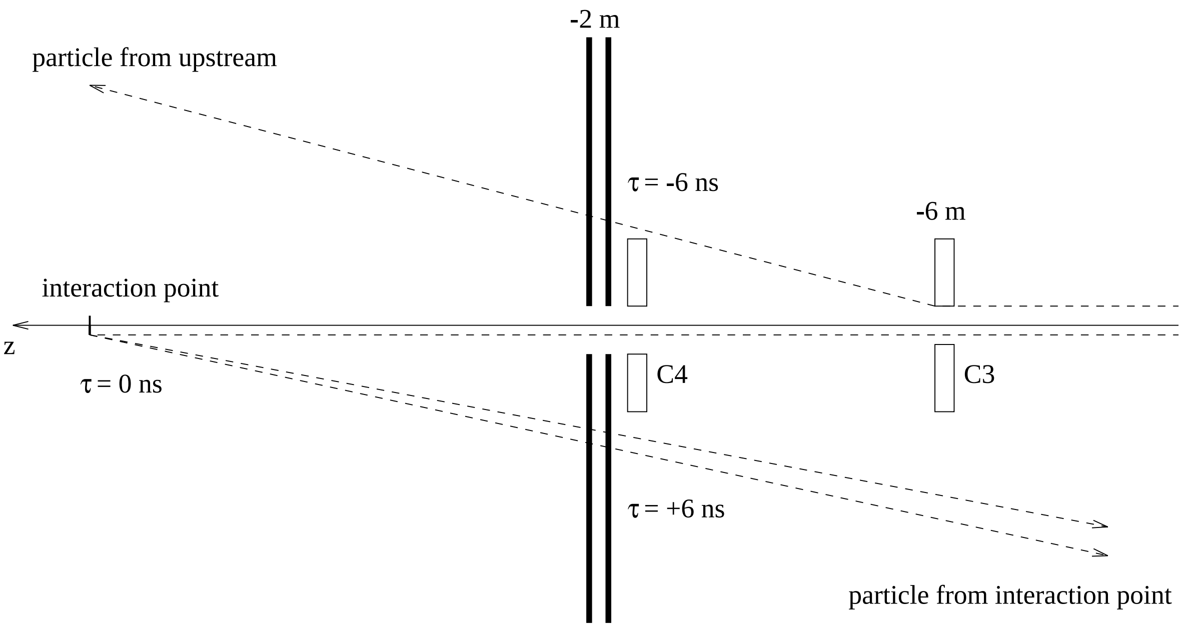

Figure 14: The time of flight system (ToF) determines the primary interaction vertex by measuring the time in respect to the HERA bunch clock at which particles pass two scintillator walls. C3 and C4 are two collimators which protect the detector from synchrotron radiation.

- **Veto Wall** [50] **:** Two further upstream scintillator hodoscopes to recognize beam halo.
- ***z*-Vertex Trigger** [51] **:** The central and forward multiwire proportional chambers are used to estimate the event vertex position along the beam axis. A histogram is filled with the z coordinate on the beam axis of all combinations of possible rays, straight lines, formed by the fired pads of the multiwire proportional chambers as shown in Figure 15. The trigger looks for a significant peak in the histogram as well as providing a good time measurement. The achieved resolution in z is 5.5 cm.
- **Forward Ray Trigger** [52] **:** From the six layer multiwire proportional chamber in the three modules in the forward tracking system trajectories with an origin

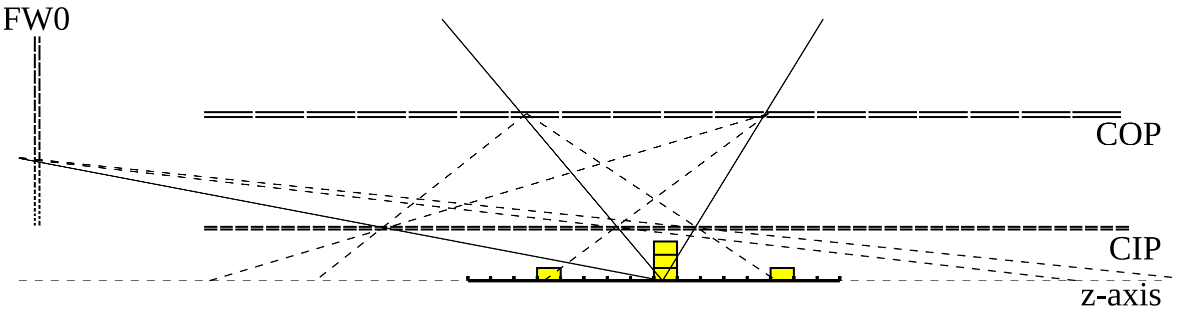

Figure 15: Schematic view of the z-vertex trigger. The z coordinate of the vertex position is reconstructed by the z-vertex trigger by filling a histogram with the z coordinate on the beam axis of all possible straight lines formed by the fired pads of the multiwire proportional chambers. The solid lines indicate the real tracks, the dashed lines the fake tracks found by the z-vertex trigger.

in the interaction zone are searched. It is possible to require a certain number of such roads for the acceptance of an event.

- **Drift Chamber r-φ Trigger** [53] **:** The information of the two central jet chambers are used to find charged particles in the r-φ projection originating from the beam axis. It is described in more detail below.

- **Drift Chamber r-z Trigger** [54] **:** Using the information of the z drift chambers and the central multiwire proportional chambers the vertex along the beam axis is reconstructed. This trigger was not available in 1993.

- **Backward Multiwire Proportional Chamber Trigger:** Three out of the four plains of the backward multiwire proportional chamber are required to register a hit for delivering a trigger signal.

- **Liquid Argon Calorimeter** [55] **:** The energy flow in the liquid argon calorimeter is measured. The total, missing and transverse energy based on the energy deposition in the calorimeter is calculated in the front end electronics.

- **Backward Electromagnetic Calorimeter** [56] **:** The deposited energy of the scattered electron is measured in a cluster of the scintillator cell. The threshold on the energy content of such a cluster can be set.

- **Central Muon System** [57] **:** One or more muons in certain areas of the detector can be required as a trigger criteria. The signals are derived from the streamer tubes in the iron yoke.

- **Forward Muon System** [58] **:** The forward muon system is used to find muon candidates produced at a very small angle ϑ to the beam axis.

- **Electron Tagger** [59] **:** The electron detector (e-tagger) of the luminosity system is used to trigger on electrons scattered at very low angle ($\vartheta \leq 5$ mrad). Also a coincidence with the photon detector can be required.

4 The Drift Chamber r-φ Trigger

4.1 Principles of Operation

The aim of the drift chamber r-φ trigger is to find tracks from the interaction point in the r-φ projection with a transverse momentum larger than 420 MeV/c in a dead time free manner and assign them to the correct bunch crossing. The trigger obtains the information from ten layers of the central jet chambers, seven layers of the inner CJC1 and three of the outer CJC2. A radial view of the central tracking area of the H1 experiment is shown in Figure 16. A layer consists of the sense wires with an equal distance to the center of the chamber. The chamber pulses of the ten layers are discriminated and synchronized with a frequency ν of 10.4 MHz or 20.8 MHz. The resulting bits correspond to drift pads of 5 mm and 2.5 mm respectively at a typical drift velocity of the central jet chambers of 50 μm/ns.

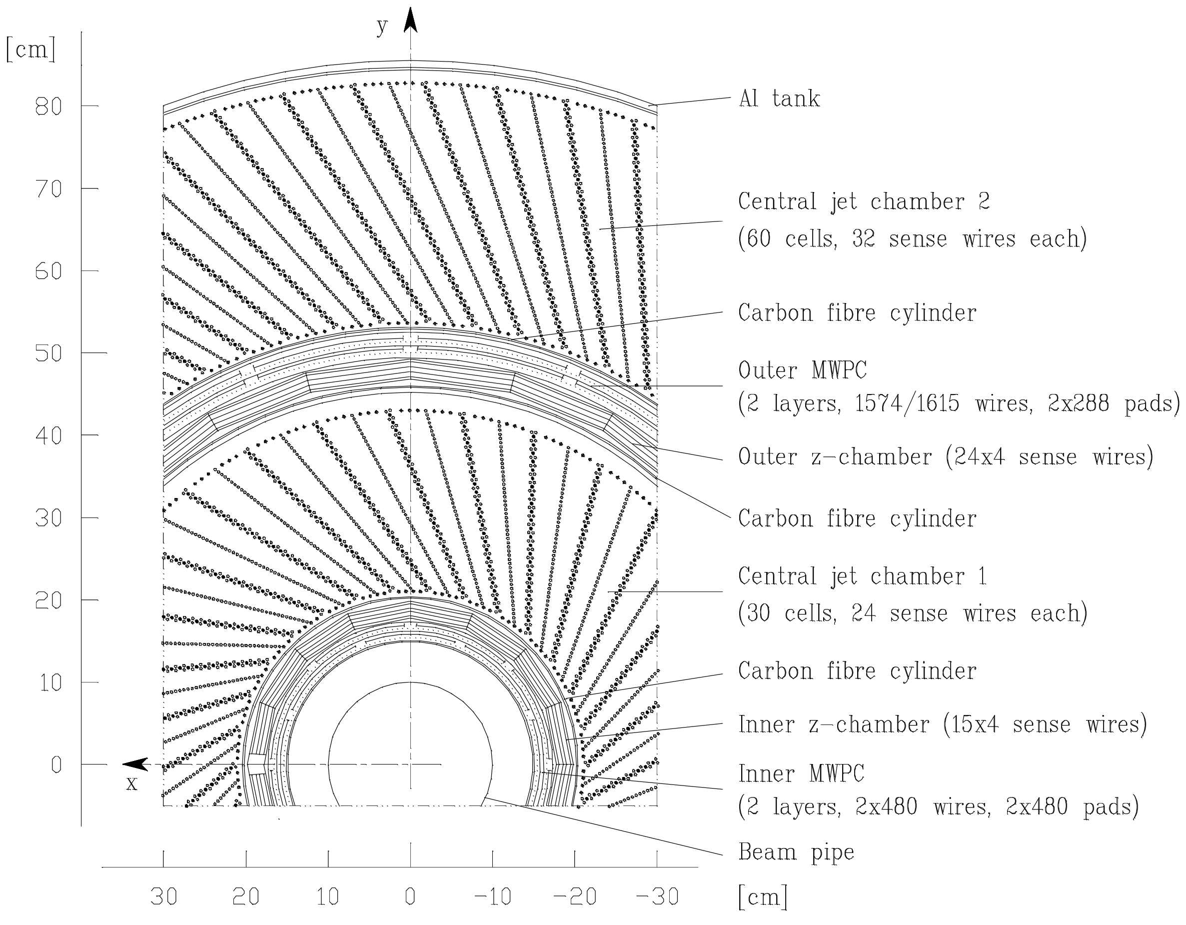

Figure 16: Radial view of the H1 tracking system [40].

In this way the trigger builds up a digitized picture of the chambers with the discriminated signals. At constant drift velocity the drift time is associated with two points in the r-φ plane, symmetric with respect to the sense wire plane. The trigger searches for tracks by comparing the points in the r-φ plane with programmed masks, called roads.

The available time to take a decision is 2.1 μs. The time left between the arrival of signals from hits with the maximum drift time of 1.1 μs, and the end of the L1 decision time is 1 μs which is available to find the tracks. Because the trigger has to provide an output every 96 ns, the operation has to be done in a pipelined fashion (see Appendix A).

The trigger calculates the multiplicity of tracks in four transverse momentum ranges as well as the topology of the event in the r-φ plane. The φ resolution of the output of the trigger was in 1993 increased from a 15 fold segmentation to a 45 fold segmentation. The four transverse momentum ranges are arranged as follows:

- positively charged tracks with 420 MeV/c to 800 MeV/c transverse momentum respectively i. e. -0.90 m^{-1} to -0.45 m^{-1} in curvature.
- positively charged tracks with 800 MeV/c to infinite transverse momentum respectively i. e. -0.45 m^{-1} to 0.00 m^{-1} in curvature.
- negatively charged tracks with 420 MeV/c to 800 MeV/c transverse momentum respectively i. e. 0.45 m^{-1} to 0.90 m^{-1} in curvature.
- negatively charged tracks with 800 MeV/c to infinite transverse momentum respectively i. e. 0.00 m^{-1} to 0.45 m^{-1} in curvature.

The central level 1 trigger (CTL1) is not able to handle large numbers, but only expects logical values. Therefore it is required to put a threshold on the various multiplicities. In addition time information is provided. Because each track with a transverse momentum larger than 400 MeV/c crosses at least once the sense wire plane, every mask can be combined with a drift pad, where the drift time is smaller than the time between two consecutive bunch crossings. The signal of this particular drift pad is called prompt bit and assigns the correct bunch crossing to the road. This time of the event is called t_0 time. The provided trigger elements in 1993 are listed in Table 10.

In the r-φ plane tracks appear as circles and can be parameterized with their curvature, the distance of closest approach (DCA) and the azimuth angle at the DCA point. A circle is determined by three well measured points some distance from each other. Therefore the track is measured with a good accuracy at the beginning, in the middle and at the end of the trajectory. To insure that the three well measured points belong to one track and to have some redundancy seven additional layers are measured and included in the track finding. To assign to each track also the correct bunch crossing, the prompt bit has to be measured as well. To be able to find the prompt bit for each track within the 420 MeV/c to infinite transverse momentum range, it is necessary to read out almost every layer of the CJC1, because most of the tracks have a prompt bit on only one layer. The wire having the prompt bit of the track is called the reference wire of this track.

Further on we will use the variable curvature κ instead of the transverse momentum p_t. The curvature κ is measured in the r-φ plane and is a constant for a track if the

trigger element	description
DCRPhi_T0	at least one tracks with $p_t > 420$ MeV/c validated with the corresponding prompt bit of the mask.
DCRPhi_Ta	at least one track with $p_t > 420$ MeV/c.
DCRPhi_Tb	at least two tracks with $p_t > 420$ MeV/c.
DCRPhi_Tc	at least three tracks with $p_t > 420$ MeV/c.
DCRPhi_TPos	at least one positively charged track with $p_t > 420$ MeV/c.
DCRPhi_TNeg	at least one negatively charged track with $p_t > 420$ MeV/c.
DCRPhi_TLow	at least one track with 420 MeV/$c < p_t <$ 800 MeV/c.
DCRPhi_THigh	at least one track with $p_t > 800$ MeV/c.

Table 10: Provided trigger elements in 1993 by the drift chamber r-φ trigger.

magnetic induction B is perpendicular to the r-φ plane and the energy loss of the particle is neglected. The two variables κ and p_t are related as follows

$$\kappa = \frac{1}{r} = \frac{ze \cdot B}{p_t} \tag{60}$$

where ze is the charge of the particle. The sign of the curvature κ is defined in Figure 36 in Section 6.1.

There are different possible algorithms to generate the roads the trigger uses for comparison [60]. The algorithm used covers the κ-φ plane with sections formed from four arcs of circles. These sections are called roads. These four circles are given by the interaction point, one out of two points around the reference point and two points at a fixed distance from the interaction point. The reference points essentially vary the parameter φ in the κ-φ plane. The distance between two points at the fixed radius spans the curvature interval of the roads. The roads have to be generated so that they cover the whole κ-φ plane between the transverse momentum boundaries. The roads are bounded by arcs given by the following points:

- the interaction point.

- an interval around the reference point. It is also the reference wire of the road. It has to be an interval around the reference point in order to avoid holes in the κ-φ plane. The width of the interval is small in comparison to the drift distance of the electrons drifting in 96 ns.

- two points at the position of layer 29. This radius is chosen arbitrarily and is located at a radius of 58.7 cm. The interval between the two points is about 7 mm; the distance between two neighbouring intervals is small. The variation of these parameters leads to different overlaps between the roads.

This generation of masks is visualized in Figure 17.

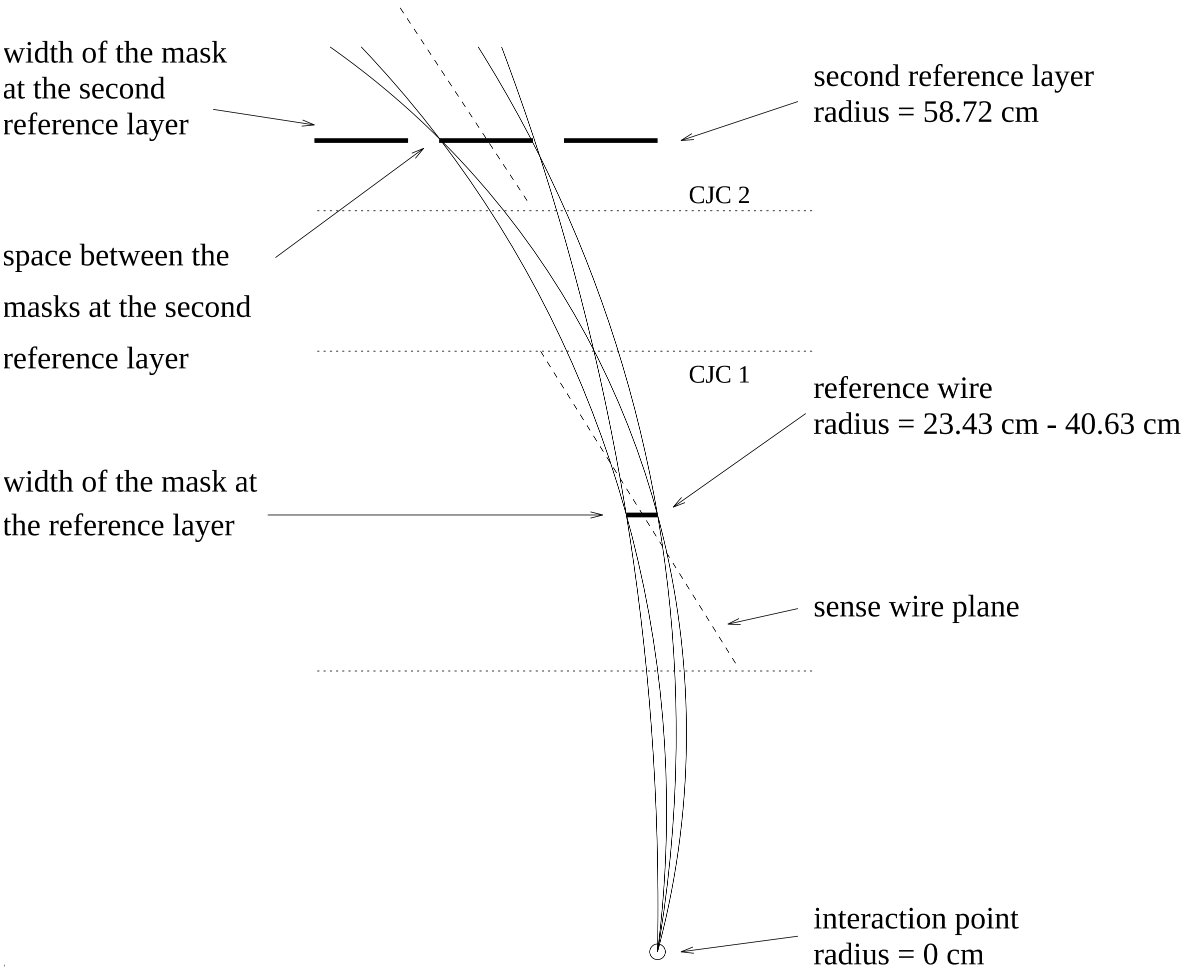

Figure 17: Generation of the masks. The masks consist of all drift pad at the measurement layers which are at least partly covered from the area defined by the four arcs.

The non linear behaviour of the electron drift near the sense wires is taken into consideration with a close wire approximation. The measured smaller drift velocity near the sense wires is parameterized as a function of the distance to the sense wire and is used for the calculation of the drift time. The constants used to generate the roads for the 1993 runs are listed in Table 11.

parameter	value
Transverse momentum limits	-400 MeV/c, 400 MeV/c
Drift velocity	53 μm/ns
Lorentz angle	45°
Layer of second reference wires	29
Distance between two masks at the second reference layer	1.5 BC
Space between two masks at the second reference layer	0.1 BC
Width of the mask in the reference point	0.0015 BC
Rotation between CJC1 and CJC2	$-0.05°$

Table 11: Parameters of the road generation for the setup of 1993. BC is the drift distance covered in one bunch crossing. BC = 96 ns $\cdot\, v_{\mathrm{drift}}$.

A cluster of 15 to 20 roads belongs to each reference wire. The number of roads depends on the distance between reference wire and interaction point. Due to the constant intervals at the position of layer 29, masks with a larger distance between interaction point and reference point cover a larger curvature range. Therefore for this reference points the number of roads is decreasing. Unfortunately these circumstances produce a slightly different granularity for the roads from different reference wires. The total number of roads the trigger is looking for adds up to about 10000. This number depends on the drift velocity and the Lorentz angle. The roads are generated symmetrically for positively and negatively charged tracks. Nevertheless the behaviour is different for positively and negatively charged tracks due to the tilt of the central jet chamber cells by 30°. Negatively charged tracks cross more wire planes and cell boundaries and their ionization length is longer than for positively ones.

Not all layers of the central jet chambers are used. The information had to be restricted in order to get to a decision within 1 μs. Most of the information is taken from the inner jet chamber, because less wires have to be read-out to cover the whole φ range. In addition all wires near the boundaries of the chamber are excluded because they are less efficient due to inhomogeneities in the electrostatic drift field. To make the trigger more stable against noise and sparking, three layers of the outer jet chamber are also required. To obtain a better resolution to determine the curvature of a track in the inner center and outer areas the time information is measured with double accuracy as already mentioned above.

To be less dependent on the performance of the two jet chambers not all ten layers are required to accept a track. Only four of the inner five layers and four of the outer five layers are necessary. For the time information, which is received in the prompt bit of a track, the requirements cannot be weakened. If the prompt bit is missing due to inefficiency , the validated t_0 mask will not fire. Therefore the additional factor on the efficiency for the validated t_0 masks of the trigger is proportional to the efficiency of the chambers.

A trigger mask consists of all drift pads which lie within the area surrounded by the four arcs described above. Two different types of masks are generated out of these roads. One type of masks consist of the drift pads of the ten measurement layers. They are called standard masks. To derive a more accurate time information for a second type of masks the prompt bit is also required. These masks are called validated t_0 masks.

This mechanism of generating roads provides a rather robust design. Due to the overlapping of the masks even at the malfunction of a single mask the corresponding κ-φ area is still covered from adjacent masks, however not with the same redundancy. The overlapping design of the masks provide also a sharp separation between the transverse momentum ranges between which the trigger distinguishes. The disadvantage of this mechanism is the resulting double counting. The probability that one track matches to different roads rises as more of the roads overlap. This influences the performance of the trigger elements DCRPhi_Tb and DCRPhi_Tc in which more than one track is asked for.

All this led to using the layers of the central jet chambers in the following way. Layers 2, 4, 8, 12, 16, 20 and 22 of the inner jet chamber and layers 27, 29 and 31 of the outer jet chamber are used to detect tracks. For a later extension layers 6, 10, 14, 18 and 25 are also processed in the same way but are not used for track finding. In addition, layers 2 to 21 are needed as reference wires to get the time information to assign the correct bunch crossing to the tracks. All layers are synchronized at 10.4 MHz with the exception of layers 2, 4, 18, 20, 29 and 31 which are synchronized at 20.8 MHz to perform the high resolution to measure the circle more accurately. In Table 12 the specifications are summarized.

For a global single wire efficiency of the central jet chamber the maximum resulting trigger efficiency can be calculated. The trigger efficiency $\epsilon_{\mathrm{trigger}}$ of an n out of m logic as a function of the single wire efficiency ϵ_{wire} can be written as

$$\epsilon_{n/m} = \sum_{i=n}^{m} \binom{m}{i} \cdot (\epsilon_{\mathrm{wire}})^{i} \cdot (1-\epsilon_{\mathrm{wire}})^{n-i} \quad . \tag{61}$$

For the ‘five out of five logic’, ten wires have to be there and the trigger efficiency $\epsilon_{\mathrm{trigger}}$ is given by

$$\epsilon_{\mathrm{trigger}} = (\epsilon_{\mathrm{wire}})^{10} \quad . \tag{62}$$

For the ‘four out of five logic’ in each group of five wires one wire can be missing. The trigger efficiency $\epsilon_{\mathrm{trigger}}$ can be written as

inner central jet chamber					
layer	radius	synchronization frequency	number of bits per layer	drift pad width for road finding	function
2	23.43 cm	20 MHz	10	0.5 BC	meas. & ref. wire
3	24.26 cm	10 MHz	1	1.0 BC	ref. wire
4	25.10 cm	20 MHz	12	0.5 BC	meas. & ref. wire
5	25.95 cm	10 MHz	1	1.0 BC	ref. wire
6	26.81 cm	10 MHz	7	1.0 BC	ref. wire
7	27.69 cm	10 MHz	1	1.0 BC	ref. wire
8	28.57 cm	10 MHz	7	1.0 BC	meas. & ref. wire
9	29.46 cm	10 MHz	1	1.0 BC	ref. wire
10	30.36 cm	10 MHz	7	1.0 BC	ref. wire
11	31.27 cm	10 MHz	1	1.0 BC	ref. wire
12	32.18 cm	10 MHz	9	1.0 BC	meas. & ref. wire
13	33.10 cm	10 MHz	1	1.0 BC	ref. wire
14	34.03 cm	10 MHz	9	1.0 BC	ref. wire
15	34.96 cm	10 MHz	1	1.0 BC	ref. wire
16	35.89 cm	10 MHz	9	1.0 BC	meas. & ref. wire
17	36.83 cm	10 MHz	1	1.0 BC	ref. wire
18	37.77 cm	20 MHz	11×2	1.0 BC	ref. wire
19	38.72 cm	10 MHz	1	1.0 BC	ref. wire
20	39.67 cm	20 MHz	11×2	1.0 BC	meas. & ref. wire
21	40.63 cm	10 MHz	1	1.0 BC	ref. wire
22	41.58 cm	10 MHz	11	1.0 BC	meas. wire

outer central jet chamber					
layer	radius	synchronization frequency	number of bits per layer	drift pad width for road finding	function
25	55.32 cm	10 MHz	7	1.0 BC	
27	57.01 cm	10 MHz	7	1.0 BC	meas. wire
29	58.72 cm	20 MHz	7×2	1.0 BC	meas. wire
31	60.45 cm	20 MHz	5×3	1.5 BC	meas. wire

Table 12: Layers of the central jet chamber used by the drift chamber r-φ trigger. BC is the drift distance covered in one bunch crossing. BC $= 96$ ns $\cdot\, v_{\mathrm{drift}}$. The abbreviations meas. wire and ref. wire mean measurement wire and reference wire.

$$
\begin{aligned}
\epsilon_{\text{trigger}} &= \left(\epsilon_{4/5}\right)^2 \\
&= \left(5\cdot(\epsilon_{\text{wire}})^4\,(1-\epsilon_{\text{wire}}) + (\epsilon_{\text{wire}})^5\right)^2 \quad . \qquad (63)
\end{aligned}
$$

For the mask with reference wire an additional condition to the four out of five logic is required. Because 6 of the 20 reference wires are identical to the normal measurement wires the trigger efficiency $\epsilon_{\text{trigger}}$ can be written for this case under the condition that all masks have the same probability

$$
\begin{aligned}
\epsilon_{\text{trigger}} &= \frac{14}{20}\cdot\left(\epsilon_{4/5}\right)^2\cdot\epsilon \;+\; \frac{6}{20}\cdot\epsilon_{4/5}\cdot\epsilon\cdot\epsilon_{3/4} \\
&= \frac{14}{20}\cdot\left(5\cdot(\epsilon_{\text{wire}})^4\,(1-\epsilon_{\text{wire}}) + (\epsilon_{\text{wire}})^5\right)^2\cdot\epsilon_{\text{wire}} \;+ \\
&\quad \frac{6}{20}\cdot\left(5\cdot(\epsilon_{\text{wire}})^4\,(1-\epsilon_{\text{wire}}) + (\epsilon_{\text{wire}})^5\right)\cdot\epsilon_{\text{wire}}\cdot \\
&\quad \left(4\cdot(\epsilon_{\text{wire}})^3\,(1-\epsilon_{\text{wire}}) + (\epsilon_{\text{wire}})^4\right) \quad . \qquad (64)
\end{aligned}
$$

The maximum trigger performance is shown in Figure 18 as a function of the central jet chamber single wire efficiency.

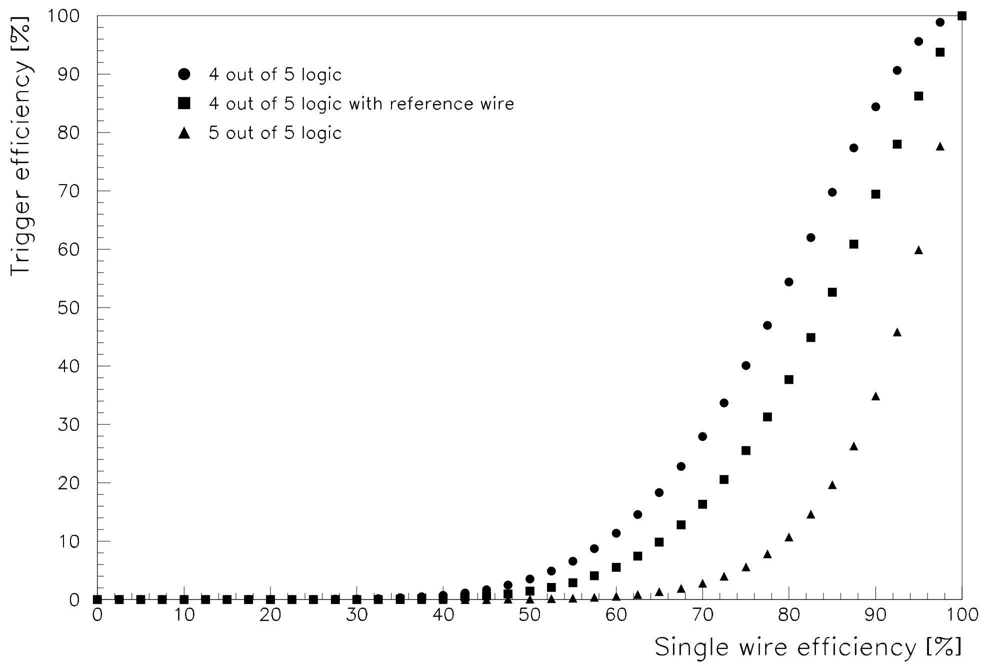

Figure 18: Maximum trigger efficiency as a function of the single wire efficiency of the central jet chambers.

4.2 Implementation

The alignment of the coincidence for the track finding algorithm is strongly dependent on the drift velocity and the Lorentz angle. The design of the trigger has to be flexible enough to be able to adjust to changes of the drift velocity or Lorentz angle in the chamber. Therefore most of the trigger logic is built with XILINX logic cell arrays (LCA) [61]. They offer both high integration and flexibility in the logic design, as they can be modified from a computer at any time. Appendix C further explains their architecture. In case of a change of the chamber parameter a new code can be loaded into the LCAs.

The electronics of the drift chamber r-φ trigger are split into several parts because of the spatial structure of the H1 experiment. The trigger hardware consists of 10 different printed circuit boards listed below:

- **870 ASD[14] Cards:** They amplify, shape and discriminate the pulses of the central jet chamber.
- **150 Adapter Cards:** They connect up to eight ASD cards with the FADC[15] cards. The distribution of the discriminator thresholds is also provided.
- **30 Receiver Cards:** They synchronize the signals from the adapter cards. In addition they contain the logic to adjust the discriminator threshold of the ASD card and a facility to feed the lines with a test pattern instead of signals.
- **15 SRL1[16] Cards:** They contain the shift registers, the track finding logic and the local clustering unit where the output of the track finding is summarized.
- **L1L2[17] Card:** This board controls the whole trigger. It calculates the various trigger elements and contains the data memory for the readout.
- **L2L3[18] Card:** It is the interface between the drift chamber r-φ trigger and the PQZP[19] [62] bus which provides the data to the higher level triggers.
- **Delay Card:** It distributes the HERA clock to the different crates. The clock phases can be adjusted for each line separately.
- **2 Clock Cards:** They distribute the HERA clock within the receiver crates.
- **Active Backplane:** It distributes the signals from the receiver cards to the SRL1 cards.
- **Passive Backplane:** It distributes the trigger bits and the shift register bits from the SRL1 cards to the L1L2 card.

[14] Amplifier, Shaper, and Discriminator
[15] Flash Analog Digital Converter
[16] Shift Register and Level 1 trigger logic
[17] Level 1 control logic and interface to Level 2 trigger
[18] Interface to Level 2 and Level 3 triggers
[19] Pipeline Quickbus Zero suppression Parallel input/output

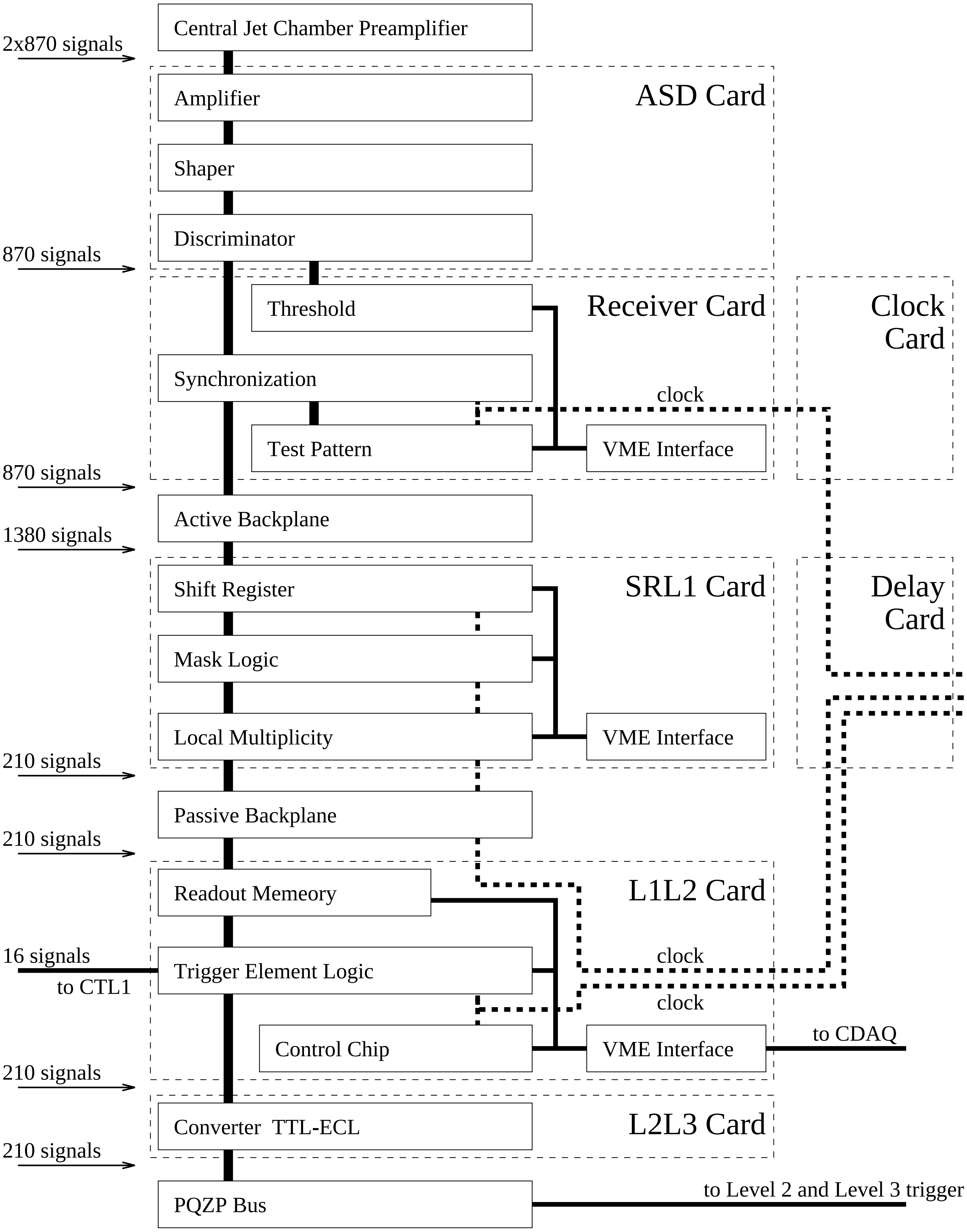

Figure 19: Schematic overview of the drift chamber r-φ trigger.

There are two receiver crates which contain the receiver, delay and clock cards. In the trigger crate the SRL1, L1L2 and L2L3 cards are located. There is a fourth crate, called the STC[20] crate. It contains all boards, which communicate with the central level 1 trigger (CTL1). There are the fast card [63], the slow card [64],the trigger bit card [66] and the fanout card [65]. In addition two fanout cards are needed to distribute and delay the control signals, one for the drift chamber r-φ trigger, one for the PQZP bus, which is also located in this crate and consists of 4 PQZP store cards and a PQZP L2L3 card. To communicate between these four crates in each of them a VME inter connect card (VIC) [68] is installed. A Macintosh IIx computer is also connected to this bus system. This computer is needed to control and load the trigger hardware. For the readout a front end processor (FIC) [69], which has access over the same bus to the data at the L1L2 card, is located in this crate. To deliver the data to the central data acquisition (CDAQ) there is a second VIC in this crate. This has the advantage that the readout and the data transfer to the CDAQ are independent and cannot disturb each other. A schematic overview is given in Figure 19.

The 2640 central jet chamber wires are read-out on both sides of the chamber. The 5280 signals are preamplified just outside the chamber. Over a 30 m long cable always 16 differential signals are connected with a FADC card, where the signals are stored for the readout. For the trigger the signals are also bypassed to the front of this card. For the trigger 870 of the 2640 wires are used. Because analog signals are much more prone to noise than digital the discriminators are plugged directly on the FADC cards to minimize the length of the analog signal cables. The signals from both ends are treated separately. They are first amplified, then shaped and finally discriminated. After the discrimination the two digital signals of both ends of a wire are 'ORed'. This leads to a better resolution than if they were to be 'ORed' before the discrimination.

The signals reach the receiver cards over 20.5 m long cables. The discriminator thresholds are set from the receiver cards as analog signals over the same cables. The thresholds can be steered for groups of eight wires in a range of -1 V to 1 V. The resolution of the DAC is 12 bits in steps of 0.5 mV. At the receiver cards the signals are synchronized with a frequency ν of 10.4 MHz or 20.8 MHz. After the synchronization there is a logic to switch on single wires permanently. This allows broken wires to be masked out. Up to the synchronization the timing of the signals is very critical. To compensate different propagation delays of the various cables it is possible to install delays for groups of eight wires before the synchronization. After the synchronization the tolerances for the timing are much larger. They are given by the synchronization frequency ν and are 96 ns or 48 ns. On the receiver card is also a facility to feed the synchronized part of the trigger with artificial signals, called test patterns, is provided. Patterns of digital signals with a frequency of 10.4 MHz can be tested. The memory has a depth of 4096 bunch crossings. These test patterns are a considerable help in debugging the trigger.

The 29 differential signals of each of the 30 receiver cards are connected to the active backplane over a 80 cm long twisted pair cable. On this backplane the 870 signals are distributed to the 15 SRL1 cards. Each of them has 92 input signals. Because some information is also used in the neighbouring SRL1 card some lines from the receiver

[20] Subsystem Trigger Controller

cards are split.

The 92 input signals of the SRL1 card are stored in shift registers with parallel outputs due to the long drift time of the chambers. The outputs of the shift registers put up a local net of 398 signals with 4860 inputs in the trigger logic. The shift registers and the trigger logic make use of the XILINX logic cell arrays (LCA).The algorithm used to find tracks works in parallel and is synchronized. All tracks belonging to a bunch crossing are found at the same time. In the local clustering unit of each of the 15 SRL1 cards the identified tracks are assigned to the four transverse momentum ranges and the three φ ranges. For each κ-φ range, a bit is set, if one or more corresponding tracks are found. In addition two time information bits, one for positive, one for negative particle tracks are provided from the local clustering unit. Whenever a prompt bit of an identified track is present, the information is collected. Each of the 15 SRL1 cards produce information containing 14 bits. These are called trigger bits, because they contain the trigger information.

In Figure 20 the concept of track finding of the drift chamber r-φ trigger is explained.

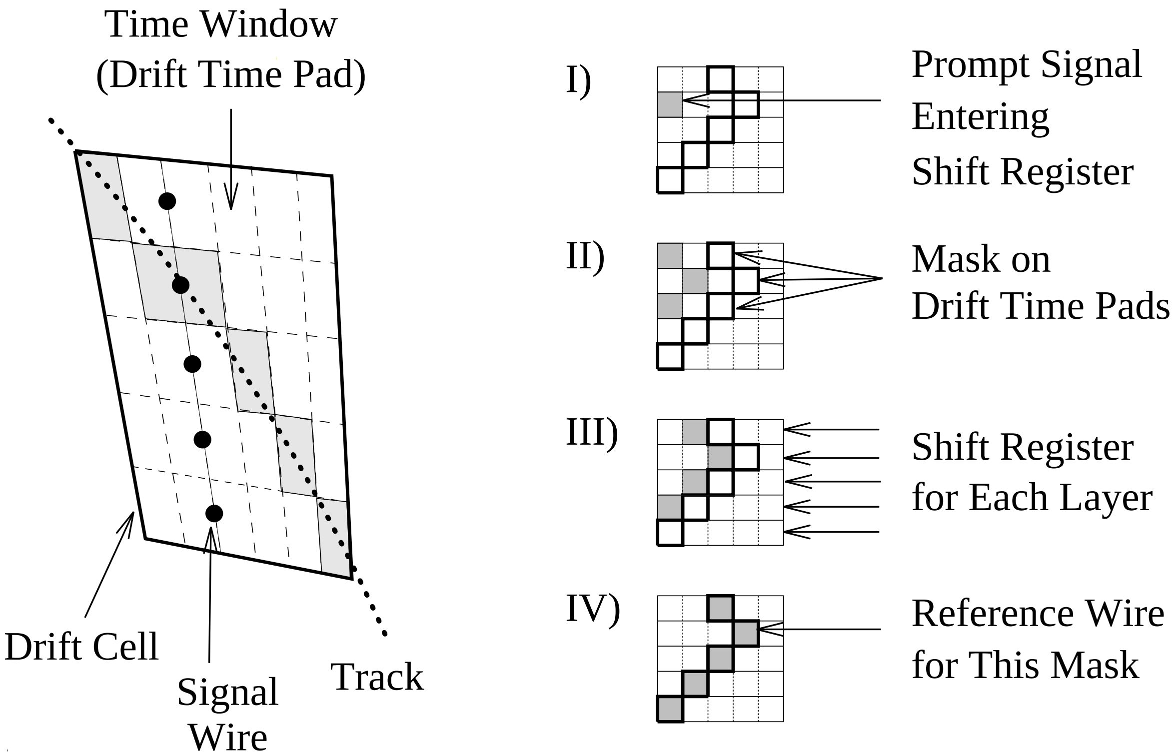

Figure 20: Concept of track finding of the drift chamber r-φ trigger. The drift times are transformed to logical coherent signals with shift registers. The small plots I) to IV) show the time evolution as it is seen from the trigger unless a matching is found in plot IV). The V-structure in the pattern allows to determine the time, as well as the earliest arriving prompt bit, which has to be clocked through according to the maximal drift time.

A total of 210 bits belonging to one bunch crossing are transferred over the passive backplane to the L1L2 card. This happens every 96 ns as long the trigger is not stopped by a L1-Keep signal for the readout. Before the readout starts, the contents of the shift registers, in total 12285 bits, are passed over the same lines to the L1L2 card. They contain the full digitized information and can be used by a planned level 2 extension of the drift chamber r-φ trigger with a better resolution. They are also used to monitor the trigger performance and verify the trigger decision.

The L1L2 card receives the 210 bits and the shift register bits from the SRL1 cards and stores them in a ring memory. At the same time the 210 bits are passed to the L2L3 card for the higher level trigger and also the trigger elements for the central level 1 trigger (CTL1) are calculated in XILINX logic cell arrays (LCA). The control unit of the whole trigger is situated on the L1L2 card. It controls the different running modes, as trigger, shift register transfer and readout mode, of the board. The multiplicity thresholds and the distribution of the trigger elements are steered over this unit by the control program.

The L2L3 card converts the 210 bits from the SRL1 cards to differential signals and passes them over 14 twisted pair cables to the PQZP bus, which collects them and distributes them to the L2 system and to the L3 processor. Because the trigger is a synchronized system, most of these boards need the HERA clock as input. Therefore this clock is distributed from a special board, called the delay card. The phases between these different clocks for the various re-synchronization steps can be steered by the control program.

A more detailed description can be found in Appendix B.

4.3 Test Procedures

Testing the drift chamber r-φ trigger electronics and ensuring its proper functionality is not a trivial task. It is not only the number of boards and signals of the trigger which cause problems, some of the signals are not even accessible because they only exist inside logic cell arrays. Sometimes it is not possible to measure all relevant signals in a conventional method with oscilloscope probes and logic analyzer, because they are covered by other essential boards.

Instead of making a major effort to try to connect all important points to measuring instruments, one can make use of the programmability of the XILINX logic cell arrays (LCA) on the SRL1 cards and the test pattern memories on the receiver cards.

The idea is to load whole roads or parts of them into the test pattern memories and record the result of the trigger decision. By comparing the expected with the measured result of many different roads it is possible to find a broken line in the logic circuit. Therefore the contents of the LCA is changed sometimes by replacing the ‘four out of five logic’ by a ‘five out of five logic’ so that every signal is needed in the logic. This can be done by exchanging the contents of the look up tables in the LCAs; the timing of the signals is not changed. At the same time, the readout program of the front end processor can be tested.

The whole test procedure is controlled by the control program running on the Macintosh IIx computer. It loads the pattern into the receiver memories and starts a test run. Each time a road is fed into the trigger logic, a receiver card generates a signal which is used as L1-Keep signal in the STC crate. So the readout is started unbiased even when the trigger has not generated a trigger output signal. This procedure is repeated 100 times for each road. Each time the 210 trigger bits for several bunch crossings are read-out. After the first cycle also the shift register bits are read-out. This is done only once to save time. After the 100^{th} cycle, the control program stops the test run and loads a new pattern. The communication between the two programs is done by the dual ported memory of a VIC in the STC crate. For the different status of the test run, bits are set in the memory and, finally the front end processor program writes the results into the memory from where the control program reads it. The road design of 1993 had 326 roads for each 30^{th} of the azimuth plane. About six hours is needed to test all 9780 roads in all φ sectors.

In the following figures the result of one such test run is shown. In Figure 21 the trigger hardware efficiencies for the standard masks and the validated t_0 masks are given as functions of the receiver card number and the mask number for 'five out of five logic'. The overall efficiency for the standard masks is 90.8 % and for the validated t_0 masks it is 90.0 %. For the 'four out of five logic', as used in 1993, the efficiencies rise to 97.1 % and 96.4 % respectively.

The inefficiencies shown as white spots in the figure originate from three different problems:

- The holes around mask numbers 95 and 115 derive from wrongly connected circuit lines to a XILINX LCA chip on the SRL1 card.
- The holes at the receiver card numbers 12, 13 and 27, 28 are due to bad connections and broken lines.
- All other holes result from timing problems (mainly too long or short propagation delays within the XILINX LCAs) which lead to loss of the information at the next synchronization step. This has been verified by changing the input timing of the information. Figure 21 shows the efficiency for the input timing with the highest efficiency.

In Figure 22 the performance of the shift register bit read-out is shown. The transfer efficiency as well as the wires with read-out problems are given as functions of the SRL1 card number and the input pin number. The input pins 41 to 48 correspond to layer 25 of the central jet chamber and are not used for the level 1 trigger; they are, therefore, not tested by the test procedure.

The overall transfer efficiency of the shift register bits is 97.7 %. The fraction of bits which never arrived is 1.4 %. The rest of 0.7 % did arrive but not in the correct time slice or the length of the bit was changed during the transmission. The noisy bits at the input pin numbers 1 to 4 are due to a timing problem during the transmission. They always occur in pairs. A correct transferred bit of them introduces another fake bit while writing into the memory on the L1L2 card due to a bad adjustment of the memory control signals.

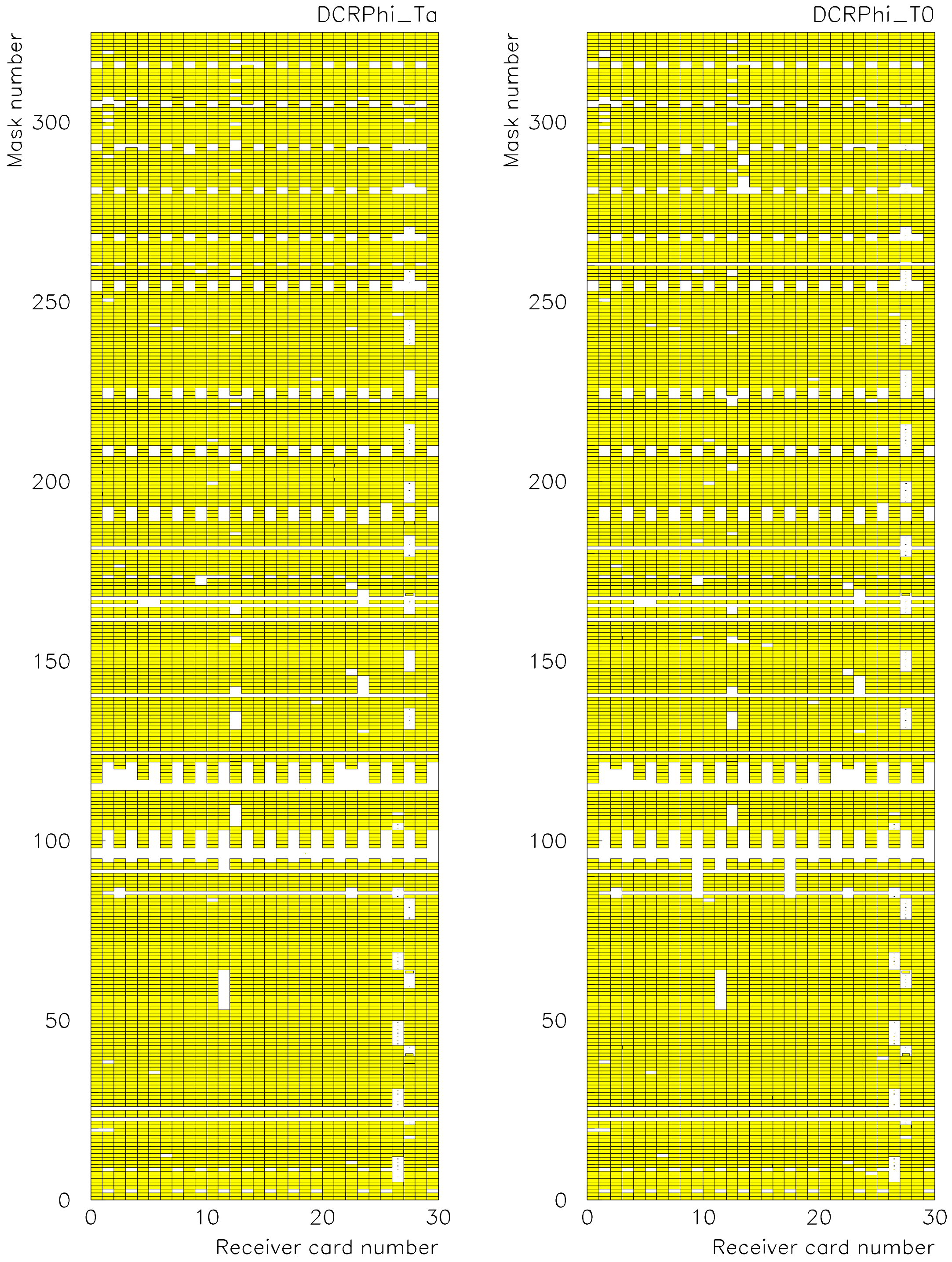

Figure 21: Hardware trigger efficiency as functions of the receiver card number and the mask number. The black spots mark a high efficiency the white spots a low efficiency. On the left the efficiency of the trigger element DCRPhi_Ta is shown. The overall efficiency is 90.8 %. On the right the efficiency of the trigger element DCRPhi_T0 is shown. The overall efficiency is 90.0 %.

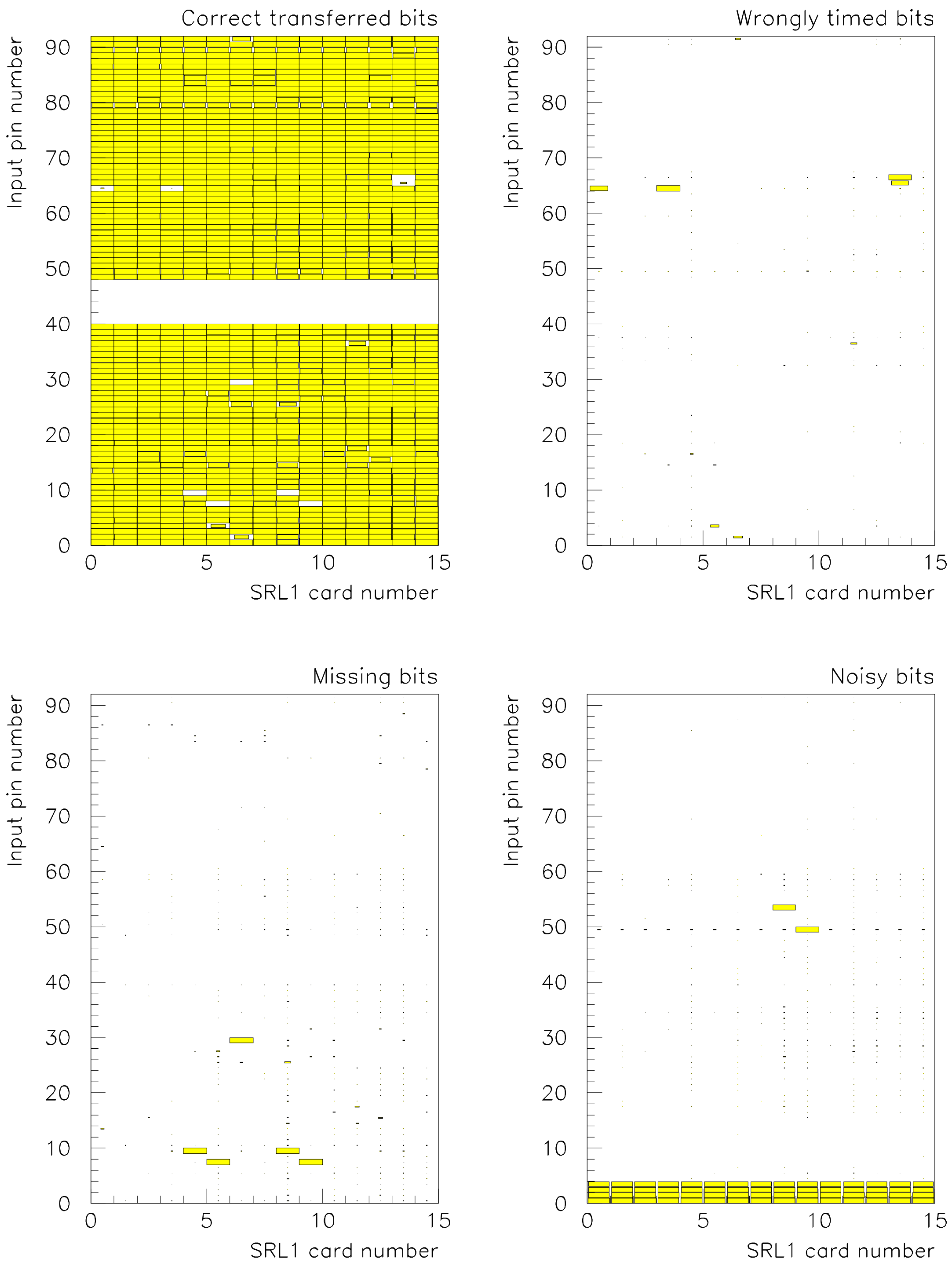

Figure 22: Shift register read-out performance as functions of the SRL1 card number and the input pin number. The black spots mark a high efficiency the white spots a low efficiency. Top left the correct transferred bits are entered. The efficiency is 97.7 %. Top right the bits are entered which came in a wrong time window. This is 0.7 % in this case. Bottom left the bits which never arrived are entered. This is 1.4 % in this case. Bottom right the noise bits, bits which were read-out but never were sent, are entered.

4.4 Performance

In this section the performance of the drift chamber r-φ trigger is described. The efficiencies in function of various physical variables are shown. In the first part, the efficiency calculation of the trigger is explained. Finally, the dependency of the efficiency of the time of synchronization in the receiver cards is shown.

4.4.1 Geometrical Acceptance

Figure 23 shows the observed geometrical resolution of the trigger. Tracks from cosmic rays measured by the central jet chambers with small distance of closest approach (DCA) and the designed transverse momentum p_t threshold of 420 MeV/c^2 are picked out from an initial flat distribution. At low transverse momentum p_t a correlation between DCA and p_t can be observed. Low momentum tracks below the threshold with a large DCA trigger as tracks with high transverse momentum and small DCA. This can be explained with wrongly measured curvature of these tracks by the trigger due to the 'four out of five logic' or accidental hits.

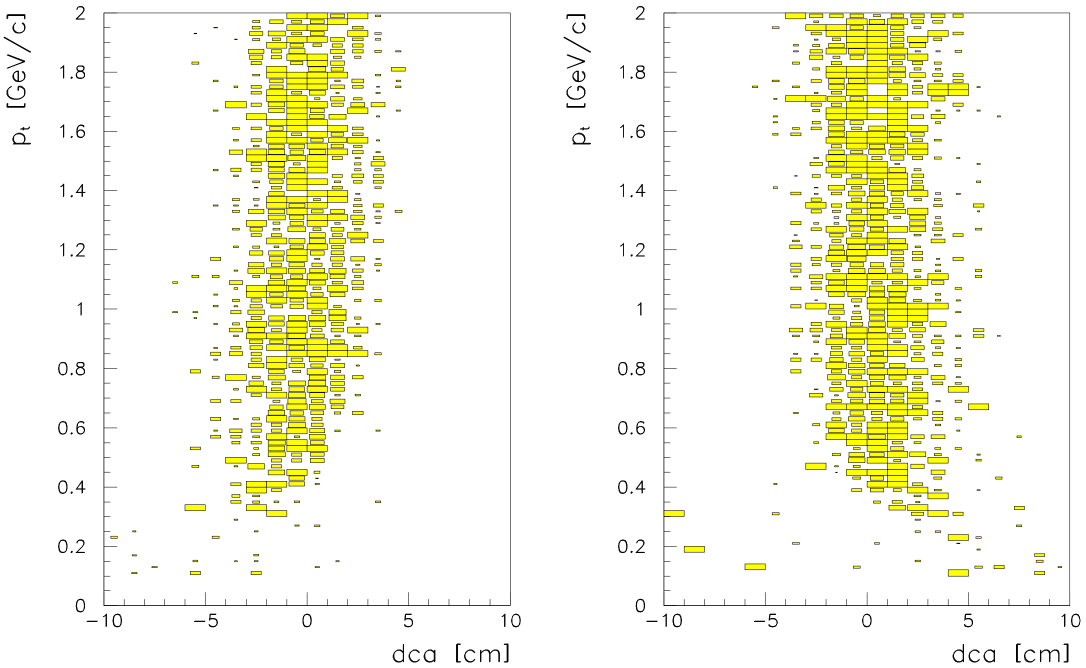

Figure 23: Acceptance of the trigger in the p_t-*dca* plane. The figure on the left side shows the acceptance for negatively charged particles. The figure on the right side shows the acceptance for positively charged particles.

4.4.2 Efficiency Calculation

Before calculating the efficiency of the trigger, the definition of what constitutes a track and how the relation between the tracks and the trigger information can be found, must be defined. To define a track a criteria which is as lose as possible is used, however, not all tracks can be used as candidates. Despite the 'four out of five criterion' it is not possible for the trigger to find a track which does not reach the outer central jet chamber. Therefore at least one hit in the inner and one hit in the outer central chamber is required for a usable track. In addition, only events are used which have at least been triggered by a subtrigger not containing any drift chamber r-φ trigger conditions. Otherwise the event sample would be biased towards an optimistic track finding efficiency.

For the offline analyses only the course information of the 210 bits, built out of the 10000 masks, is available. The granularity in φ of these 210 bits is 45 azimuth sectors. The tracks, measured by the central jet chambers, are matched in φ with this quality of the trigger bits. As the masks are focused at the reference wires, the maximum resolution for the matching is achieved for the azimuth φ of a track at a radius R of 32.5 cm. The azimuth φ at a radius R is given by

$$\varphi(R) \quad = \quad \varphi_0 \quad + \quad \arcsin \frac{\kappa \cdot R}{2} \tag{65}$$

with φ_0 the azimuth angle of the trajectory in the DCA point. It is compared with the azimuth φ of the the sector corresponding to the threshold trigger element defined as follows

$$\varphi \quad = \quad \frac{2\pi}{15} \cdot i_{\mathrm{SRL1}} \quad + \quad 0.14 \cdot i_{\mathrm{sector}} \quad . \tag{66}$$

with

$$i_{\mathrm{SRL1}} \in [\,0, 14\,] \quad \text{and} \quad i_{\mathrm{sector}} \in [\,0, 2\,] \quad .$$

Each of the 15 SRL1 cards covers an azimuth angle of $2\pi/15$ rad whereby each SRL1 card is split into three sectors shifted by an azimuth angle of 0.14 rad.

For the validated t_0 masks and therefore also for the trigger element DCRPhi_T0, the azimuth φ is given by

$$\varphi \quad = \quad \frac{2\pi}{15} \cdot i_{\mathrm{SRL1}} \quad + \quad 0.28 \tag{67}$$

with

$$i_{\mathrm{SRL1}} \in [\,0, 14\,] \quad .$$

The granularity for this information is only $2\pi/15$ rad.

A difference in azimuth φ of

$$\triangle\varphi \quad = \quad \pm 0.12 \text{ rad} \tag{68}$$

for the standard masks and

$$\triangle\varphi \quad = \quad \pm 0.24 \text{ rad} \tag{69}$$

for the validated t_0 masks is allowed to assign the track.

In Figure 24 the difference in azimuth between the reconstructed track and the nearest corresponding trigger bit is histogrammed. The peak in the histogram for the trigger element t_0 is wider because the granularity for this bit is 15 instead of 45 as for all other threshold bits.

The accidentally found tracks can be estimated by the side bins of the peak in the histogram. This is about 6 % in the case of trigger element DCRPhi_Ta.

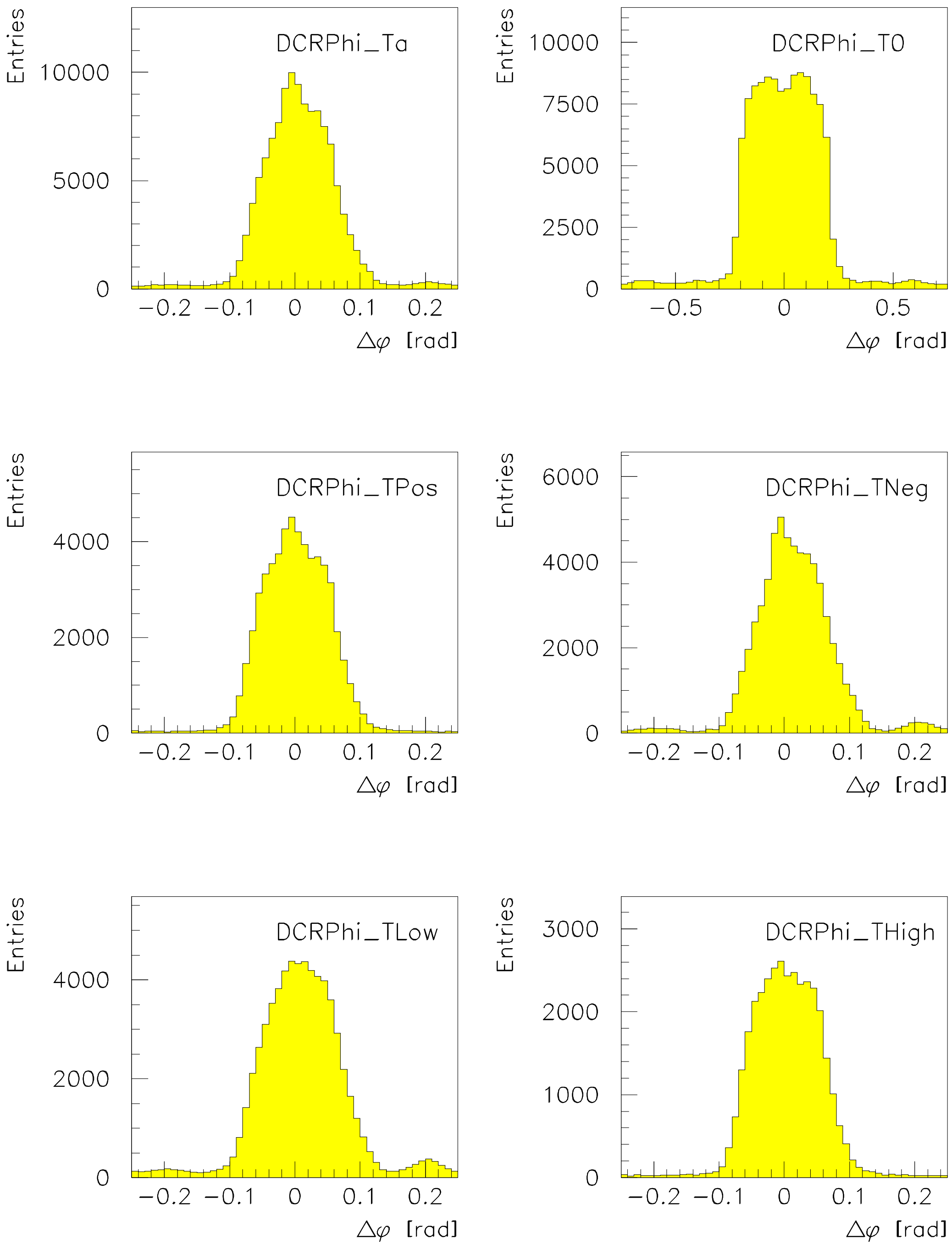

Figure 24: Difference $\triangle\varphi$ of the azimuth angles between the reconstructed track and the nearest corresponding trigger bit for the the six trigger elements DCRPhi_Ta, DCRPhi_T0, DCRPhi_TPos, DCRPhi_TNeg, DCRPhi_TLow, and DCRPhi_THigh.

4.4.3 Trigger Efficiency

Figure 25 shows the transverse momentum p_t acceptance of the tracks triggered by the drift chamber r-φ trigger. The tracks from cosmic rays are used to obtain this efficiency distribution. A cut on the absolute value of the distance of closest approach (DCA) of the tracks of 1 cm was applied to exclude the influence of the DCA threshold. Due to the low multiplicity of he cosmic ray events the assignment of the trigger information to the tracks measured by the central jet chambers is not ambiguous. The fraction of accidentally found tracks is very small. This becomes apparent in a small efficiency for triggering a track with a transverse momentum p_t below 400 MeV/c.

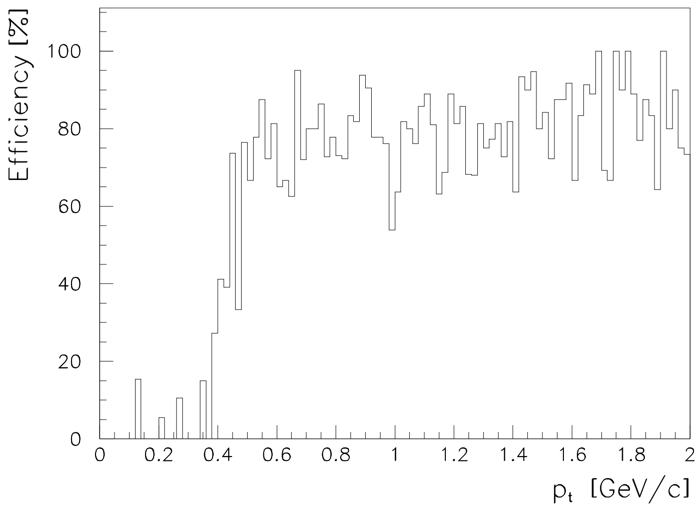

Figure 25: Trigger efficiency for cosmic ray data as a function of the transverse momentum p_t for the trigger element DCRPhi_Ta of the drift chamber r-φ trigger. A cut on the distance of closest approach of 1 cm is applied on the tracks used for this distribution.

In the following efficiency distributions for ep data the background by accidentally found tracks is not subtracted.

The transverse momentum p_t distribution of the triggered tracks from ep data is show in Figure 26 for the different threshold trigger elements. For comparison, the efficiencies for positively and negatively charged tracks are shown in the same figures. To obtain this distribution, a cut on the absolute value of the DCA of the tracks of 1 cm was applied to exclude the influence of the DCA threshold. It can be seen that the efficiency for negatively charged tracks is slightly higher than for positively charged tracks. There are also differences in the threshold behaviour. The thresholds for positively charged tracks are always some MeV/c lower than the thresholds for negatively charged tracks. The resolution of the trigger is constant in the curvature, therefore a less steep efficiency edge for the high transverse momentum trigger elements, compared to the low momentum trigger elements, is observed. The different efficiency rises of the wrong charged tracks in the figures for the trigger elements DCRPhi_TPos and DCRPhi_TNeg are because in the design, masks which corresponds to infinite momentum tracks — straight lines — are assigned to the negative track counter. In this curvature region the transverse momentum is not measured very well and leads to ambiguity.

The same behaviour is seen in the efficiency distribution as functions of the curvature κ of the tracks in Figure 27. For these distributions as well, a cut on the DCA of 1 cm was applied. In this representation the efficiency edges are similar. The different efficiencies for positively and negatively charged tracks can be seen as well. It is also clearly visible that high momentum tracks, tracks with curvature around zero, are treated as negatively charged tracks.

The DCA acceptance is important for rejecting beam wall interactions and therefore has to be smaller than the beam pipe radius. The efficiency as a function of the DCA of the tracks is shown in Figure 28. Only tracks with a transverse momentum larger than 420 MeV/c are used for these distributions. The full width at half maximum is 4 cm for the standard masks and the validated t_0 masks and this is much smaller than the radius of the beam pipe of 10 cm. The DCA acceptance for low transverse momentum tracks is the same for positively and negatively charged tracks. For high transverse momentum the acceptance is shifted for these two cases. The acceptance for the trigger element DCRPHI_T0 looks worse due to the wider azimuth angle interval $\triangle\varphi$ which assign the track to the mask. This does not influence the performance, because the trigger element DCRPhi_T0 can only occur with an other trigger element. In the figures for the trigger elements DCRPhi_TPos and DCRPhi_TNeg it can be seen that wrong charged tracks trigger most likely if they have a DCA of 3 cm to 4 cm.

In Figure 29 the trigger efficiency as a function of the azimuth φ is given. In 1994 some sectors of the central jet chambers had high voltage problems. Most of them were at the outer jet chamber. In undamaged sectors an efficiency over 80 % is achieved in the 1994 data. The sectors of the jet chambers with high voltage problems are seen most clearly in the figure of trigger element DCRPhi_THigh because these tracks are mostly straight and therefore cross only few sectors. For all other figures the effect is smeared out because the tracks cross several sectors, damaged and undamaged ones. The significant lower efficiency for the trigger element DCRPhi_TLow is due to the not box like transverse momentum acceptance between 420 MeV/c and 800 MeV/c. At 800 MeV/c the efficiency has already dropped significantly as can be seen in Figure 26.

In Figure 30, where the efficiency as a function of cosine of the polar angle ϑ is given, no dependency on this variable is seen. The drop at both ends is due to the chamber acceptance. The polar angle ϑ range in which the trigger is able to detect tracks is $27.6° \leq \vartheta \leq 151.3°$. For the trigger element DCRPhi_TLow the same reason as for the previous figure, showing the azimuth angle distribution, leads to a lower efficiency.

4.4.4 Synchronization

The efficiency of the trigger is strongly dependent on the time of synchronization in the receiver cards. To measure this effect, cosmic ray events are taken. Their event time distribution is not peaked. In the analysis of each measurement point, events within a time window of 4.8 ns are selected and the efficiency for these events calculated. The result for the standard masks and the validated t_0 masks is shown in Figure 31. It can be seen that the validated t_0 masks are much more sensitive to the synchronization

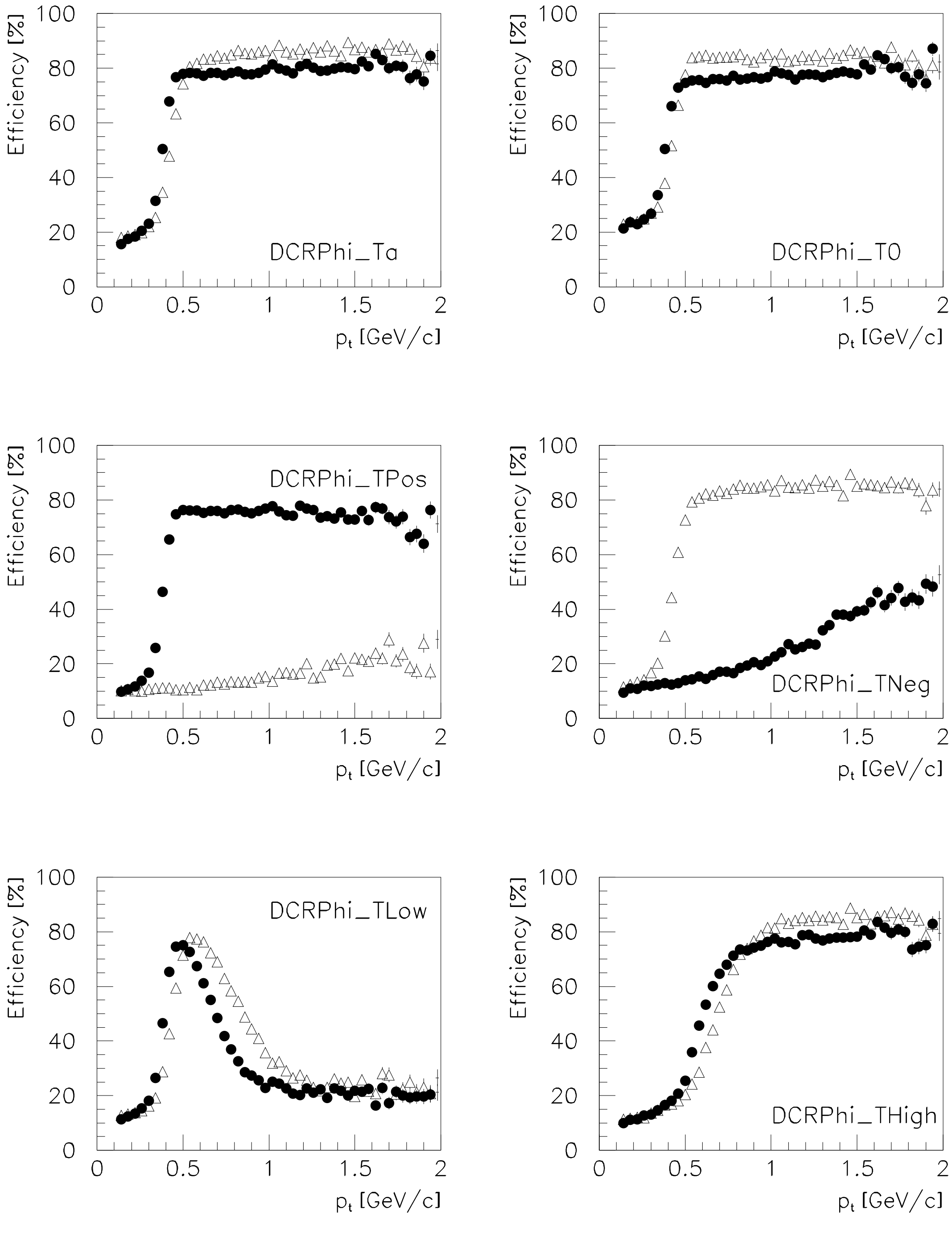

Figure 26: Trigger efficiency for data collected in 1994 as a function of the transverse momentum p_t for the the six trigger elements DCRPhi_Ta, DCRPhi_T0, DCRPhi_TPos, DCRPhi_TNeg, DCRPhi_TLow, and DCRPhi_THigh. Positively and negatively charged particles are entered separately to the figures; $\bullet$ corresponds to positively charged particles, $\triangle$ to negatively charged particles. A cut on the distance of closest approach of 1 cm is applied on the tracks used for these distributions.

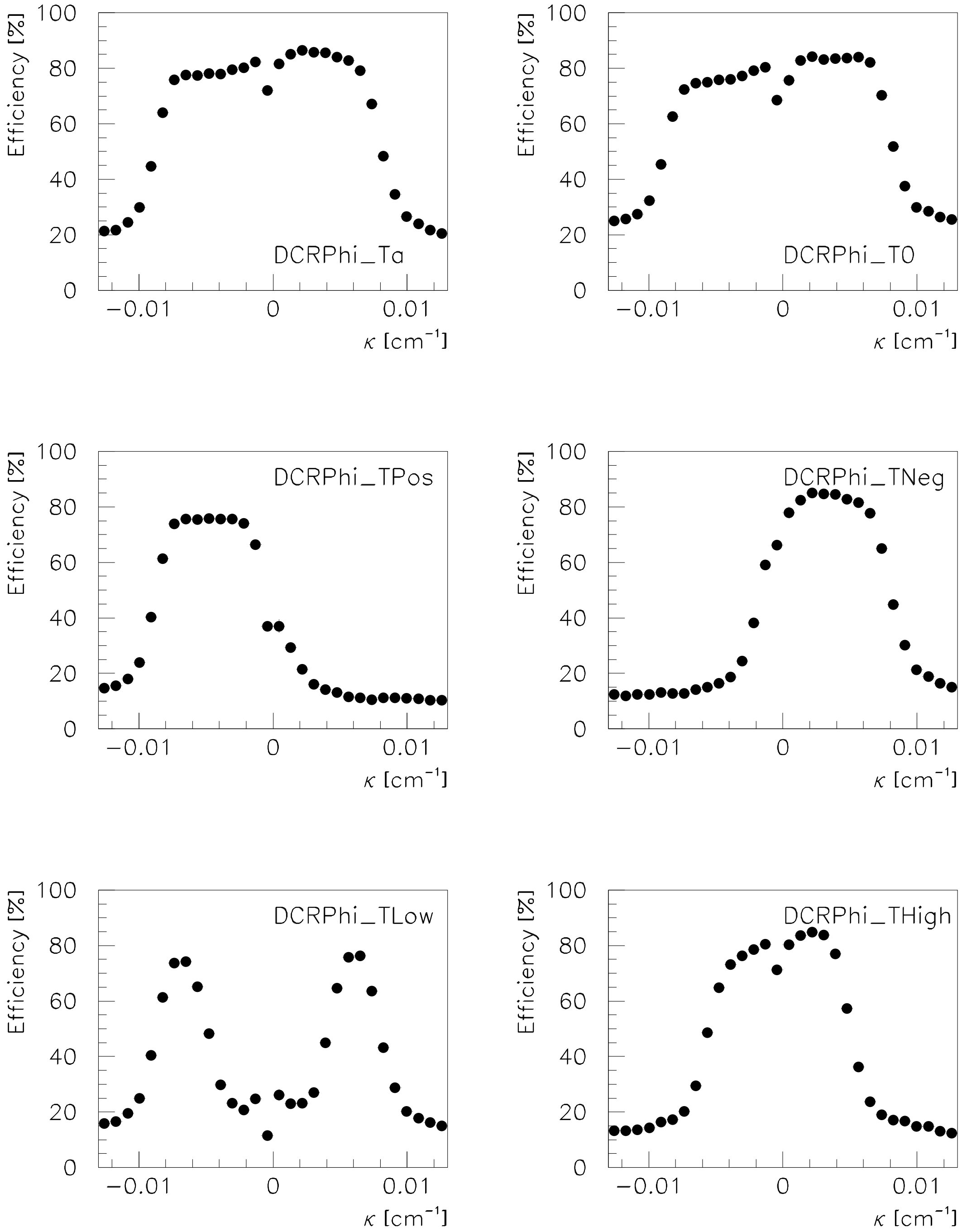

Figure 27: Trigger efficiency for data collected in 1994 as a function of the curvature κ for the the six trigger elements DCRPhi_Ta, DCRPhi_T0, DCRPhi_TPos, DCRPhi_TNeg, DCRPhi_TLow, and DCRPhi_THigh. A cut on the distance of closest approach of 1 cm is applied on the tracks used for these distributions.

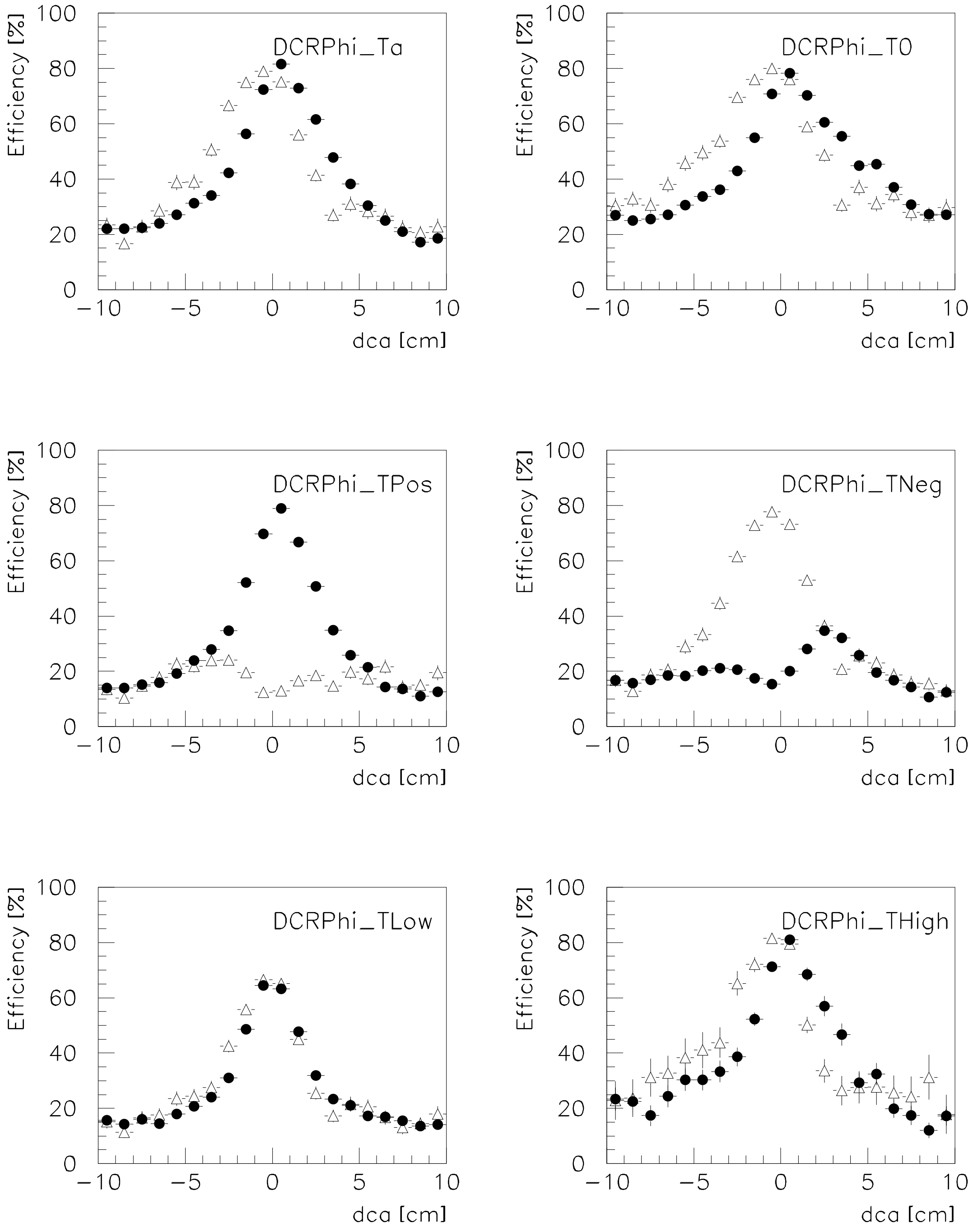

Figure 28: Trigger efficiency for data collected in 1994 as a function of the distance of closest approach *dca* for the the six trigger elements DCRPhi_Ta, DCRPhi_T0, DCRPhi_TPos, DCRPhi_TNeg, DCRPhi_TLow, and DCRPhi_THigh. Positively and negatively charged particles are entered separately to the figures; $\bullet$ corresponds to positively charged particles, $\triangle$ to negatively charged particles. A cut on the transverse momentum of 420 MeV/c is applied on the tracks used for these distributions.

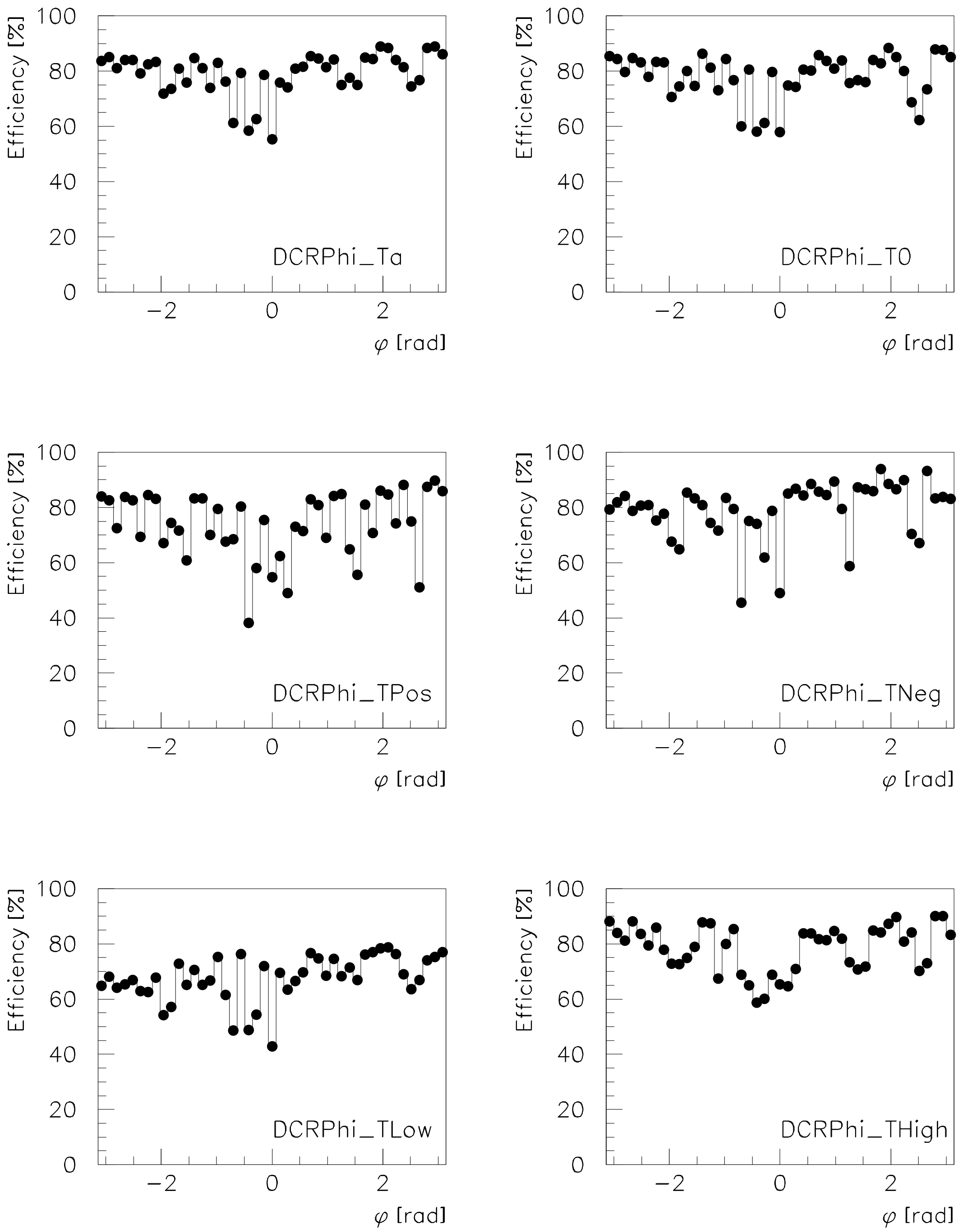

Figure 29: Trigger efficiency for data collected in 1994 as a function of the azimuth angle φ for the the six trigger elements DCRPhi_Ta, DCRPhi_T0, DCRPhi_TPos, DCRPhi_TNeg, DCRPhi_TLow, and DCRPhi_THigh. A cut on the transverse momentum of 420 MeV/c and the distance of closest approach of 2 cm is applied on the tracks used for these distributions.

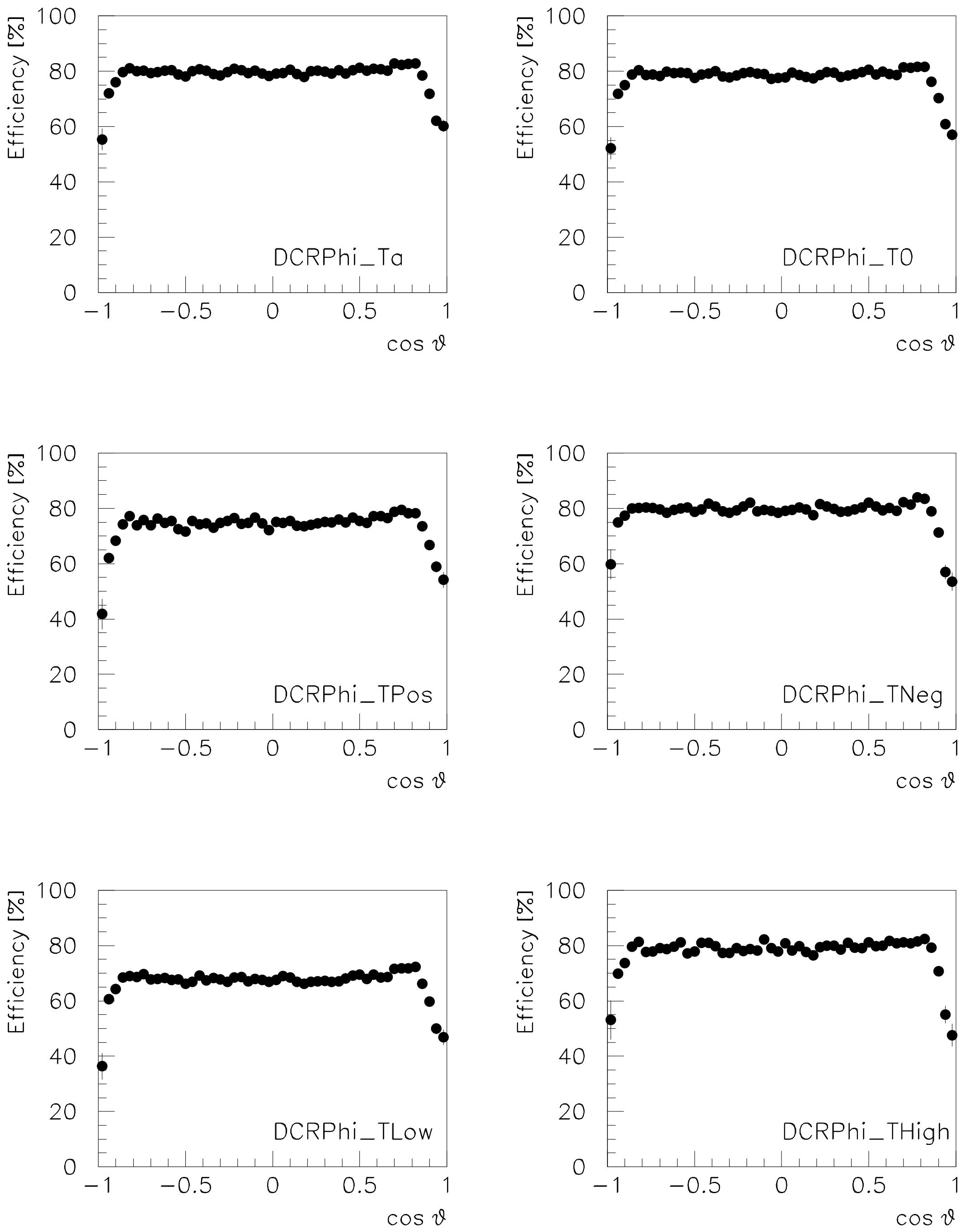

Figure 30: Trigger efficiency for data collected in 1994 as a function of the cosine of the polar angle ϑ for the the six trigger elements DCRPhi_Ta, DCRPhi_T0, DCRPhi_TPos, DCRPhi_TNeg, DCRPhi_TLow, and DCRPhi_THigh. A cut on the transverse momentum of 420 MeV/c and the distance of closest approach of 2 cm is applied on the tracks used for these distributions.

than the standard masks. The width of the distribution of validated t_0 masks is much smaller than for the standard masks because of the requirement of an additional drift pad, the prompt bit, for the validated t_0 masks. For these masks the fraction of too early triggering masks is much smaller due to the required prompt bit which has a drift time smaller than 50 ns. Therefore the distribution is not symmetric. The long tails in the distribution at later triggers are due to accidental pad combinations which look like tracks. For an ideal trigger this does not influence the performance because the real track has already triggered at an earlier time and the pipelines have already stopped.

The distribution is not symmetric for the validated t_0 masks in contrast to the standard masks. This can be explained by the loss of the prompt bit if the synchronization is too late. Because this bit is always required for the validated t_0 masks, the influence is much bigger than for the standard masks.

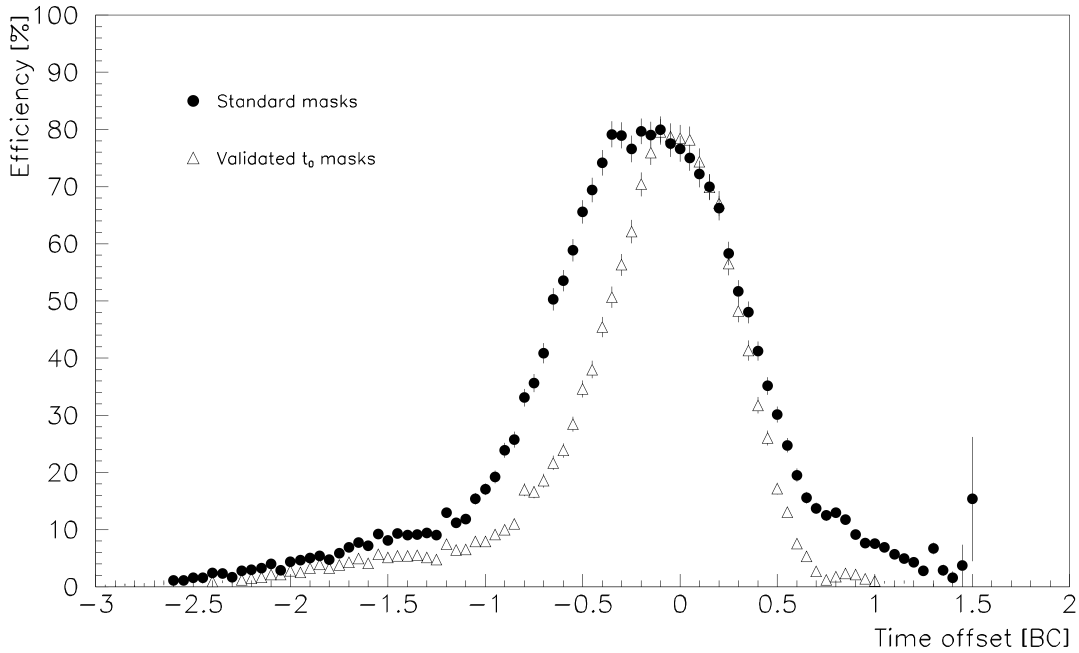

Figure 31: Trigger efficiency for the standard masks and the validated t_0 masks as a function of the time of synchronization in the receiver cards. The efficiencies are calculated from cosmic ray events taken in 1994. Higher bunch crossing (BC) values correspond to an earlier time, lower bunch crossing values to a later time.

4.4.5 Wrongly Timed Triggers

The trigger element DCRPhi_T0 assigns the event to the correct bunch crossing. The first bunch crossing, in which the element occurs, is the correct one, because it consists of the drift pad of the reference wire which has a drift time shorter than 50 ns.

The performance of the trigger element DCRPhi_T0 is identical to the performance of the validated t_0 masks shown in Figure 31. Because the prompt bit is required, the trigger element cannot come too early for an ideal trigger. Nevertheless the efficiency for the validated t_0 masks is not zero for a bunch crossing earlier as can be seen in

Figure 31. This can be explained by jitter and walk of the discriminators and different propagation delays of the cables. This leads to a small probability that a drift pad moves into an earlier bit at the synchronization and causes an early trigger.

This probability is listed in Table 13 for 1993 and 1994 data.

transverse momentum interval	too early t_0 triggers 1993 data	1994 data
positively charged low momentum tracks	0.37 ± 0.27 %	1.67 ± 0.24 %
positively charged high momentum tracks	0.96 ± 0.47 %	0.59 ± 0.12 %
negatively charged low momentum tracks	0.63 ± 0.63 %	0.51 ± 0.11 %
negatively charged high momentum tracks	0.41 ± 0.27 %	0.28 ± 0.07 %

Table 13: Probability of too early triggers for 1993 and 1994 data for the validated t_0 masks separated for the four transverse momentum intervals.

4.4.6 Double Counting

The trigger road generation procedure was chosen to have a good separation power between the different momentum intervals. Therefore the roads overlap each other. The resulting double counting is discussed in this section. The probability that one track match to more than one road rises as more the roads overlap, especially because, with the 'four out of five logic', not all ten hits are required. There are also noise hits in the system because the thresholds of the discriminators are rather low to achieve a high efficiency.

In Table 14 the measured probability, that one track measured by the central jet chamber leads to more than one fired mask, is listed for 1993 and 1994 data.

transverse momentum interval	counting factor 1993 data	1994 data
positively charged low momentum tracks	1.62 ± 0.11	1.32 ± 0.04
positively charged high momentum tracks	1.84 ± 0.28	1.24 ± 0.05
negatively charged low momentum tracks	1.64 ± 0.09	1.18 ± 0.03
negatively charged high momentum tracks	1.77 ± 0.23	1.20 ± 0.05

Table 14: Probability of double counting for 1993 and 1994 data separated for the four transverse momentum intervals. The given numbers are the mean values of fired masks for one measured track by the central jet chambers.

5 Monte Carlo Programs

5.1 Event Generator

To generate events with heavy quarks several Monte Carlo generators are used. The generator has to describe the following parts of a scattering

- hard process and structure function,
- initial and final state radiation,
- beam remnants,
- fragmentation,
- decays.

The production of heavy quarks in ep scattering is described by the QCD process of BGF. In the fragmentation of all partons involved in the subprocess the radiation of gluons is included. To ensure that the center of mass energy of the subprocess does not drop below the threshold for the production of heavy quarks ($\sqrt{\hat{s}} \geq 2m_q c^2$) due to radiation, the fragmentation is calculated backwards. The calculation is started at the fragmentation products and is counted back to the starting point of the fragmentation by adding radiation. The fragmentation which produces the heavy quarks is done according to the string model.

For the radiation of the photon from the electron the program IJRAY 1.5 [70] is used. It calculates the energy and momentum of the scattered electron and the photon and passes this values to the program PYTHIA 5.6 [71] which calculates the γp scattering. The fragmentation is done by the Lund string model which is implemented in the program JETSET 7.3 [72].

It is possible to describe the following structures of the photon which interacts with the proton in the photoproduction process with the program PYTHIA 5.6

- direct component,
- resolved component, VDM and anomalous,
- resolved component, VDM only,
- resolved component, anomalous only.

The ratio between these processes has to be provided by the user.

In addition it is also possible to choose in the program PYTHIA 5.6 the proton and the photon structure functions. For the proton the structure function GRV LO[21] [73] and, for the photon, the structure function GRV-G LO[22] [74] were chosen.

For this analysis two sets of event type were generated.

[21] Proton structure function: Glück-Reya-Vogt — leading order

[22] Photon structure function: Glück-Reya-Vogt — leading order

- 7959 photoproduction events with the direct component of the photon. Each of them contains at least one nonresonant decay $D^{*\pm} \longrightarrow D^0\pi^\pm \longrightarrow K_S^0\pi^+\pi^-\pi^\pm$ with all tracks within the acceptance of the central tracker.

- 8125 photoproduction events with the resolved component of the photon. Each of them contains at least one nonresonant decay $D^{*\pm} \longrightarrow D^0\pi^\pm \longrightarrow K_S^0\pi^+\pi^-\pi^\pm$ with all tracks within the acceptance of the central tracker.

In the generation step of these events several decay channels were excluded. The $D^{*\pm}$ mesons had to decay in a D^0 meson and a positive or negative pion respectively. The D^0 meson was forced to decay into a K^0 meson with two oppositely charged pions. The K^0 meson had to decay as a K_S^0 meson.

All acceptances and efficiencies are calculated separately. At the end a mixing ratio of 75 % direct component and 25 % resolved component has been chosen to determine the overall acceptance and efficiency. The resolved component consists of the VDM component and the anomalous component. The mixing ratio is derived from comparison of the predicted cross section for the different components of the photon gluon fusion. In Section 8.4 it is shown that the result is only weakly depending on the choice of these ratios.

5.2 Trigger Simulation

One part of the detector simulation is the simulation of the drift chamber r-φ trigger. This is done in several steps analogous to the hardware. The module calculates the output of the trigger, the 210 bits which are provided from the SRL1 cards as well as all trigger elements which are sent to the central level 1 trigger. As input of the module the simulated pulses of the central jet chambers are used. The main steps of the module are listed below:

- Mask generation:
  The masks are generated in the simulation in exactly the same way as for the hardware trigger. This is described in Section 4.1. The parameters of Table 11 as well as the geometry of the inner and outer jet chamber are needed to generate a set of masks. This step is carried out once only in a simulation job.

- Discrimination:
  In the first step the discriminators are simulated. The digital signals are received from the chamber pulses by applying thresholds on the pulses, and efficiencies and time resolutions on the discriminators.

- Synchronization:
  The digital signals derived from describing the discriminators are transformed into a bit pattern as in the synchronization.

- Road finding:
  The generated masks are compared with the bit pattern which derives from the simulated event. All found roads are passed to the next step.

- Trigger output:
  The found roads are combined with the trigger output. First the 14 bits, provided by each of the 15 SRL1 cards as described in Section 4.2 and Appendix B.3, are calculated. From these 210 bits the output data, which are sent to the central data acquisition, as well as all possible trigger elements, which are sent to the central level 1 trigger, are formed. All output data are stored in the same format as is used for real events.

The agreement between the *ep* data and simulated data is shown in the Figures 32, 33, 34 and 35. The data from the run period of 1993 are compared with the Monte Carlo simulated data. The same distributions are shown as in Section 4.4, where the performance of the drift chamber r-φ trigger is discussed. The selection of figures is restricted to the later used trigger elements DCRPhi_Ta, DCRPhi_T0, DCRPhi_TNeg and DCRPhi_THigh.

The overall efficiency during the run period of 1993 is lower than for 1994. The main reason is the damaged sectors of the central jet chambers. Broken wires lead to missing signals and serious high voltage problems in some sectors. The influence of these sectors can be seen in the distributions where the efficiency is given as a function of the azimuth angle φ. The efficiency holes are clearly visible. These dead wires and almost dead sectors lead to difficulties in simulating the trigger. The distributions of the efficiency as a function of the azimuth angle φ show the biggest discrepancies between *ep* data and Monte Carlo simulated data. Outside the acceptance area the efficiencies are higher for the *ep* data than for the simulated data. This introduces also less steep edges of the efficiencies at the boarder of the acceptance area in the transverse momentum distributions and the curvature distribution respectively as well as in the DCA acceptance distribution. All other distribution agree rather well, even the different acceptance for positively and negatively charged tracks is simulated well.

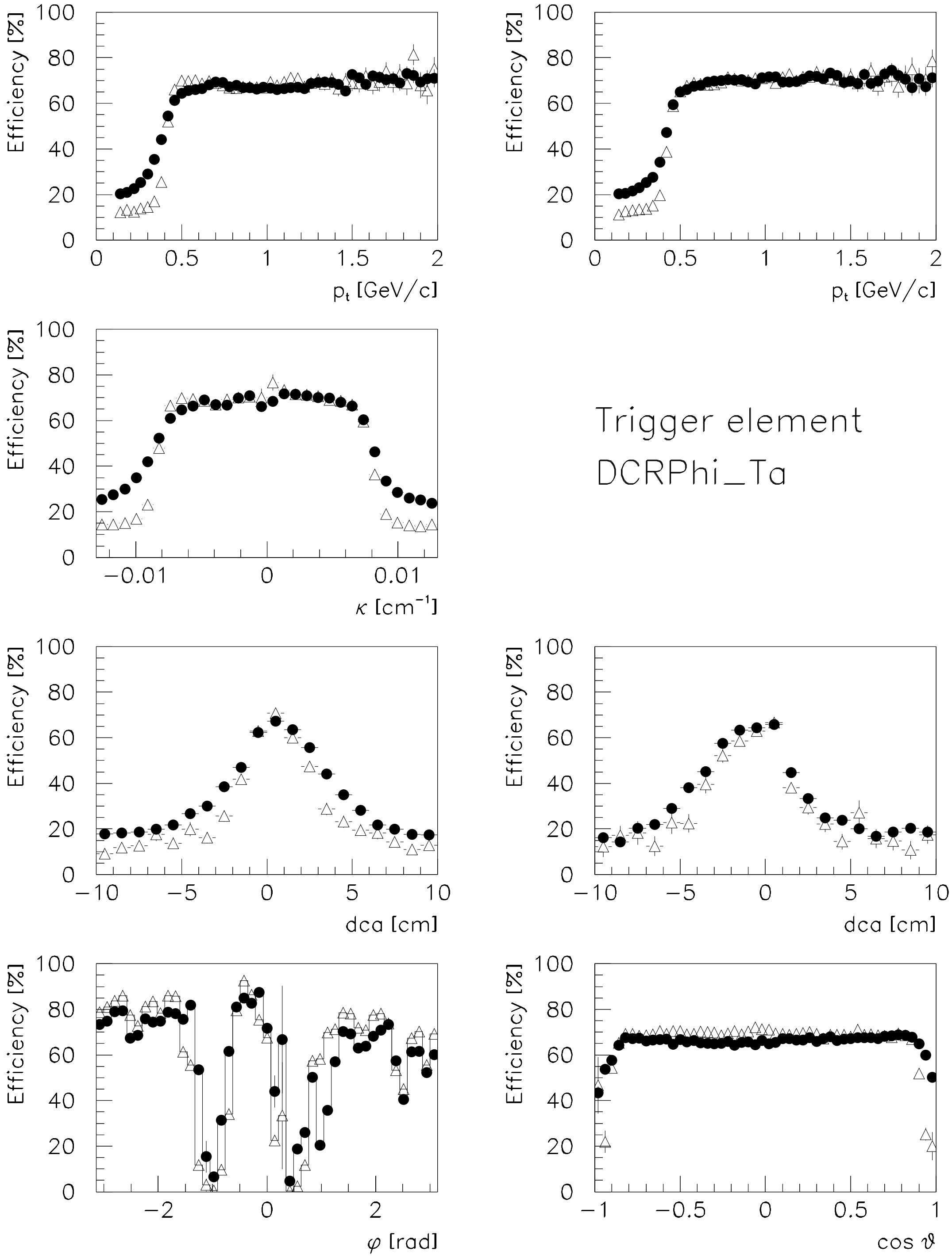

Figure 32: The trigger efficiency of the trigger element DCRPhi_Ta for ep data and Monte Carlo simulated data for the run period of 1993; $\bullet$ corresponds to ep data, $\triangle$ to Monte Carlo simulated data. The efficiency is given as a function of the transverse momentum p_t, the curvature κ, the distance of closest approach dca, the azimuth angle φ and the cosine of the polar angle ϑ. For the transverse momentum p_t and the distance of closest approach dca the distributions are separated for positively and negatively charged tracks. The distribution for positively charged tracks are on the left, for negatively charged tracks on the right. The same cuts on the tracks are applied as in the Figures 26, 27, 28, 29 and 30.

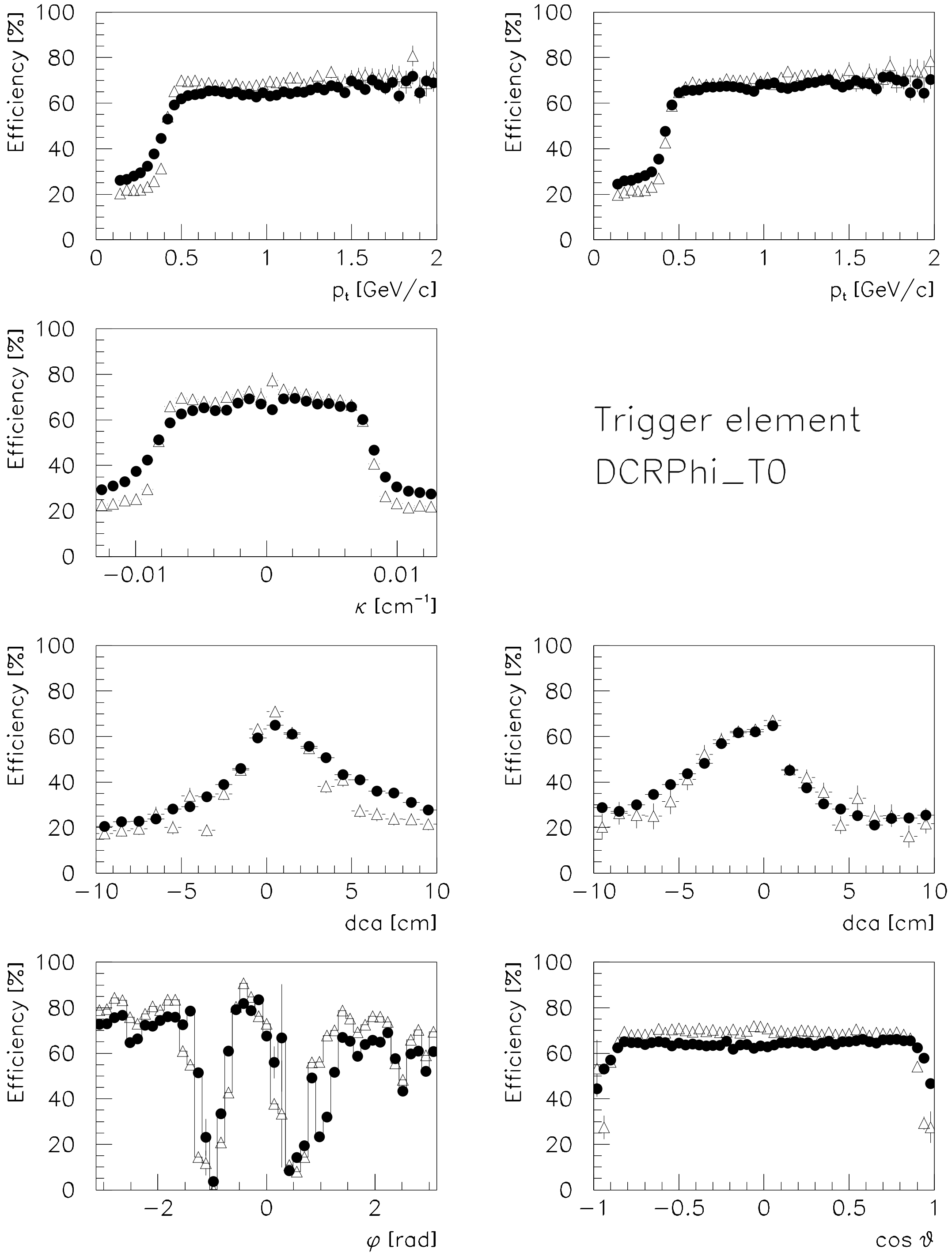

Figure 33: The trigger efficiency of the trigger element DCRPhi_T0 for ep data and Monte Carlo simulated data for the run period of 1993; • corresponds to ep data, △ to Monte Carlo simulated data. The efficiency is given as a function of the transverse momentum p_t, the curvature κ, the distance of closest approach dca, the azimuth angle φ and the cosine of the polar angle ϑ. For the transverse momentum p_t and the distance of closest approach dca the distributions are separated for positively and negatively charged tracks. The distribution for positively charged tracks are on the left, for negatively charged tracks on the right. The same cuts on the tracks are applied as in the Figures 26, 27, 28, 29 and 30.

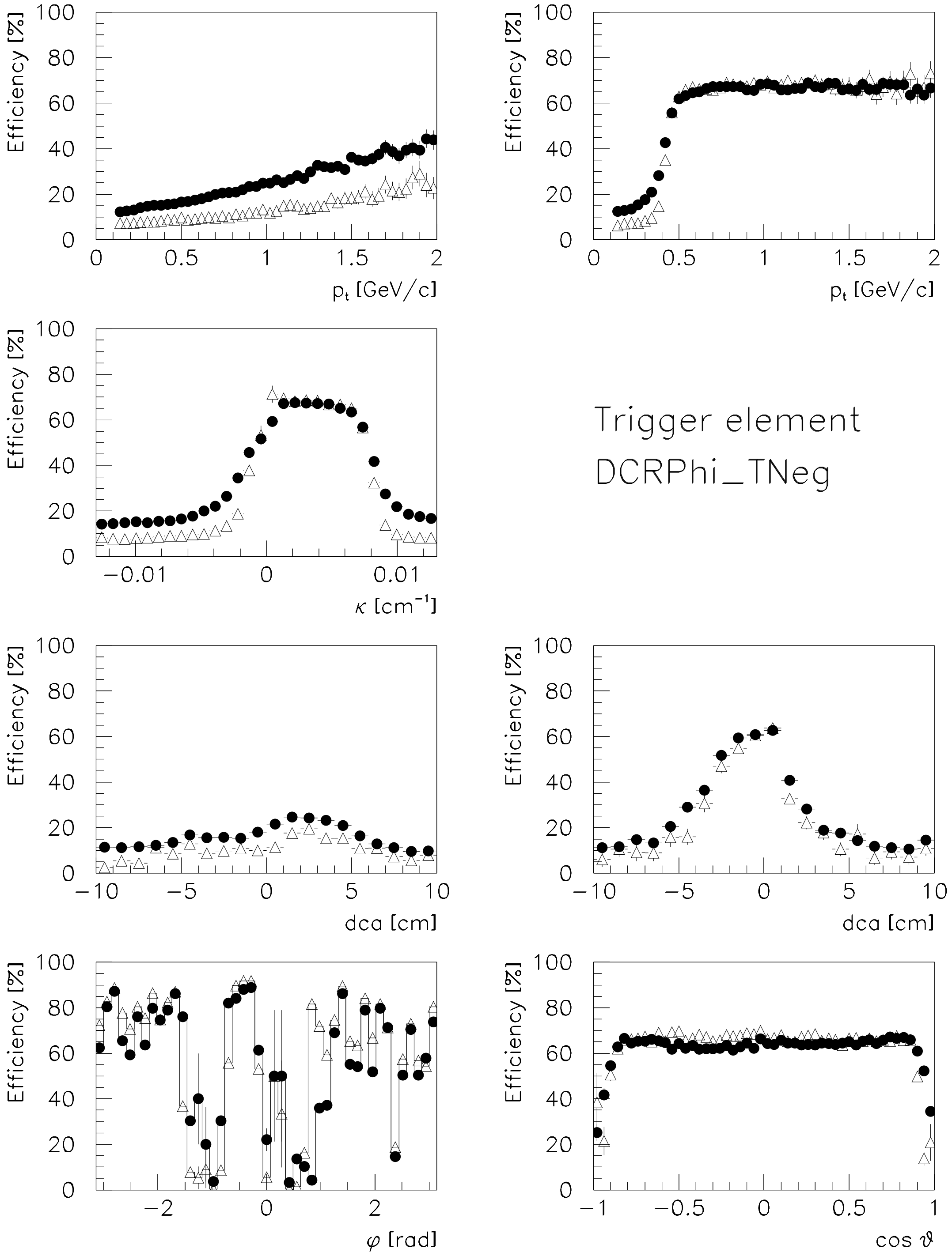

Figure 34: The trigger efficiency of the trigger element DCRPhi_TNeg for ep data and Monte Carlo simulated data for the run period of 1993; • corresponds to ep data, △ to Monte Carlo simulated data. The efficiency is given as a function of the transverse momentum p_t, the curvature κ, the distance of closest approach dca, the azimuth angle φ and the cosine of the polar angle ϑ. For the transverse momentum p_t and the distance of closest approach dca the distributions are separated for positively and negatively charged tracks. The distribution for positively charged tracks are on the left, for negatively charged tracks on the right. The same cuts on the tracks are applied as in the Figures 26, 27, 28, 29 and 30.

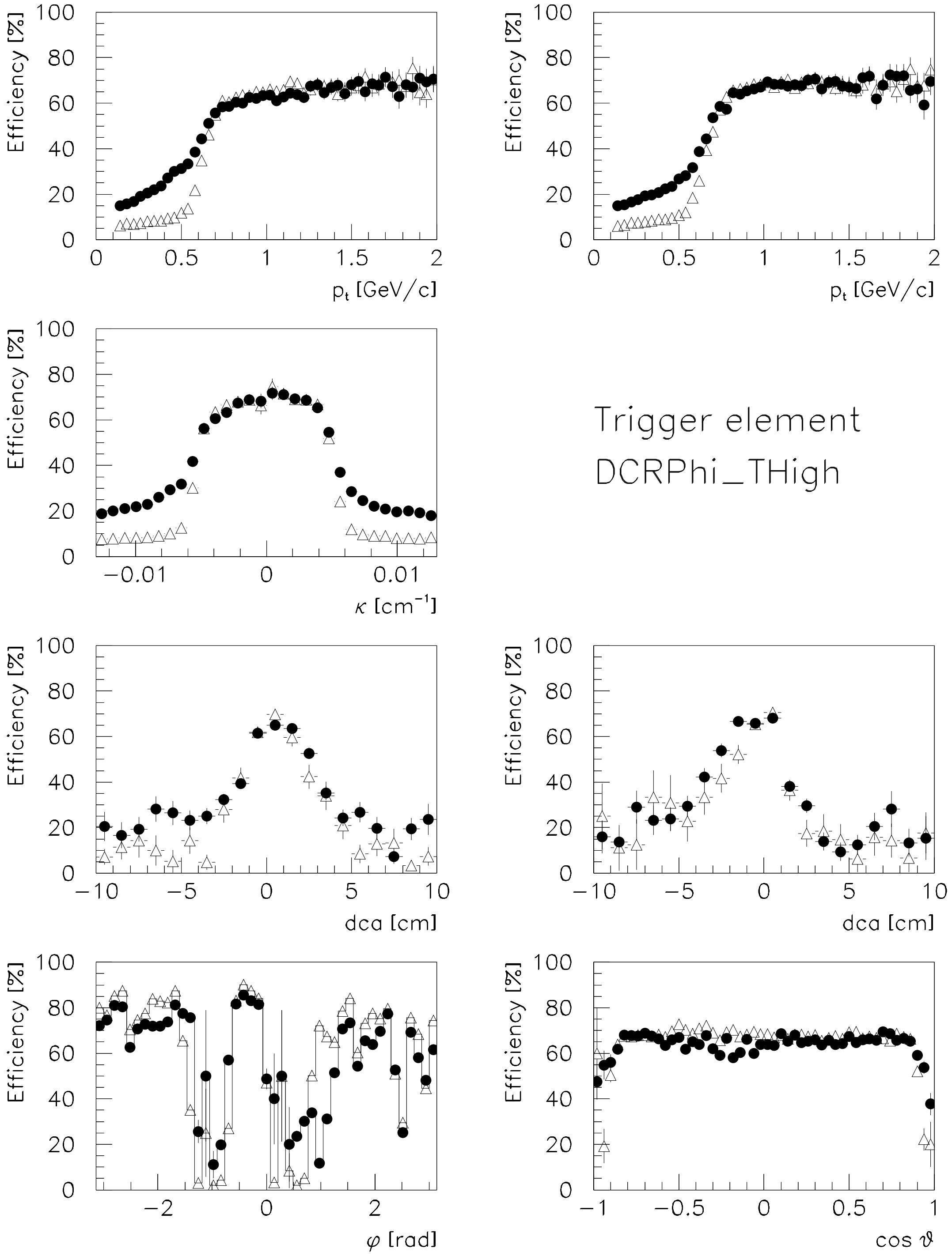

Figure 35: The trigger efficiency of the trigger element DCRPhi_THigh for ep data and Monte Carlo simulated data for the run period of 1993; $\bullet$ corresponds to ep data, $\triangle$ to Monte Carlo simulated data. The efficiency is given as a function of the transverse momentum p_t, the curvature κ, the distance of closest approach dca, the azimuth angle φ and the cosine of the polar angle ϑ. For the transverse momentum p_t and the distance of closest approach dca the distributions are separated for positively and negatively charged tracks. The distribution for positively charged tracks are on the left, for negatively charged tracks on the right. The same cuts on the tracks are applied as in the Figures 26, 27, 28, 29 and 30.

6 The Selection Criteria

The mechanism of the charm production is already described in Section 1.4. The charm quarks are produced mainly by photon gluon fusion with their typical kinematical properties. These charm events have the characteristic of low energy deposition in the central part of the detector. The main background is photoproduction events of light quarks and protons colliding with residual gas in the beam pipe.

Because of the low energy deposition in the calorimeter, the charm events have to be selected by criteria derived from tracks. Therefore a stable track criteria is needed. In this section the track criteria is defined and the event selection, based on these selected tracks, is introduced.

6.1 Track Selection

The magnetic induction in the central jet chamber is to first order homogeneous. It points in the forward direction, in the direction of the outgoing proton. Charged particles describe helices which point in the z direction. The radius of the helix in the magnetic induction B is given for a particle with mass m and charge ze by the cyclotron radius

$$r = \frac{\gamma m}{zeB} v_t \qquad \text{with} \qquad \gamma = \frac{1}{\sqrt{1-\frac{v^2}{c^2}}} \quad , \tag{70}$$

where v_t is the component of velocity of the particle in the direction perpendicular to the magnetic field. The transverse momentum of a particle can be calculated from the known magnetic induction B and the curvature of the track

$$p_t = \gamma m v_t = ze \cdot B \cdot r \quad . \tag{71}$$

Knowing the slope of the helix, defined below, the total momentum of the particle can also be calculated.

The parameterization of a helix needs five parameters. The following parameters are chosen in the H1 experiment [75]:

$\kappa \in \mathbb{R}$: Curvature, the inverse radius of the track in the $r\varphi$-plane together with its sign $\kappa = \pm 1/r$. A positive sign of κ means a counter-clockwise rotation of the particle trajectory in the x-y plane as viewed from the $+z$ direction. These definitions are shown in Figure 36. Because the magnetic induction points in the positive z direction, tracks of particles with positive charge have a curvature with a negative sign.

$dca \in \mathbb{R}$: Distance of closest approach (DCA) of the track to the z axis with corresponding sign. The sign is equal to that of the vector product $\vec{dca} \times \vec{p_t}$ with $\vec{dca}$ being the vector from the origin of the coordinate system to DCA. These definitions are shown in Figure 36.

$\varphi \in [-\pi, +\pi]$: Azimuth at the DCA, the angle between the transverse momentum $\vec{p_t}$ at the DCA and the x axis.

$\vartheta \in [0, +\pi]$: Slope of the helix, defined by $\vartheta = \arccos(\mathrm{d}z/\mathrm{d}s)$, where s is the length along the helix measured in the direction of flight. It is also the polar angle of the momentum; for the proton direction of flight is $\vartheta = 0$.

$z \in \mathbb{R}$: z coordinate at the DCA point.

The sign of curvature κ and dca is defined such that there is no discontinuity in the parameters by changing one of the parameters.

With the angles defined above the momentum components of a particle are given in terms of the transverse momentum as

$$\begin{array}{lclcl} p_x & = & p \cdot \sin\vartheta \cdot \cos\varphi & = & p_t \cdot \cos\varphi \\ p_y & = & p \cdot \sin\vartheta \cdot \sin\varphi & = & p_t \cdot \sin\varphi \\ p_z & = & p \cdot \cos\vartheta & & . \end{array} \qquad (72)$$

Instead of the polar angle ϑ often the pseudo rapidity η is used. The rapidity y of a particle, which is Lorentz invariant, in contrast to the polar angle ϑ, is connected with its velocity v by

$$\beta \;=\; \tanh y \qquad \text{with} \qquad \beta \;=\; \frac{v}{c} \quad . \qquad (73)$$

This is the well known angle argument of the Lorentz transformation into the rest frame of the particle. In scattering experiments the rapidity defined by the velocity component parallel to the beam axis is given by

$$y \;=\; \frac{1}{2} \cdot \ln \frac{E + p_z}{E - p_z} \quad . \qquad (74)$$

Because differences and differentials of rapidities are Lorentz invariant it is a frequently used quantity. If the particle mass is neglected the rapidity y becomes the pseudo rapidity η which is defined as a simple function of the polar angle

$$\eta \;=\; -\ln\left(\tan\left(\frac{\vartheta}{2}\right)\right) \quad . \qquad (75)$$

For the events used in this analysis only tracks which fulfill the following criteria are taken:

$|z| < 100$ cm: The track should come from the interaction region.

$|z - z_{\mathrm{v}}| < 25$ cm: The origin of the track should be near to the primary vertex. z_{v} is the z coordinate of the reconstructed primary vertex of the event.

$|\eta| < 1.5$: The track should lie in the angle acceptance of the central jet chamber. This criterion corresponds to a cut on the polar angle ϑ of $25° < \vartheta < 155°$.

$R_{\mathrm{start}} < 40$ cm: The track should start within a radius of 40 cm, except the track starts in a damaged sector of the inner central jet chamber. The damaged sectors are located in the following azimuth angle φ ranges

$$\begin{array}{rcccr} -1.55 & < & \varphi & < & -0.60 \\ -0.30 & < & \varphi & < & 1.25 \quad . \end{array} \qquad (76)$$

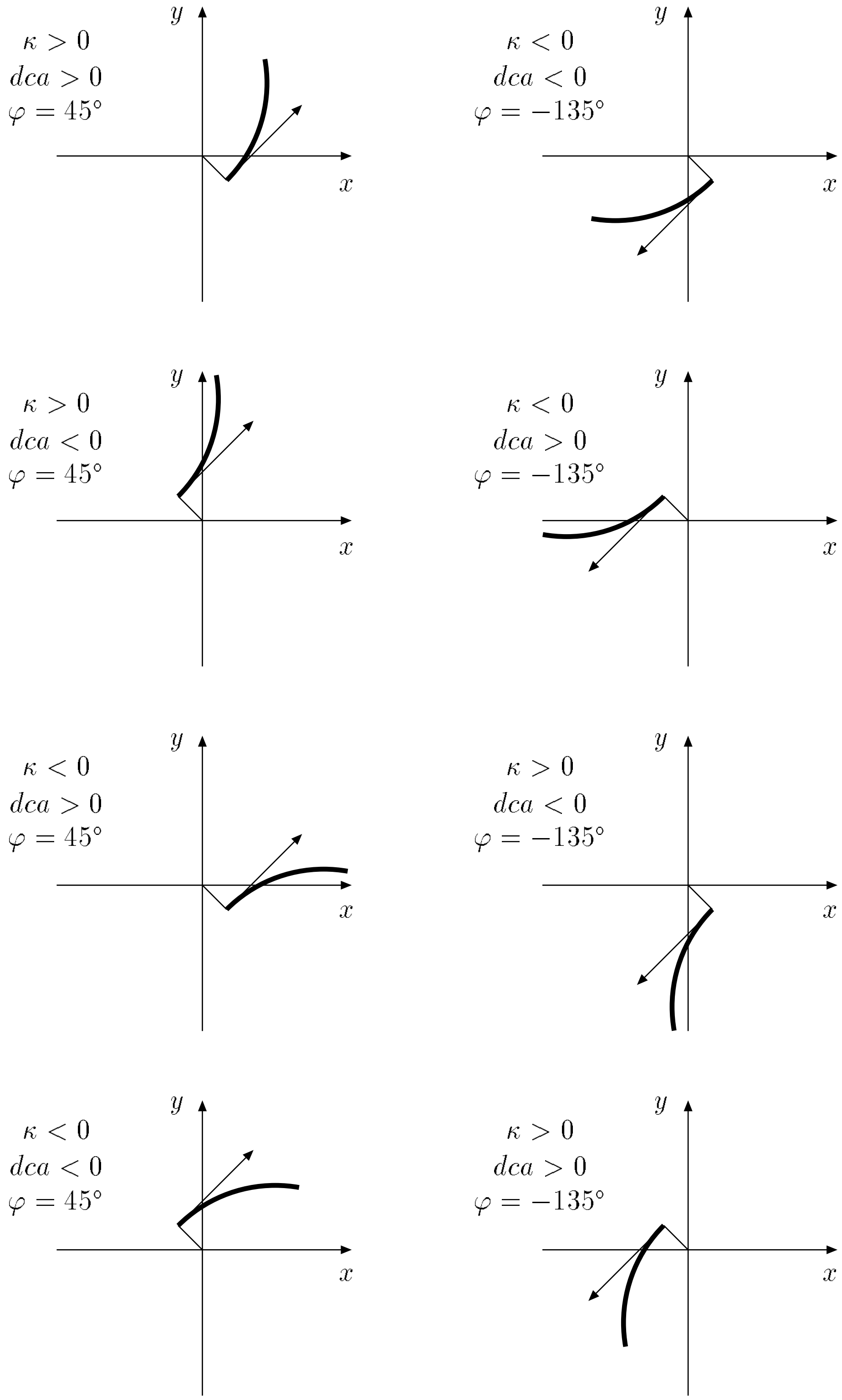

Figure 36: Definition of the conventions used for the parameters κ and dca in the equations. The different cases of projecting a track helix into the x-y plane illustrate the sign of κ and dca.

$l_{r\varphi} > 15$ cm: The minimum track length in the $r\varphi$-projection.

$p_t > 100$ MeV$/c$: To avoid wrongly reconstructed tracks a minimum radius of the curvature of a track is required.

The track criteria are very loose and reduce the data sample only slightly.

To calculate the momentum of a particle, equations (70) and (72) are used. The magnetic induction B provided by the coil is almost constant over the length of the central jet chamber. The inhomogeneities have to be taken into account when the momentum of the particle is determined. The magnetic induction B has been measured over the whole volume within the solenoid for a nominal current of the coil. These values are stored in the data base. For each detected event the current provided to the coil is measured. The magnetic induction B in a space point within the coil is derived by scaling the value from the data base with the measured current of the coil.

The small inhomogeneities of the magnetic induction is corrected in the following way: The z component of the magnetic induction B is determined at the start, in the middle, and at the end of each track. With this values an average magnetic induction $\overline{B}$ is calculated with

$$\overline{B} = \frac{1}{4}\left(B_{\text{start}} + 2B_{\text{middle}} + B_{\text{end}}\right) \quad . \tag{77}$$

For each track the average magnetic induction is inserted in equation (70). Because the assumption of circular tracks in the $r\varphi$-projection is not absolutely true, the measurement of the angle between two tracks is also subject to an error which influence the measurement of the invariant mass. This measurement error is not corrected in this analysis.

The energy loss of the pions crossing the beam pipe and the innermost chambers CIP and CIZ is also not considered in this analysis. The change of the energy is about one to two percent for pions in the energy region of 150 MeV.

6.2 Event Selection

To remove much of the background, all events written on tape are examined for typical background signatures. The events fulfilling one of the following criteria are rejected.

- No track from the interaction region (proton beamwall interaction).
- More than three tracks coming from more than 100 cm away of the nominal interaction point (proton gas interaction).
- Two collinear tracks (cosmic rays).
- Vertex at the beam pipe position in the x-y plane (proton beamwall interaction).

These criteria are used to separate background reactions from ep reactions. Because not all ep reactions have a charmed particle with a searched decay channel the event sample has to be reduced furthermore. The identification of charm decays is based in this analysis on the reconstruction the decays of $D^0 \longrightarrow K^0_S\pi^+\pi^-$ and $K^0_S \longrightarrow \pi^+\pi^-$.

If the mesons decay into two oppositely charged particles they leave a V-formed decay pattern due to the magnetic field. These patterns are called V^0 candidates. The most important candidates apart from the $K_S^0 \longrightarrow \pi^+\pi^-$ decay are the decays $\rho^0 \longrightarrow \pi^+\pi^-$, $\Lambda \longrightarrow p\pi^-$, and $\gamma \longrightarrow e^+e^-$.

The V^0 candidates examined in each event using the following criteria:

- A minimum quality criteria for the tracks.

  $|z| < 100$ cm: The track should come from the interaction region.

  $N_{\text{hit}} \geq 10$: The track should consists of at least 10 hits.

  $R_{\text{start}} < 40$ cm: The track should start within a radius of 40 cm.

  $p_t > 200$ MeV$/c$: To avoid wrongly reconstructed tracks and to reduce the number of V^0 candidates a minimum radius of the curvature of a track is required.

- Successful vertex fit (convergence of the fit algorithm).

- Invariant mass cut. The invariant mass has to lie in the following mass regions:

  $$\begin{array}{l} 398\ \text{MeV}/c^2 \text{ to } 598\ \text{MeV}/c^2 \text{ for the } K^0 \text{ hypothesis,} \\ 916\ \text{MeV}/c^2 \text{ to } 1316\ \text{MeV}/c^2 \text{ for the } \Lambda \text{ hypothesis,} \end{array}$$

  but not in the region

  $$0\ \text{MeV}/c^2 \text{ to } 50\ \text{MeV}/c^2 \text{ for the } \gamma \text{ hypothesis.}$$

- A minimum decay time of the V^0 candidate calculated by the ratio of the vertex separation d and the momentum p of the decaying particle. A value of

  $$\frac{d}{p} > 1 \tag{78}$$

  is requested. This corresponds to a decay length of about $c\tau > 0.5$ cm of the K^0 meson. This cut removes most of the V^0 candidates which derive from ρ^0 decays.

7 The Reconstruction of the Decay Chain

The decay of the $D^{*\pm}$ mesons and its decay products are already described in Section 1.5. In this section the method used to reconstruct the D^0 meson and the $D^{*\pm}$ meson from the trajectories of their decay products is described. The number of found $D^{*\pm}$ decays is given by subtracting the background candidates from the candidates in the $D^{*\pm}$ meson signal.

7.1 The Method of the Invariant Mass

The four momentum of a decaying particle can be calculated from the four momenta of its decay products. For a decay $A \longrightarrow 1, \ldots, n$ the four momentum is

$$p_A = \sum_{i=1}^{n} p_i \quad . \tag{79}$$

The variable p_A^2/c^2 is Lorentz-invariant and is equal to the mass of the decaying particle. This mass can be calculated from the four momenta of the decay products

$$m_A = \sqrt{\left(\sum_{i=1}^{n} E_i\right)^2 - \left(\sum_{i=1}^{n} \vec{p_i}\right)^2} =: m_{\mathrm{inv}}(1, \ldots, n) \quad . \tag{80}$$

It is called the invariant mass of the particles $1, \ldots, n$ independent of the existence of an original particle A.

With this method the invariant mass m_{inv} of all possible combination of tracks are added into a histogram. Most of the combinations are not obtained using tracks from the same particle. The values of the invariant mass m_{inv} are spread statistically over the whole allowed kinematical range. The combinations of tracks belonging to the searched particle decay will have an entry in the histogram near the mass of the original decaying particle. If the number of reconstructed decays is large enough a peak at the mass of the original particle will appear.

The calculated invariant mass of the real decay is Lorentz-distributed, if the original particle appears as a sharp resonance (natural width caused by the Uncertainty Principle), or Gaussian distributed, if the width of the signal is due to measurement errors.

By eliminating track combinations, which, with a high probability, do not represent the searched particle decay, the ratio between signal and combinatorial background can be improved. Obviously, criteria which include in any way the invariant mass are not allowed for reconstructing the original particle because this would bias the invariant mass distribution.

The method of the invariant mass is most effective for two body decays. The more particles are involved the higher is the combinatorial background.

7.2 The Reconstruction of the K_S^0 Meson

The K_S^0 mesons are identified by their decay into two charged pions by the method of the invariant mass. For each pair of oppositely charged tracks, a vertex fit algorithm is applied to reconstruct a vertex. The algorithm is based on the method of Kalman-filters and is described in [75]. If the vertex fit algorithm converges, the invariant mass of the two tracks is calculated according to equation (80) with the hypothesis that the two particles are pions, in the calculation of the particle's energy the mass of the charged pions is inserted (mass hypothesis).

$$E_i = \sqrt{p_i^2 + m_{\pi+}^2} \quad \text{with} \quad m_{\pi+} = 139.570 \text{ MeV}/c^2 \quad . \tag{81}$$

No particle identification, such as dE/dx measurements in the central jet chamber, is used to find the K_S^0 meson candidates.

The Figure 37 shows the distribution of the invariant mass. Near the K^0 mass a small peak above the background is visible.

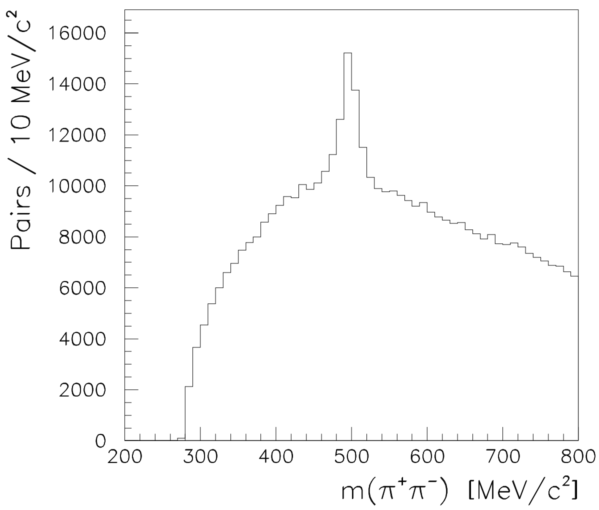

Figure 37: Distribution of the invariant mass $m_{\text{inv}}(\pi^+\pi^-)$ of the whole data sample after the event selection. The two small steps in the distribution at 400 MeV/c^2 and 600 MeV/c^2 are due to cuts in the event selection.

To improve the ratio between signal and background some kinematical criteria on tracks are introduced. In particular it is expected that the decay vertex of each K_S^0 meson (secondary vertex) is separated from the primary vertex. With a mean life time of 89 ps, the K_S^0 mesons have a decay length of several centimeters at the expected energy of the order of 1 GeV. Even although the K_S^0 mesons mostly decay within the beam pipe, the vertex of each decay is rather well known due to the vertex fit algorithm.

The following criteria are used to reduce the background combinations:

- **Vertex separation:** Only track pairs are used, where the primary and the secondary vertices are well separated. The calculated vertex separation d should be larger than its error σ_d
$$d > \sigma_d \quad . \tag{82}$$
- **DCA of the pion tracks:** Pions with a momentum in transverse direction are produced at some distance of the beam axis. The projection of the track helix in

the $r\varphi$ plane does not point back to the z axis. The searched pion tracks have a larger dca value than tracks from the primary vertex. With the requirement of a minimum DCA value wrong track combinations can be suppressed. To take into account the often rather large uncertainties in the measurement of the DCA of a track, the dca values are weighted with the corresponding error σ_{dca} and we require

$$\frac{|dca|}{\sigma_{dca}} \quad > \quad 5 \tag{83}$$

for the tracks of both pions. The $|dca|/\sigma_{dca}$ distribution is shown in Figure 38.

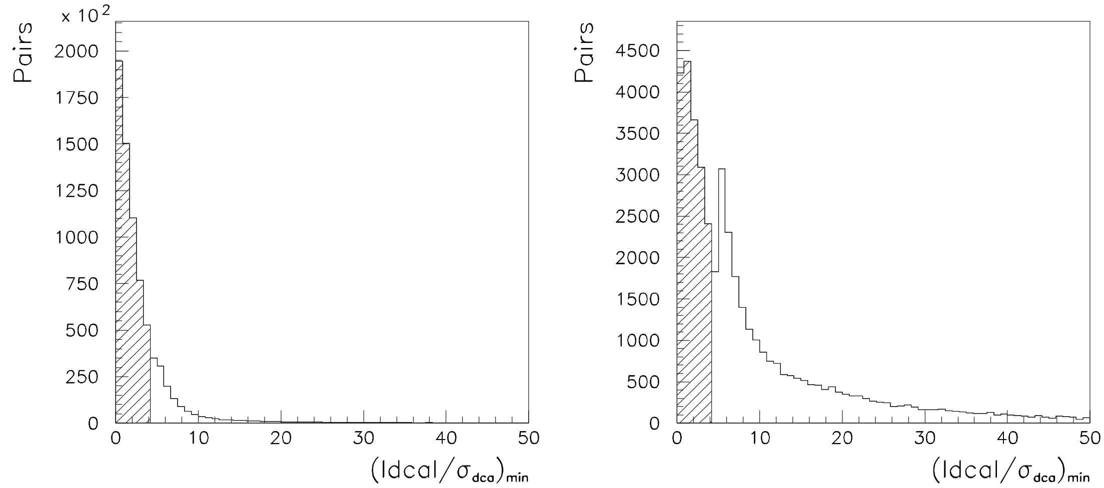

Figure 38: Distribution of the quantity $|dca|/\sigma_{dca}$. On the left the distribution of all track pairs is shown. On the right the same distribution after all other cuts, used to get the K_S^0 signal, is shown. The double peak structure is introduced by the cut on the direction of the K_S^0 momentum (85). The cut $|dca|/\sigma_{dca} > 5$ is indicated by the dashed area.

- **Angular momentum with respect to the beam axis of the pions:** From the definition of the sign of the DCA it follows that the sign of the DCA is equal to that of the z component of the angular momentum. Because a K_S^0 meson has no angular momentum corresponding to the z axis the angular momentum of the two pions have to cancel each other (angular momentum conservation)

$$dca_1 \cdot dca_2 \quad < \quad 0 \quad . \tag{84}$$

  This criterion is almost always satisfied for tracks satisfying (83).

- **Direction of the K_S^0 momentum:** The vector sum of the momenta of the pions at the secondary vertex is equal to the kaon momentum $\vec{p}$. The angle α between the momentum $\vec{p}$ of the kaon and the straight line through the two vertices is very small because the vertex separation of the D^0 meson decay is small. It is smaller than the resolution of the vertex measurement because no silicon tracker detector is used. Only for decays near the primary vertex the angle α can be large due to measurement errors, but this is excluded by the cut (83). Therefore the criterion

$$\cos\alpha \quad > \quad 0.9 \tag{85}$$

is required for all K_S^0 candidates. The $\cos\alpha$ distribution is shown in Figure 39.

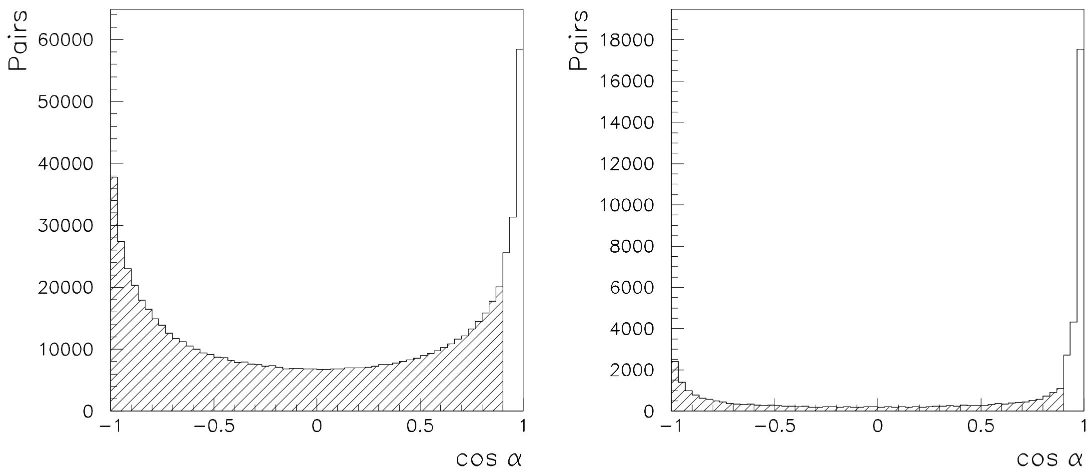

Figure 39: Distribution of the quantity $\cos\alpha$. On the left the distribution of all track pairs is shown. On the right the same distribution after all other cuts, used to get the K_S^0 signal, is shown. The cut $\cos\alpha > 0.9$ is indicated by the dashed area.

- **Decay angle in the rest frame:** Because the K_S^0 meson has no spin no direction is preferred in the rest frame and the decay is isotropic. The angle ν_π^* is defined as the angle between the direction of flight of the K_S^0 meson and one of the charged pions measured in the rest frame of the K_S^0 meson. In this analysis the positively charged pion is used. $\cos\nu_\pi^*$ is for real K_S^0 decays evenly distributed due to the isotropy of the decay. Randomly combined track pairs show particularly for high momentum a correlation with the direction of flight. This can be seen in Figure 40, where the maximum of the distribution is near $\cos\nu_\pi^* = \pm 1$ for invariant masses larger than 1 GeV/c^2. The required criteria is therefore

$$|\cos\nu_\pi^*| \quad < \quad 0.9 \quad . \tag{86}$$

  This cut improves the ratio between signal and background.

- **Quality of the vertex fit:** The vertex fit algorithm calculates for each fit the statistical quantity χ^2, an often used quantity for the quality of a fit. For a good fit hypothesis the integrated probability

$$P_\chi\left(\chi^2,\nu\right) \quad = \quad \int_{\chi^2}^{\infty} P_x\left(x^2,\nu\right)\,\mathrm{d}x^2 \quad = \quad \int_{\chi^2}^{\infty} \frac{\left(x^2\right)^{\frac{1}{2}(\nu-2)}\, e^{-\frac{x^2}{2}}}{2^{\frac{\nu}{2}}\,\Gamma\left(\frac{\nu}{2}\right)}\,\mathrm{d}x^2 \tag{87}$$

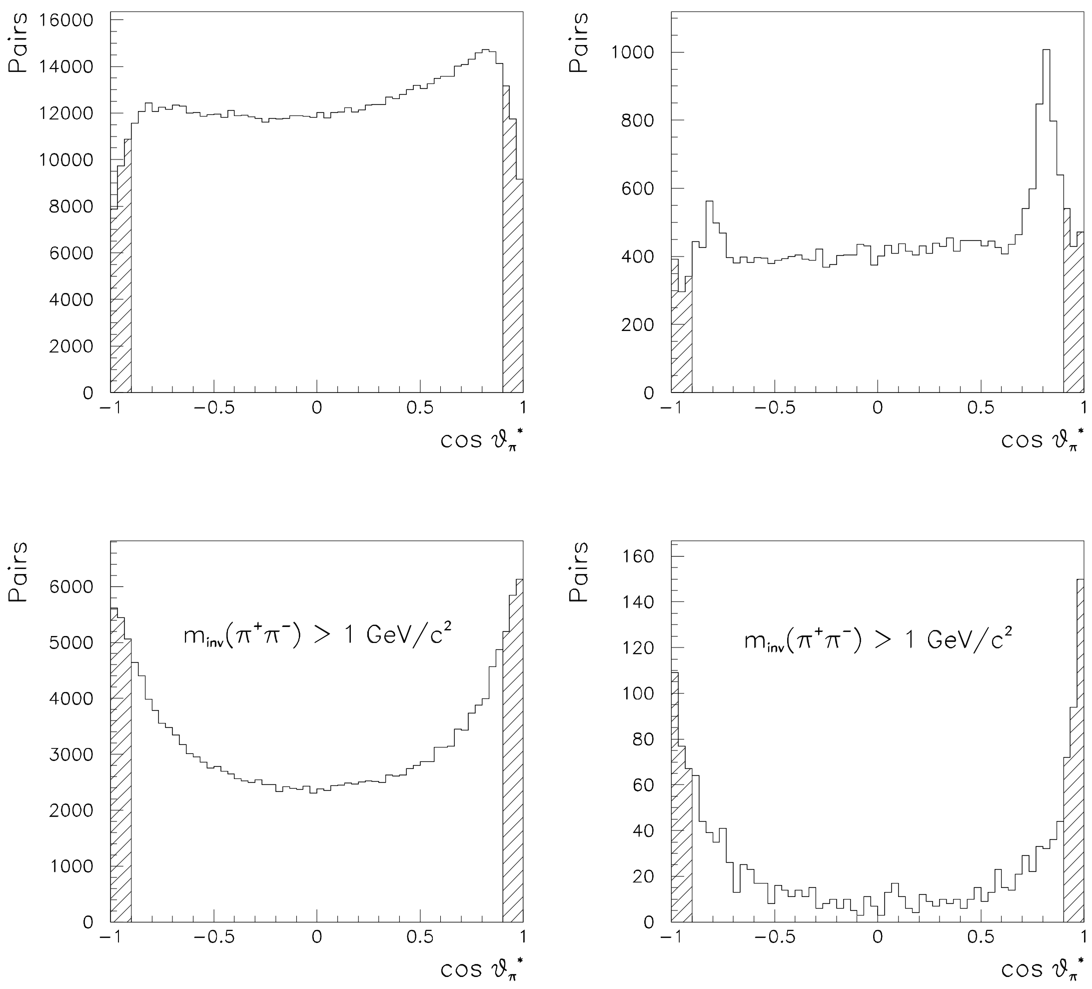

Figure 40: Distribution of the quantity $\cos\nu_\pi^*$. On the top left the distribution of all track pairs is shown. On the top right the same distribution after all other cuts, used to get the K_S^0 signal, is shown. On the bottom left and right the same distributions as on the top are shown with an additional cut on $m_{\text{inv}}(\pi^+\pi^-) > 1$ GeV$/c^2$. The cut $|\cos\nu_\pi^*| < 0.9$ is indicated by the dashed area.

is evenly distributed between 0 and 1, if the fitted quantity has Gaussian distributed errors and a linear model is applied. The variable ν is the number of degrees of freedom which is in this case $\nu = 1$. For track pairs which do not have a common vertex the hypothesis is unsuitable, which can be seen in an integrated probability $P_\chi(\chi^2)$ near zero. Therefore the distribution of $P_\chi(\chi^2)$ for all K_S^0 candidates has a pronounced peak at zero as can be seen in Figure 41. Only track pairs with a vertex with an integrated probability

$$P_\chi\left(\chi^2\right) \quad > \quad 0.01 \tag{88}$$

are taken into consideration.

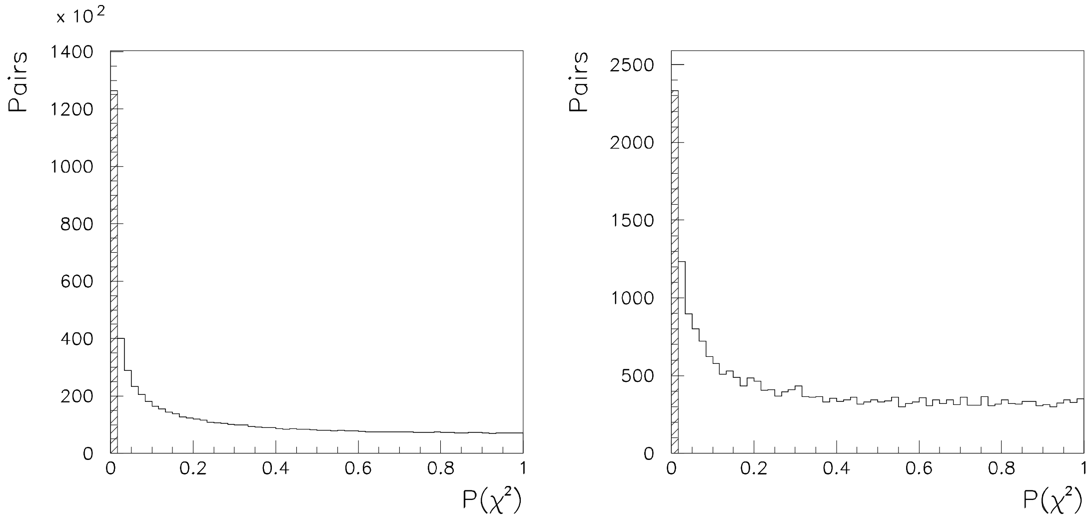

Figure 41: Distribution of the quantity $P_\chi(\chi^2)$. On the left the distribution of all track pairs is shown. On the right the same distribution after all other cuts, used to get the K_S^0 signal, is shown. The cut $P_\chi(\chi^2) > 0.01$ is indicated by the dashed area.

Figure 42 shows the result of the selection. The K_S^0 meson signal stands out clearly from the background.

7.3 The K_S^0 Meson Signal

To achieve an even clearer K_S^0 signal the other V^0 decay channels were considered. These are particularly from Λ decays of the kind of $\Lambda \longrightarrow p\pi^-$ or $\bar{\Lambda} \longrightarrow \bar{p}\pi^+$ as well as pair production from photons $\gamma \longrightarrow e^+e^-$. For each pair of tracks of the remaining K_S^0 candidates the invariant mass $m_{\text{inv}}(p\pi)$ is calculated with the assumption that the track with the larger momentum is the proton or antiproton. The distribution of $m_{\text{inv}}(p\pi)$ of all K_S^0 candidates displays a clear peak at $m_\Lambda = 1115.6\ \text{MeV}/c^2$ as can be seen in Figure 43. Many of the cuts required for the K_S^0 reconstruction are also suitable for the Λ decay. By cutting out the mass window

$$1109\ \text{MeV}/c^2 \quad < \quad m_{\text{inv}}(p\pi) \quad < \quad 1121\ \text{MeV}/c^2 \tag{89}$$

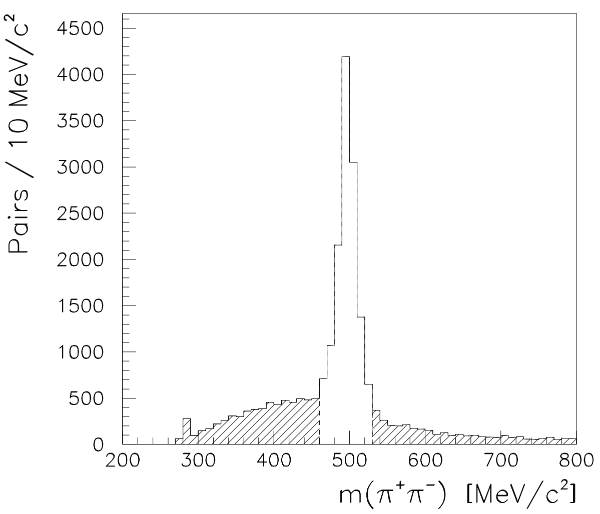

Figure 42: Invariant mass peak of the K_S^0 meson. Distribution of the invariant mass $m_{\mathrm{inv}}(\pi^+\pi^-)$ after applying the kinematical cuts. The small peak at 280 MeV/c^2 are e^+e^- pairs from γ conversion. The mass window used for the reconstruction of D^0 mesons is shown.

most of the Λ decays are eliminated.

The e^+e^- pair production by γ conversion is evident in a small peak at the threshold of the $m_{\mathrm{inv}}(\pi^+\pi^-)$ spectra as shown in Figure 42. The hypothesis is tested by plotting the distance from the decay vertex to beam axis for invariant masses of

$$m_{\mathrm{inv}}(\pi^+\pi^-) \quad < \quad 0.29 \text{ GeV}/c^2 \quad . \tag{90}$$

Pair production can only occur in material. Most of the vertices are in the region of the beam pipe wall and the chamber walls which result in two clear peaks at the corresponding radii as can be seen in Figure 43. The track pairs of a γ conversion are removed by excluding the invariant mass window

$$m_{\mathrm{inv}}(e^+e^-) \quad < \quad 50 \text{ MeV}/c^2 \quad . \tag{91}$$

Figure 44 shows the K_S^0 signal after the removal of the Λ and γ candidates.

Due to the small natural width of the K_S^0 meson, the form of the K_S^0 signal is given by the resolution of the detector and the quality of reconstruction. Therefore the invariant mass around the K^0 mass is expected to be Gaussian distributed. The deviation of the values depends upon the transverse momentum of the kaon, and are due to the limited resolution of the track chambers measuring the curvature of the tracks. Furthermore the mean value of the peak depends on the direction of the kaon and therefore also on its momentum. This is probably due to the inhomogeneities of the magnetic field. In Table 15 the parameters of the fitted Gaussian distribution for different pseudo rapidities and momentum regions are listed. Because of these differences a global fit of the K_S^0 signal was not done.

To test this analysis, the reconstructed decays are used in an attempt to determine the life time of the K_S^0 meson. The ratio of the decay length d to the momentum p of

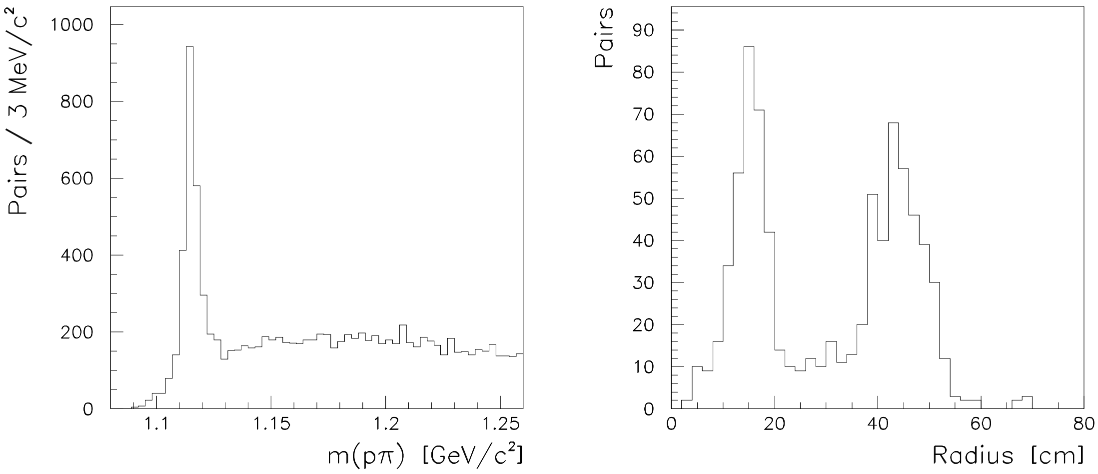

Figure 43: Identification of other V^0 candidates than the K^0 mesons. On the left, the invariant mass distribution $m_{\rm inv}(p\pi)$ of the K^0 candidates is shown. A peak at the Λ mass is visible. On the right, the radial distance of the decay vertex, assuming a γ conversion, from the beam axis for events at the kinematical threshold of the invariant mass distribution $m_{\rm inv}(\pi^+\pi^-)$ is shown. The clear peaks are located at the radii of the beam pipe and the inner multiwire proportional and z drift chambers as well as at the outer multiwire proportional and z drift chambers.

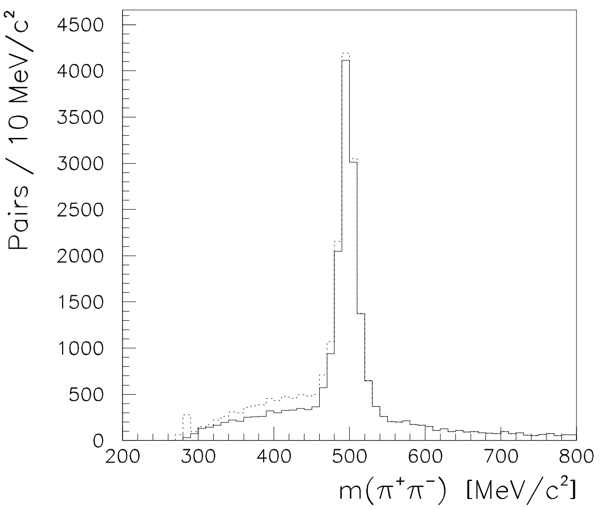

Figure 44: The K^0meson signal in the invariant mass distribution before (dotted line) and after (solid line) elimination of the Λ and γ candidates.

interval			$\overline{m}$ [MeV/c^2]	σ [MeV/c^2]
1	$< \eta <$	∞	499.3	11.3
0	$< \eta <$	1	496.7	10.7
-1	$< \eta <$	0	496.7	11.9
$-\infty$	$< \eta <$	-1	502.8	12.8
0	$< p <$	0.5	492.7	8.9
0.5	$< p <$	1	496.3	10.2
1	$< p <$	1.5	498.9	11.9
1.5	$< p <$	2	499.9	12.7
2	$< p <$	2.5	500.2	13.7
2.5	$< p <$	∞	500.9	13.6

Table 15: Mean values and standard deviation of the fitted Gaussian distributions for different pseudo rapidity η and momentum p ranges. For the fit the method of least squares is used.

the K_S^0 meson is directly proportional to its life time

$$\frac{d}{p} = \frac{\gamma v \tau}{\gamma m v} = \frac{\tau}{m} \quad \text{with} \quad \gamma = \frac{1}{\sqrt{1-\frac{v^2}{c^2}}} \quad . \tag{92}$$

The fit of the distribution of this quantity with an exponential function gives an estimation of the mean life time of the K_S^0 meson. To consider the background of wrongly combined track pairs the same reconstruction procedure is applied for track pairs with the same charge. The d/p distribution, which certainly is not produced from K_S^0 decays, is subtracted from the original d/p distribution. In addition only combinations of tracks which lie in a mass window around the K^0 mass are used.

$$0.46 \text{ GeV}/c^2 \quad < \quad m_{\text{inv}}(\pi^+\pi^-) \quad < \quad 0.55 \text{ GeV}/c^2 \tag{93}$$

For small decay times the distribution is distorted by the selection criteria, for long decay times the statistical variation becomes relatively large. Nevertheless an exponential fit is achieved within the d/p range

$$15 \text{ cm} \quad < \quad \frac{d}{p} \quad < \quad 40 \text{ cm} \tag{94}$$

with a mean life time for the K_S^0 meson of

$$c\tau \quad = \quad 2.8 \pm 0.3 \text{ cm} \quad , \tag{95}$$

as shown in Figure 45. The result is compatible with the value $c\tau = 2.676$ cm published in [31].

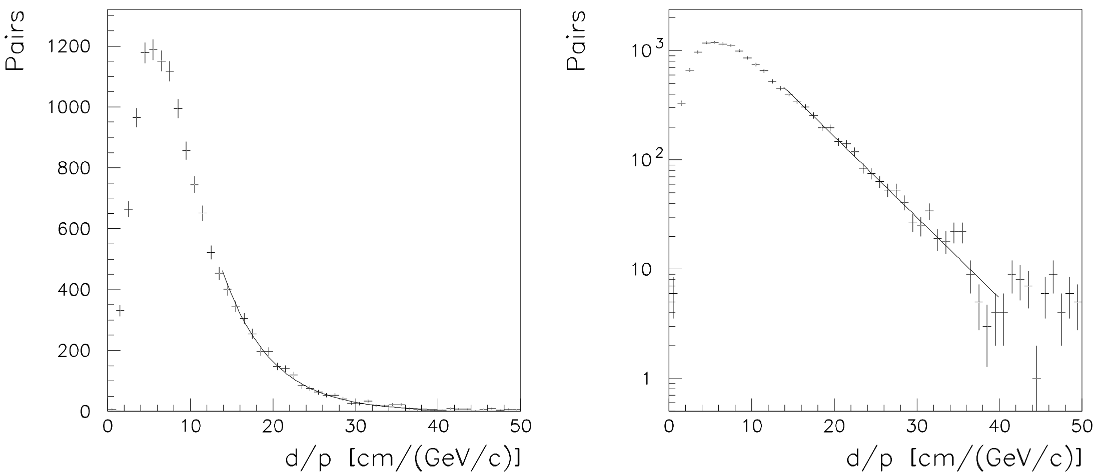

Figure 45: Distribution of the ratio of the decay length d to the momentum p of the K_S^0 meson after subtraction of the background. On the left the distribution is shown in a linear scale, on the right in a logarithmic scale. The life time of the K_S^0 meson is proportional to this ratio. An exponential fit between 15 cm $< d/p <$ 40 cm shown in the distribution gives a value $c\tau = 2.8 \pm 0.3$ cm for the life time.

7.4 The Reconstruction of D^0 Mesons

To reconstruct the decay (49), the K_S^0 candidates discussed in the previous section, whose invariant masses lie in the region of

$$0.46 \text{ GeV}/c^2 \quad < \quad m_{\text{inv}}(\pi^+\pi^-) \quad < \quad 0.55 \text{ GeV}/c^2 \tag{96}$$

are taken and combined with two additional oppositely charged tracks. No vertex fit is done.

The invariant mass of the three particles is calculated. It is assumed that the two additional tracks are pions. The energy is calculated in a similar way to (81) with the K^0 mass of

$$m_{K^0} \quad = \quad 497.672 \text{ MeV}/c^2 \quad . \tag{97}$$

The mean decay length of the D^0 meson in the laboratory frame for compatible energies is three orders of magnitude smaller than for K_S^0 mesons. Therefore the decay vertex of the D^0 meson is inseparable from the primary vertex due to the present experimental configuration at H1. The selection criteria for the K_S^0 decay can not be applied for the D^0 decay.

To identify the charm events with charm-tagging, only one additional cut on the D^0 candidates is applied.

- **DCA of the pion tracks:** Because the pions of the D^0 decay are produced practically at the primary vertex, it is expected that they have small dca values. For the two pions of the D^0 decay the requirement is again weighted with its error.

$$\frac{|dca|}{\sigma_{dca}} \quad < \quad 10 \tag{98}$$

Unfortunately the distribution of the invariant mass does not show a clearer signal at the D^0 mass for more severe cuts.

7.5 The Charm-Tagging

The masses of the decay products have to be smaller than the mass of the decaying particle. The mass difference decides if a decay is possible or not.

The mass difference between the $D^{*\pm}$ meson and the D^0 meson is only just above the pion mass. For the decay $D^{*\pm} \longrightarrow D^0\pi^\pm$ the mass difference $\triangle m$ can be measured with a much higher accuracy than the mass of the $D^{*\pm}$ meson or the D^0 meson due to the strong kinematical restriction.

The value

$$\triangle m \quad = \quad m_{D^{*\pm}} - m_{D^0} \quad = \quad 145.42 \pm 0.05 \text{ MeV}/c^2 \tag{99}$$

has to be compared with the mass of the pion $m_\pi = 139.57$ MeV$/c^2$. The pion deriving from the $D^{*\pm}$ decay has a kinetic energy of 5.8 MeV and a momentum of about 40 MeV$/c$. Therefore it is called a 'slow' or 'soft' pion. Its symbol is π_s. If it is possible to find a low momentum track in addition to the four tracks of the D^0 decay it is strong evidence for a possible $D^{*\pm}$ decay and raises the probability of having found a charm event. Although only a quarter of all D^0 mesons come from a $D^{*\pm}$ decay, the signal to background ratio gets much higher because the background from wrong combinations of tracks in this kinematical region is much more suppressed than in the direct search for D^0 mesons.

Due to the insufficient inclusive D^0 signal an attempt is made to establish the D^0 mesons over the decay of D^* resonances. The D^0 candidates with an invariant mass

$$1.81 \text{ GeV}/c^2 \quad < \quad m_{\text{inv}}(K^0_S\pi^+\pi^-) \quad < \quad 1.92 \text{ GeV}/c^2 \tag{100}$$

are taken and combined with a fifth track — 'slow' pion —, which can have a positive or a negative curvature. The difference of the invariant mass

$$\triangle m_{\text{sig}} \quad = \quad m_{\text{inv}}(K^0_S\pi^+\pi^-\pi^\pm_s) \quad - \quad m_{\text{inv}}(K^0_S\pi^+\pi^-) \tag{101}$$

is entered into a histogram, where the following kinematical restrictions were applied.

- **DCA of the fifth track:** The pion of the D^* decay is practically produced at the primary vertex. Therefore the *dca* value of the fifth track has to be small.

$$\frac{|dca|}{\sigma_{dca}} \quad < \quad 10 \tag{102}$$

- **Ratio of the momenta:** At the D^* decay only a small amount of energy becomes free. The momenta of the daughter particles D^0 and π_s are approximately proportional to their masses in the laboratory frame. The requirement is that the momentum of the D^0 meson is nine times larger than the momentum of the 'slow' pion

$$\frac{p_{D^0}}{p_{\pi_s}} \quad > \quad 9 \quad . \tag{103}$$

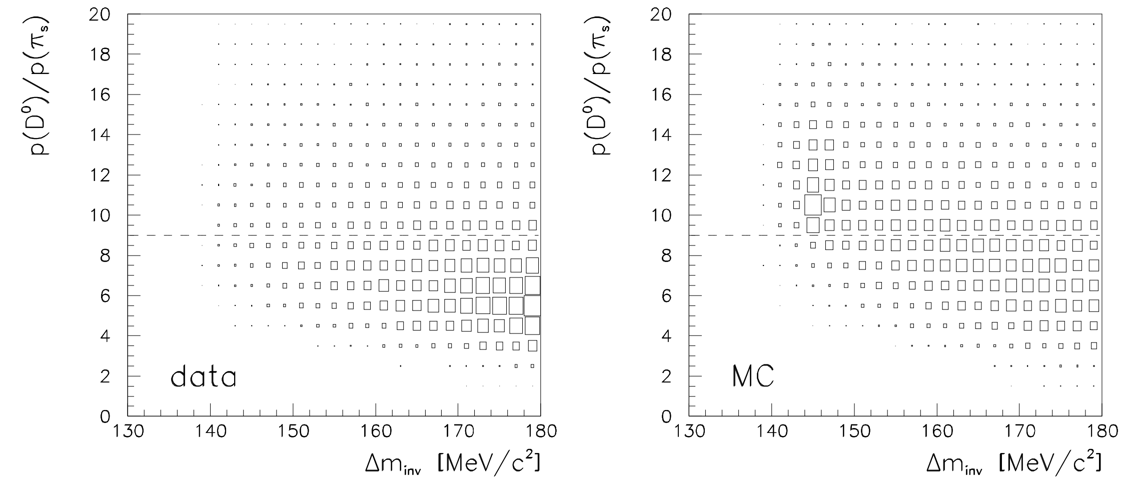

Figure 46: Two dimensional histogram to illustrate the cut on the momentum ratio p_{D^0}/p_{π_s}. The momentum ratio as a function of the invariant mass difference is shown. On the left the distribution of the *ep* data, on the right the distribution of the Monte Carlo simulated data is shown. The cut at $p_{D^0}/p_{\pi_s} > 9$ is indicated with a dashed line.

The ratio of the masses is 13.4. This cut turns out to be effective. An illustration is given in Figure 46.

- **Momentum of the 'slow' pion:** Although the 'slow' pion receives less energy from the decay, its momentum is larger than many of the background tracks because it has taken over a part of the momentum of the D^* meson. With the condition

$$p_{\pi_s} \quad > \quad 175 \text{ MeV}/c \tag{104}$$

several wrong combinations can be avoided.

The spectra of the invariant mass difference $\triangle m_{\text{sig}}$, with all cuts applied, can be seen in Figure 47. In order to test the analysis the invariant mass difference distribution $\triangle m_{\text{bgr}}$ is calculated for wrongly charged combinations. For both, the positively-positively charge combinations and the negatively-negatively charge combinations, the invariant mass differences

$$\triangle m_{bgr} \quad = \quad m_{\text{inv}}(K_S^0\pi^+\pi^+\pi^\pm) \quad - \quad m_{\text{inv}}(K_S^0\pi^+\pi^+) \tag{105}$$

and

$$\triangle m_{bgr} \quad = \quad m_{\text{inv}}(K_S^0\pi^-\pi^-\pi^\pm) \quad - \quad m_{\text{inv}}(K_S^0\pi^-\pi^-) \tag{106}$$

are entered into a histogram. The same selection criteria are applied. Comparison of the two distributions in Figures 48 shows a accumulation of correctly charged track combinations near the expected mass difference (99). This is interpreted as a signal for the production of charm quarks.

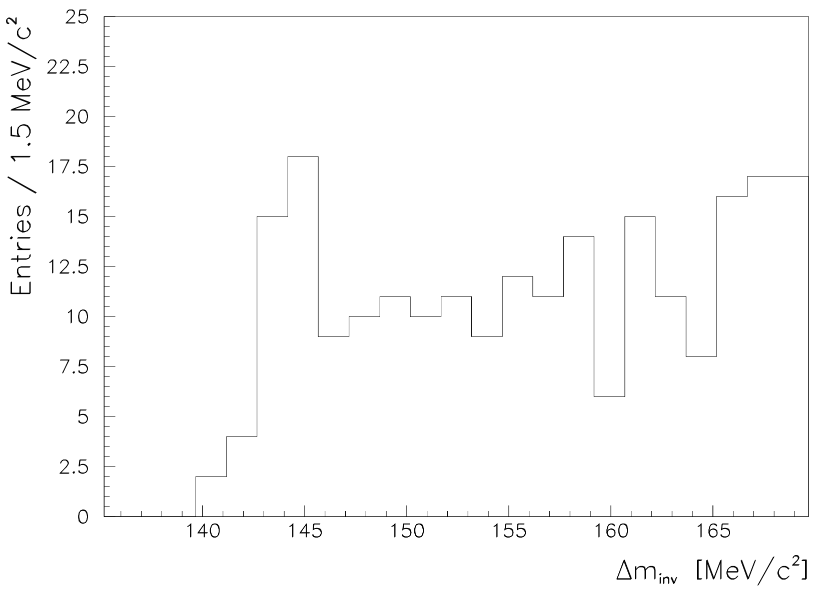

Figure 47: Invariant mass difference distribution after applying all cuts described in the text.

7.6 The Charm Signal

It can be assumed that the width of the signal is brought about by the limited resolution of the measurement and therefore the $\triangle m_{\mathrm{sig}}$ peak with a maximum around 145 MeV/c^2 is fitted with a Gaussian curve. The procedure to establish the number of $D^{*\pm}$ meson candidates is the following:

- Fitting of the background spectrum $\triangle m_{\mathrm{bgr}}$ with a function

$$F(\triangle m) \quad = \quad P_1 \cdot (\triangle m - m_{\pi^\pm})^{P_2} \quad . \tag{107}$$

- Adjusting the background spectrum fit to the background in the distribution of the signal by scaling the curve but fixing its shape. The achieved function is of the form

$$F(\triangle m) \quad = \quad P_1 \cdot (\triangle m - m_{\pi^\pm})^{P_2} \cdot P_3 \quad . \tag{108}$$

- Fitting of the real $\triangle m_{\mathrm{sig}}$ spectrum with the sum of the background fit and a Gaussian curve

$$F(\triangle m) \quad = \quad P_1 \cdot (\triangle m - m_{\pi^\pm})^{P_2} \cdot P_3 + P_4 \cdot e^{-\frac{1}{2}\cdot\left(\frac{\triangle m - P_5}{P_6}\right)^2} \quad . \tag{109}$$

The variables P_1 to P_5 are the parameters of the fit. For the fits the method of least squares is used.

Due to the low statistics, the result of the fits depends strongly on the binning of the histogram and the assumed background shape. The chosen bin width is 1.5 MeV/c^2. For smaller bin widths the signal disappears, for larger bin widths the fits are even more uncertain.

The obtained fit of a Gaussian distribution to the signal is shown in Figure 48 and described by the following parameters:

$$\begin{array}{ll} \text{Mean value } \overline{\triangle m_{\text{sig}}}: & 144.46 \pm 0.41 \text{ MeV}/c^2 \\ \text{Standard deviation } \sigma: & 0.76 \pm 0.35 \text{ MeV}/c^2 \quad . \end{array}$$

The number of $D^{*\pm}$ meson candidates corresponding to the fitted peak is 16 ± 9.

Due to the uncertainties of fitting the signal distribution an easier method is used to determine the number of $D^{*\pm}$ meson candidates. Within a 3.8 MeV/c^2 wide interval around the $D^{*\pm}$ meson signal in the $\triangle m_{\text{inv}}$ distribution

$$142.6 \text{ MeV}/c^2 \quad < \quad \triangle m_{\text{inv}} \quad < \quad 146.4 \text{ MeV}/c^2 \quad , \tag{110}$$

this corresponds to a $\triangle m_{\text{sig}}$ range of 2.5 standard deviations from the fit in Figure 48, the number of background candidates and signal candidates are counted. The number of $D^{*\pm}$ meson candidates is given by the difference of the two numbers

$$N \quad = \quad N_{\text{sig}} - N_{\text{bgr}} \quad = \quad 19 \pm 8 \quad . \tag{111}$$

This is allowed because the scaling parameter P_3 in equation (109) is one within its error. The number of $D^{*\pm}$ candidates with this method agree within the error with the numbers obtained from the fits. This method of determining the number of $D^{*\pm}$ candidates has the advantage that also the number of $D^{*\pm}$ candidates triggered by each subtrigger can be determined.

When reconstructing decays of five tracks a large part of the background comes from using the wrong combinations. It is possible to get several entries in the histogram, because the reconstruction of the decay with the same five tracks but in a different permutation also may give a valid entry. If an event has a jet with several similar tracks, these can be exchanged and give also several entries in the histogram. This combinatorial background is also included in the spectra of the wrong charged track combinations. The possibility that there are two $D^{*\pm}$ mesons decay in the same channel, is very low and can be neglected. In the data, no event was found with two D^* candidates.

In the $\triangle m_{\text{sig}}$ region (110), 25 % of the entries are combinatorial background, but their $\triangle m_{\text{inv}}$ values are smoothly spread over the whole region and are not the reason for the peak in the $\triangle m_{\text{inv}}$ distribution. This background is due to multiple entries of the same event in the invariant mass distribution. In the background spectra of wrong combined charged tracks, 24 % of the entries in the $\triangle m_{\text{bgr}}$ region (110) are due to combinatorial background. These values agree very well within statistical errors.

If the peak in the $\triangle m_{\text{inv}}$ spectra is related to the $D^{*\pm}$ meson decay the invariant mass distribution of the D^0 candidates should show a peak. Therefore the invariant mass $m_{\text{inv}}(K^0_S\pi^+\pi^-)$ is histogrammed for all track combinations with a $\triangle m_{\text{sig}}$ value within the same 2.5 standard deviations of the calculated mean value

$$142.6 \text{ MeV}/c^2 \quad < \quad \triangle m_{\text{sig}} \quad < \quad 146.4 \text{ MeV}/c^2 \quad . \tag{112}$$

The histogram is shown in Figure 49. The signal is fitted with a Gaussian distribution and the underlying background with a polynomial. The obtained fit to the signal is

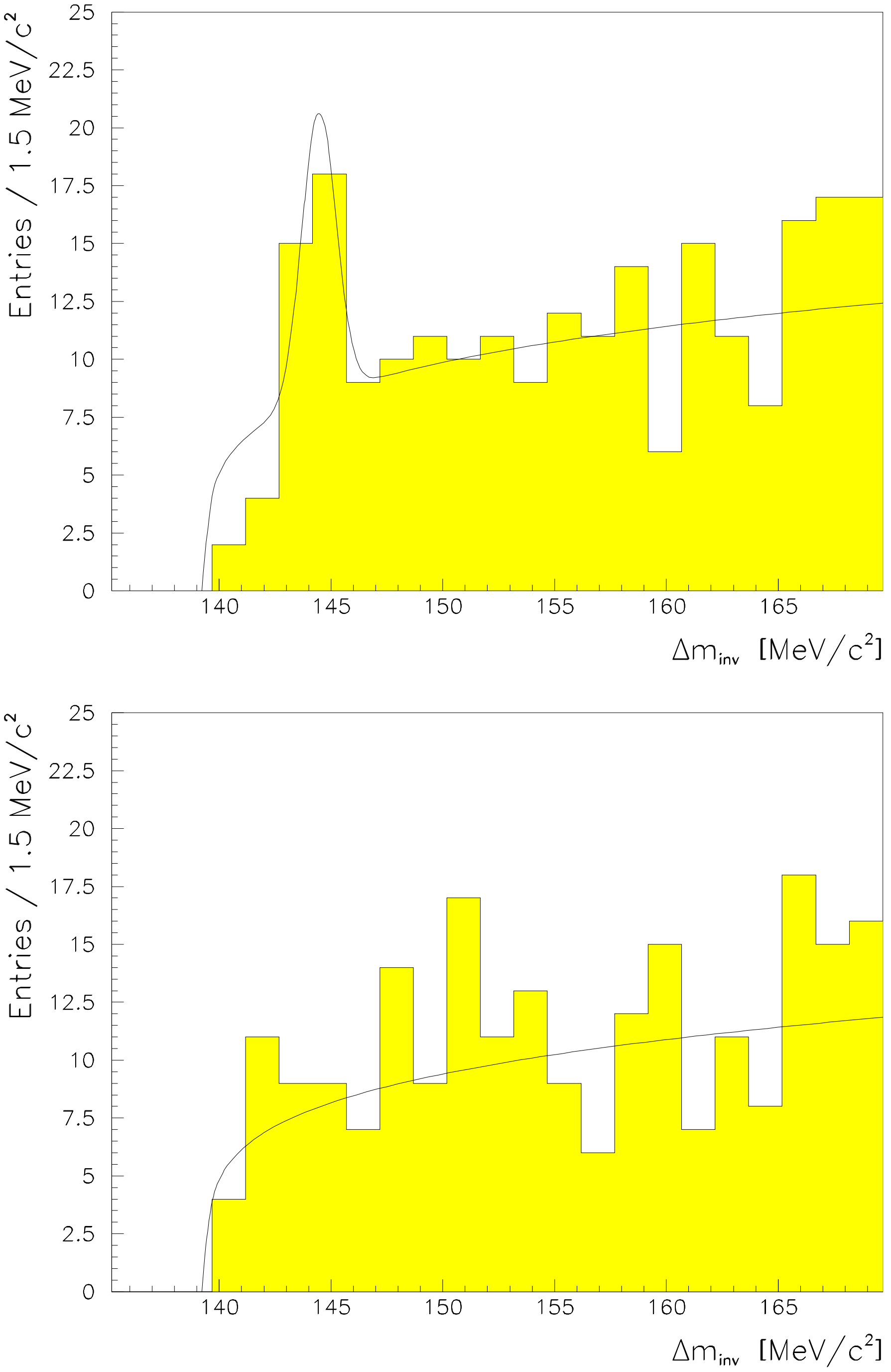

Figure 48: Invariant mass difference $\triangle m_{\mathrm{inv}}$ distribution after applying all cuts described in the text for different charge signs — signal distribution — on the top and for equal charge signs — background distribution — on the bottom. The bin width is 1.5 MeV/c^2. The solid lines are corresponding fits described in the text.

described by the following parameters:

$$\begin{array}{ll}\text{Mean value } \overline{m_{\text{inv}}(K_S^0\pi^+\pi^-)}: & 1886 \pm 43 \text{ MeV}/c^2 \\ \text{Standard deviation } \sigma: & 76 \pm 37 \text{ MeV}/c^2 \quad .\end{array}$$

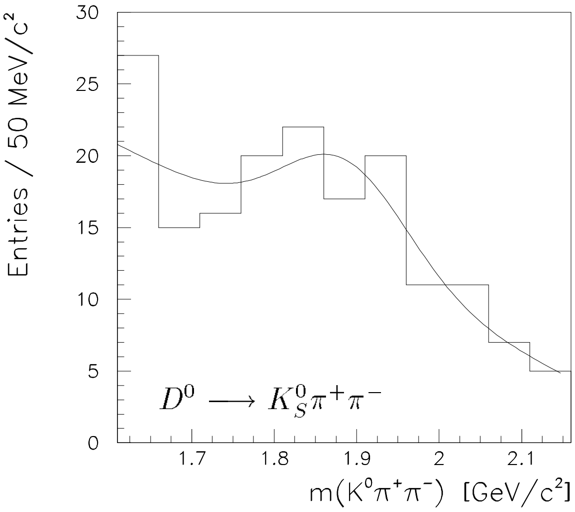

Figure 49: Invariant mass peak of the D^0 meson. Distribution of the invariant mass $m_{\text{inv}}(K_S^0\pi^+\pi^-)$ for all track combination with an invariant mass difference in $142.6\text{ MeV}/c^2 < \triangle m_{\text{sig}} < 146.4\text{ MeV}/c^2$.

The same procedure can also be used to obtain the $D^{*\pm}$ signal. The histogram is shown in Figure 50. The signal is fitted with a Gaussian distribution, the underlying background with a polynomial. The obtained fit to the signal is described by the following parameters:

$$\begin{array}{ll}\text{Mean value } \overline{m_{\text{inv}}(K_S^0\pi^+\pi^-\pi_s^\pm)}: & 2031 \pm 38 \text{ MeV}/c^2 \\ \text{Standard deviation } \sigma: & 65 \pm 33 \text{ MeV}/c^2 \quad .\end{array}$$

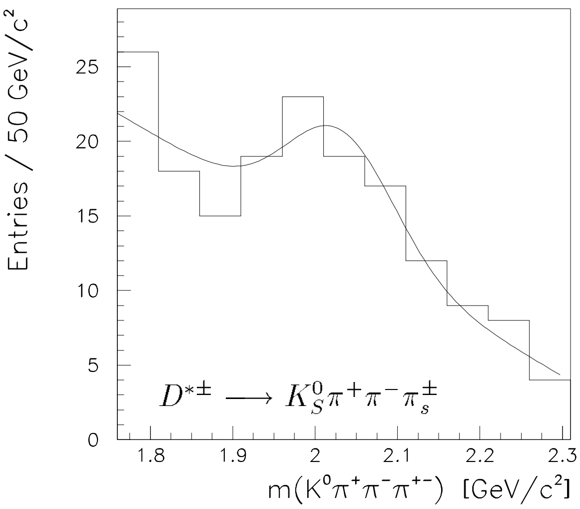

Figure 50: Invariant mass peak of the $D^{*\pm}$ meson. Distribution of the invariant mass $m_{\rm inv}(K^0_S\pi^+\pi^-\pi_s^\pm)$ for all track combination with an invariant mass difference in $142.6\ \mathrm{MeV}/c^2 < \triangle m_{\rm sig} < 146.4\ \mathrm{MeV}/c^2$.

8 Determination of the Charm Cross Section

In this section the charm production cross section is determined. The found number of $D^{*\pm}$ decays is scaled with acceptances and efficiencies and finally compared with the total luminosity corresponding to the found events.

8.1 Method

To obtain a quantitative estimation of the charm production at HERA the cross section $\sigma(ep \longrightarrow ec\bar{c}X)$ has to be determined. For the calculation of σ from the event rate n the definition of the luminosity $\mathcal{L}$ is used

$$\sigma = \frac{n}{\mathcal{L}} \quad . \tag{113}$$

The integration of the event rate over the period of data taking gives the total of all processes which contribute to the cross section. The number N_{tot} of all $c\bar{c}$ pairs has to be calculated from the number of observed events N. In this case the equation (113) becomes

$$\sigma = \frac{N}{L \cdot P \cdot \epsilon} \quad , \tag{114}$$

where L is integrated luminosity, P is the total probability of the fragmentation and of the decay in the decay channel, equation (59), which is used for this analysis, and ϵ is the probability of recording an event. The probability that the decay is recorded in the detector and that it passes all cuts in the reconstruction and the selection are included in the probability ϵ.

The number of observed decays N is determined as follows:
A 3.8 MeV/c^2 wide interval is chosen in the $\triangle m_{\mathrm{sig}}$ distribution

$$142.6 \text{ MeV}/c^2 < \triangle m_{\mathrm{sig}} < 146.4 \text{ MeV}/c^2 \quad . \tag{115}$$

The entries in this interval of correct and wrongly charged combinations are counted. The number of $D^{*\pm}$ meson candidates N are traced back to real decays

$$N = N_{\mathrm{sig}} - N_{\mathrm{bgr}} \quad . \tag{116}$$

The quantity ϵ includes the acceptance of the detector as well as the efficiency of recording and reconstructing the events, the tracks and the determination method. The Monte Carlo simulation of events is an important tool to determine efficiencies. For the simulated events, exactly the same reconstruction and selection criteria are used as for the data. The ratio of the remaining events to the total number of events gives an estimation of the efficiency.

8.2 The Choice of the Subtrigger

Most of the analyzed events of the D^0 signal are triggered by the following three subtriggers:

st44 = zVtx_sig1 && DCRPhi_Tc && DCRPhi_TNeg && DCRPhi_THigh && FwdRay_T0 && !ToF_BG && !CIP_Backward

st48 = zVtx_sig1 && BPC && DCRPhi_Tc && DCRPhi_TNeg && DCRPhi_T0 && !ToF_BG && !CIP_Backward

st83 = eTAG && DCRPhi_Ta && zVtx_T0 && !ToF_BG

These are combinations of the following trigger elements provided from the first level triggers described in Section 3.3. The meaning of these trigger elements are described below:

- **zVtx_T0:** At least one entry in the z-vertex trigger histogram filled with the z position on the beam axis of rays formed by the fired pads of the CIP and COP.
- **zVtx_sig1:** A significant peak in the z-vertex trigger histogram filled with the z position on the beam axis of rays formed by the fired pads of the CIP and COP. The significance criterion to be fulfilled is

$$\sigma = \frac{p-b}{\sqrt{p}} > 1.5 \quad , \tag{117}$$

  where p is the content of the peak bin and b is the average number of entries in all other bins of the 16 bin wide histogram.
- **DCRPhi_T0:** At least one track with a transverse momentum higher than 420 MeV/c is found by the drift chamber r-φ trigger and in addition the prompt bit of the mask of the track.
- **DCRPhi_Ta:** At least one track with a transverse momentum higher than 420 MeV/c is found by the drift chamber r-φ trigger.
- **DCRPhi_Tc:** At least three tracks with a transverse momentum higher than 420 MeV/c is found by the drift chamber r-φ trigger.
- **DCRPhi_TNeg:** At least one track with a transverse momentum higher than 420 MeV/c and negative charge is found of the drift chamber r-φ trigger.
- **DCRPhi_THigh:** At least one track with a transverse momentum higher than 800 MeV/c is found by the drift chamber r-φ trigger.
- **FwdRay_T0:** At least one ray formed by the FPC is provided by the forward ray trigger.
- **BPC:** Three out of four planes of the BPC have registered a hit.

- **eTAG:** The electron detector, which is used to measure the luminosity, has detected energy.
- **!ToF_BG:** No hit is found in the scintillators of the time of flight system in the background timing window derived from the HERA clock signal.
- **!CIP_Backward:** Not more than three sectors of the backward quarter of the CIP are active.

The trigger efficiencies for these three subtriggers are derived from the Monte Carlo simulation and are given with the statistical errors in Table 16. These efficiencies result from events with $D^{*\pm}$ meson decays described in equation (49) which have all decay products within the acceptance of

$$|\eta| \quad < \quad 1.75 \quad . \tag{118}$$

The acceptance of η has to be slightly larger than those of the central jet chambers which define the acceptance needed for this analysis. Larger acceptance is not necessary because these additional tracks cannot be measured in the central jet chambers. There is no restriction for the scattered electron; no cut on the variable y is applied. The low efficiency of the subtrigger st83 is due to the limited acceptance in y of the electron detector shown in Figure 51 which is included in the trigger efficiency.

The difference between the direct and the resolved component can be explained by the different averaged number of tracks in the central tracker region. For the direct component of the photon gluon fusion the averaged number of tracks above 400 MeV/c transverse momentum is 6 and for the resolved component it is 8. This leads to higher efficiencies of the drift chamber r-φ trigger for the resolved component.

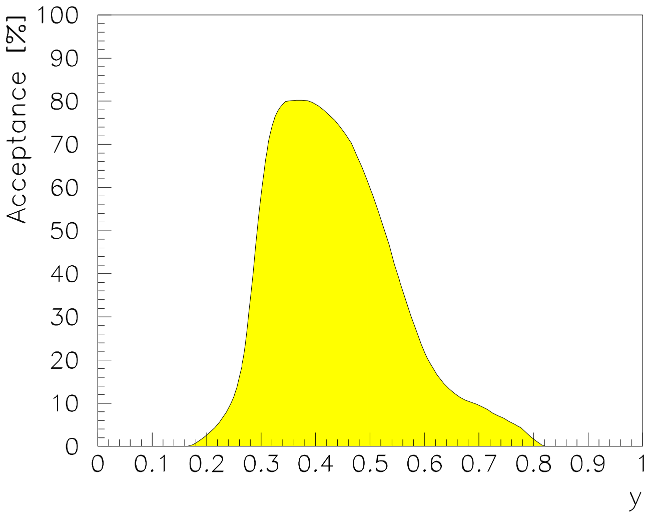

Figure 51: The electron tagger acceptance as a function of the kinematical scaling variable y.

The level 4 filter farm verifies the decisions of the level 1 triggers by recalculating the trigger conditions. In addition it applies some background rejection cuts to remove

subtrigger	direct component	resolved component
st44	13.53 ± 0.56 %	22.57 ± 0.78 %
st48	22.69 ± 0.79 %	40.17 ± 1.15 %
st83	11.75 ± 0.52 %	22.90 ± 0.79 %

Table 16: Subtrigger efficiencies after the level 1 trigger derived from Monte Carlo simulation.

the proton beamwall and proton gas interactions. The trigger efficiencies after the level 4 trigger step are given with statistical errors in Table 17.

subtrigger	direct component	resolved component
st44	11.03 ± 0.50 %	21.51 ± 0.75 %
st48	21.43 ± 0.76 %	39.18 ± 1.13 %
st83	11.75 ± 0.52 %	22.83 ± 0.78 %

Table 17: Subtrigger efficiencies after the level 4 trigger derived from Monte Carlo simulation.

8.3 The Luminosity

The luminosity delivered by HERA to the H1 experiment is measured using the rate of the Bethe-Heitler process $ep \longrightarrow ep\gamma$. The cross section is large and within quantum electrodynamics exactly calculable. The scattered electron and photon are measured in the electron and photon detector in coincidence as previously mentioned in Section 2.2.

Unfortunately the background process in this measurement, the scattering of electrons from the beam with molecules of the remnant gas in the beam pipe, has an even larger cross section. These processes $eA \longrightarrow eA\gamma$ have the same signature as the Bethe-Heitler process. To get a measurement of these background processes some of the electron bunches in the storage ring are pilot bunches. These bunches do not have a colliding proton bunch partner. They can only collide with the remnant gas in the beam pipe and give therefore a good measurement of the background processes. These background rates are normalized to the total number of bunches and to the bunch currents and are subtracted from the rates measured during ep collisions.

The total integrated luminosity for the data of the period in 1993, which is used in this analysis, becomes

$$L_{\mathrm{tot}} \quad = \quad \int \mathcal{L}\, dt \quad = \quad 319 \ \mathrm{nb}^{-1} \quad . \qquad (119)$$

In addition this luminosity measurement needs some further corrections:

- Due to the acceleration of the protons with high frequency cavities, whose frequency is much higher than the bunch crossing frequency, some of the protons are not in the correct bunch. They are situated in smaller bunches with a distance of the period of the high frequency of the cavities before and after the nominal bunch. These satellite bunches contribute to the luminosity measurement because they also collide with electron bunches, but their interactions do not lie in the interaction zone and are therefore rejected by the track criteria. The correction to the luminosity measurement is $3.3^{+3.3}_{-1.2}$ % for the year 1993.

- Sometimes it happens that some parts of the detector are not functioning during data taking. For example it is not possible to measure tracks in the central jet chamber after it has tripped and the high voltage turned off. The luminosity is integrated for this analysis only over the time period in which relevant detector parts were functioning.

- To reduce the dead time of the whole data acquisition system some of the subtriggers had to be prescaled. Not every event, which was triggered by a subtrigger, was read-out. The prescale value determines the fraction of the read-out data. This value could change several times during the period of data taking because the system was always adjusted to new situations such as higher trigger efficiencies or better beam conditions.

  The prescale values p for the chosen subtriggers weighted averaged over the run period of 1993 are

$$\begin{aligned} p_{\mathrm{st44}} &= 0.504 \\ p_{\mathrm{st48}} &= 0.729 \\ p_{\mathrm{st83}} &= 0.003 \quad . \end{aligned} \tag{120}$$

  The fraction f of events which pass the system is given by the prescale value p with the equation

$$f = \frac{1}{1+p} \quad . \tag{121}$$

For the above chosen subtriggers the following integrated luminosities are found after the corrections have been applied:

$$\begin{aligned} L_{\mathrm{st44}} &= 186\ \mathrm{nb}^{-1} \\ L_{\mathrm{st48}} &= 161\ \mathrm{nb}^{-1} \\ L_{\mathrm{st83}} &= 278\ \mathrm{nb}^{-1} \quad . \end{aligned} \tag{122}$$

8.4 The Acceptance and the Efficiency

The total efficiency of the reconstruction is given by the product of the efficiencies of the several reconstruction cuts

$$\epsilon_{\mathrm{tot}} = \prod_i \epsilon_i \quad , \tag{123}$$

provided they are independent of each other. Often the efficiencies of successive cuts are correlated and therefore the product of the efficiencies delivers too small a result.

The cuts of the event selection are, for example, rather similar to the cuts of the reconstruction of the K_S^0 meson. Therefore the efficiency and the acceptance of the detector are determined in one single step, by taking the Monte Carlo simulation to achieve an estimation.

The efficiencies of the different subtriggers are discussed is Section 8.2 for the different Monte Carlo calculations.

The acceptance $\mathcal{A}$ of the $D^{*\pm}$ meson decaying to five pions through the channel in equation (49), where all five tracks still can be measured in the central part of the detector, is calculated with the Monte Carlo simulation program for the direct and the resolved contribution separately. The derived numbers for the acceptance in this decay channel are:

$$\begin{aligned} \mathcal{A}_{\text{direct}} &= 12.88 \pm 0.19 \ \% \\ \mathcal{A}_{\text{resolved}} &= \ \ 6.27 \pm 0.08 \ \% \quad . \end{aligned} \tag{124}$$

Because the efficiency and the acceptance of a subtrigger are correlated, it is not correct to multiply the two numbers to achieve the overall probability to measure a decay. The probability has also to be calculated with the Monte Carlo simulation.

The mixing ratio between the direct component and the resolved component of the photon gluon fusion is taken as 3 : 1; i. e. 75 % of direct and 25 % of resolved component. All numbers are summarized in the Table 18.

	direct contribution		
subtrigger	efficiency	acceptance	efficiency $\otimes$ acceptance
st44	11.03 $\pm$ 0.50 %	12.88 $\pm$ 0.19 %	1.42 $\pm$ 0.05 %
st48	21.43 $\pm$ 0.76 %	12.88 $\pm$ 0.19 %	2.76 $\pm$ 0.08 %
st83	11.75 $\pm$ 0.52 %	12.88 $\pm$ 0.19 %	1.51 $\pm$ 0.06 %
	resolved contribution		
subtrigger	efficiency	acceptance	efficiency $\otimes$ acceptance
st44	21.51 $\pm$ 0.75 %	6.27 $\pm$ 0.08 %	1.34 $\pm$ 0.04 %
st48	39.18 $\pm$ 1.13 %	6.27 $\pm$ 0.08 %	2.44 $\pm$ 0.05 %
st83	22.83 $\pm$ 0.78 %	6.27 $\pm$ 0.08 %	1.43 $\pm$ 0.04 %
	75 % direct + 25 % resolved contribution		
subtrigger	efficiency	acceptance	efficiency $\otimes$ acceptance
st44	13.65 $\pm$ 0.56 %	10.19 $\pm$ 0.15 %	1.39 $\pm$ 0.05 %
st48	25.87 $\pm$ 0.85 %	10.19 $\pm$ 0.15 %	2.63 $\pm$ 0.07 %
st83	14.52 $\pm$ 0.59 %	10.19 $\pm$ 0.15 %	1.48 $\pm$ 0.05 %

Table 18: Efficiencies and acceptances of the subtriggers st44, st48 and st83 for the direct and resolved contribution of the photon gluon fusion process of charm production.

To be able to calculate the efficiency ϵ for measuring the decay some other corrections are needed:

- Because in the Monte Carlo simulation only the decay channels of the D mesons are imposed, there is a correction for the K_S^0 meson decay. It is only looked for with the decay channel $K_S^0 \longrightarrow \pi^+\pi^-$ for the K_S^0 meson and therefore there is a correction factor of the value of the branching ratio $\mathcal{B}(K_S^0 \longrightarrow \pi^+\pi^-)$.

- The probability to correctly reconstruct a track from the hits in the central jet chambers is not equal for events from data and events produced by Monte Carlo simulations. The reason for this difference is noise in the chambers and readout problems. Almost all tracks are found, but in some cases the reconstructed track parameters are obviously wrong.

  The track finding efficiency was found by a visual scanning of events using the event display. The efficiency for tracks is for data events

$$\epsilon_{\text{track}}^{\text{data}} = 89 \pm 2\ \% \tag{125}$$

  and for Monte Carlo events

$$\epsilon_{\text{track}}^{\text{MC}} = 95 \pm 2\ \% \quad . \tag{126}$$

  The ratio of both efficiencies has to be applied for each of the five tracks of the decay.

- With the described reconstruction method of $D^{*\pm}$ decays resonant as well as nonresonant decays are found but in the Monte Carlo simulation only nonresonant decays were generated. Therefore a correction factor for the efficiency of

$$\mathcal{R} = \frac{\mathcal{B}\left(D^0 \longrightarrow \bar{K}^0\pi^+\pi^-\right)_{\text{all}}}{\mathcal{B}\left(D^0 \longrightarrow \bar{K}^0\pi^+\pi^-\right)_{\text{nonresonant}}} \tag{127}$$

$$= \frac{(5.3 \pm 0.6)\ \%}{(1.43 \pm 0.26)\ \%} = 3.71 \pm 1.09 \tag{128}$$

  has to be applied.

With these corrections the efficiency of reconstructing and measuring the whole decay is given by

$$\epsilon = \frac{N_{\text{st}}^{\text{MC}}}{N_{\text{tot}}^{\text{MC}}} \cdot \frac{1}{\mathcal{B}\left(K_S^0 \longrightarrow \pi^+\pi^-\right)} \cdot \left(\frac{\epsilon_{\text{track}}^{\text{data}}}{\epsilon_{\text{track}}^{\text{MC}}}\right)^5 \cdot \mathcal{R} \quad , \tag{129}$$

where $N_{\text{tot}}^{\text{MC}}$ is the total number of simulated and reconstructed Monte Carlo events and $N_{\text{st}}^{\text{MC}}$ the number of found $D^{*\pm}$ mesons in the same invariant mass difference interval as for data.

8.5 Reconstructed Decays

The number of observed decays within the invariant mass difference interval

$$142.5\ \text{MeV}/c^2 < \triangle m_{\text{inv}} < 146.1\ \text{MeV}/c^2 \tag{130}$$

is

$$N = 40 - 21 = 19 \pm 8 \quad . \tag{131}$$

as already mentioned in Section 8.1. For the three chosen subtriggers the following numbers of observed decays are found in the same invariant mass difference interval:

$$N_{\mathrm{st44}} = 21 - 8 = 13 \pm 5 \tag{132}$$

$$N_{\mathrm{st48}} = 21 - 14 = 7 \pm 6 \tag{133}$$

$$N_{\mathrm{st83}} = 13 - 8 = 5 \pm 4 \quad . \tag{134}$$

The number of decays, which have triggered at least by one of these subtriggers, is

$$N_{\mathrm{st44,st48,st83}} = 34 - 21 = 13 \pm 7 \quad . \tag{135}$$

For the Monte Carlo simulated events the same reconstruction program is used and the same cuts as for data are applied. The achieved number of found decays for the two types of event generators are given in Table 19. For the sum of the events triggered by the three subtriggers the prescaling of the central level 1 trigger is also simulated with the prescale values given in equation (120). To be able to compare the results from the Monte Carlo simulated events with the data, the two types of Monte Carlo events are mixed with the ratio 3 : 1; i. e. 75 % of direct and 25 % of resolved component of the photon gluon fusion, the same ratio as it is used in Section 8.4.

selection	direct contribution	resolved contribution
Total generated decays	66532	136815
Total generated decays with acceptance of central tracker	8569	8574
Found $D^{*\pm}$ mesons of st44	50 ± 7	92 ± 12
Found $D^{*\pm}$ mesons of st48	58 ± 8	132 ± 14
Found $D^{*\pm}$ mesons of st83	31 ± 6	59 ± 9
Found $D^{*\pm}$ mesons of st44, st48, st83 with simulated prescaling	76 ± 9	143 ± 14

selection	75 % direct + 25 % resolved contribution
Total generated events	84103
Total generated events with acceptance of central tracker	8570
Found $D^{*\pm}$ mesons of st44	59.00 ± 8.25
Found $D^{*\pm}$ mesons of st48	73.50 ± 9.50
Found $D^{*\pm}$ mesons of st83	38.00 ± 5.50
Found $D^{*\pm}$ mesons of st44, st48, st83 with simulated prescaling	92.75 ± 10.25

Table 19: Number of generated Monte Carlo events and the number of those which passed the selection criteria identical to those applied for the recorded data.

8.6 Error Estimation

8.6.1 Statistical Error

The difference of the number of events found in the signal distribution and in the background distribution has a statistical error for the charm cross section determination of 54 %.

8.6.2 Systematic Error

The different sources for systematic errors are given in the following listing, together with the numbers for the charm production cross section.

- The error of the luminosity measurement is 4.5 % [76].
- The probability of the fragmentation of a charm quark to a $D^{*\pm}$ meson, which decays in the searched decay channel, has an uncertainty of 22 %. This leads to the same systematic error in the charm cross section determination.
- The ratio between the track reconstruction efficiency for the data and for Monte Carlo simulation has an error of 2 %. This leads to a systematic error in the charm cross section determination of 10 %.
- A large fraction of the systematic errors comes from the determination of the $D^{*\pm}$ meson reconstruction efficiency by Monte Carlo simulation. This efficiency depends on several parameters of the event generator.
  - The fraction of $D^{*\pm}$ mesons, which decay within the detector acceptance, varies with applying different proton and photon structure functions in the event generator. The variation changes the fraction by up to 20 %.
  - The ratio between the direct and the resolved component of the photon gluon fusion has not been yet measured at the HERA energy. The resolved component was estimated to be less than 30 % [14, 16]. To estimate the error of the ratio of 3 : 1, it was varied between 2 : 1 and 4 : 1. Due to the small differences in the decay detection efficiency between the direct and the resolved component, the introduced systematic error is smaller than 3 %.
  - The distribution of the calculated kinematical quantities agree quite well between the data and the Monte Carlo simulation. Therefore the applied cuts to achieve the invariant mass difference distribution $\triangle m_{\mathrm{inv}}$ should have the same effects in both cases. The contributed systematic error of the selection is estimated to be below 20 %.

  All these factors of uncertainties of the efficiency together give an estimation for the systematical error from the Monte Carlo simulation of 28 %.

The contributions to the systematic error are assumed to be not correlated and therefore can be summed quadratically. This gives a total systematic error for the charm cross section determination of 38 %.

8.7 Results

With the above method and applying equations (114) and (129), the cross section for the charm production becomes for all events triggered from at least one of the three subtriggers st44, st48 and st83

$$\sigma\left(ep \longrightarrow ec\bar{c}X\right) = 1.62 \pm 0.87_{\text{stat.}} \pm 0.62_{\text{syst.}}\ \mu\text{b} \quad . \tag{136}$$

For a consistency check, the cross section for the charm production is also calculated for each subtrigger separately. The results should be the same within the errors, but with much larger statistical errors.

$$\sigma\left(ep \longrightarrow ec\bar{c}X\right)_{\text{st44}} = 3.81 \pm 1.47_{\text{stat.}} \pm 1.45_{\text{syst.}}\ \mu\text{b} \tag{137}$$

$$\sigma\left(ep \longrightarrow ec\bar{c}X\right)_{\text{st48}} = 1.90 \pm 1.63_{\text{stat.}} \pm 0.72_{\text{syst.}}\ \mu\text{b} \tag{138}$$

$$\sigma\left(ep \longrightarrow ec\bar{c}X\right)_{\text{st83}} = 1.52 \pm 1.22_{\text{stat.}} \pm 0.58_{\text{syst.}}\ \mu\text{b} \quad . \tag{139}$$

The result can be compared with the theoretical calculations of Ellis and Nason [14], which have been discussed in Section 1.2. For the most probable charm-quark mass of 1.5 GeV/c^2 they obtained for the charm cross section a value of

$$\sigma\left(ep \longrightarrow ec\bar{c}X\right) = 0.68\ ^{+0.26}_{-0.18}\ \mu\text{b} \quad . \tag{140}$$

The charm production measured in this analysis is in agreement with this value within the errors. It is also in agreement using the values for the charm-quark masses of 1.2 GeV/c^2 and 1.8 GeV/c^2 in the theoretical calculations.

For a certain y range it is possible to calculate the total cross section for the photoproduction of a pair of charm quarks. Starting from equation (16) the cross section for the photoproduction of a pair of charm quarks is given by

$$\sigma\left(\gamma p \longrightarrow c\bar{c}X\right) = \frac{\sigma\left(ep \longrightarrow ec\bar{c}X\right)}{\int_{y_{\min}}^{y_{\max}} F_{\gamma/e}\left(y\right)\ \mathrm{d}y} \cdot \mathcal{A}\left(y_{\min}, y_{\max}\right) \quad . \tag{141}$$

The y interval is given by the edges $y_{\min}$ and $y_{\max}$. Over this interval the photon flux factor $F_{\gamma/e}$, see equation (20), has to be integrated. The fraction of events with a y within the interval between $y_{\min}$ and $y_{\max}$ of the whole y range is described by $\mathcal{A}$. This number has to be determined by the Monte Carlo simulation by the ratio

$$\mathcal{A}\left(y_{\min}, y_{\max}\right) = \frac{N_{\triangle y}}{N_{\text{tot}}} \quad . \tag{142}$$

A natural interval of the variable y is the acceptance of the electron tagger. The photon flux factor integrated over the y range

$$0.3 < y < 0.7 \tag{143}$$

and the Q^2 range

$$3 \cdot 10^{-8}\ \text{GeV}^2/c^2 < Q^2 < 100\ \text{GeV}^2/c^2 \tag{144}$$

gives

$$\int_{y_{\min}}^{y_{\max}} F_{\gamma/e}(y)\ \mathrm{d}y \quad = \quad \int_{0.3}^{0.7} F_{\gamma/e}(y)\ \mathrm{d}y \quad = \quad 0.0256 \quad . \tag{145}$$

The y and Q^2 ranges implicate a center of mass energy of the γp system in the region of

$$160\ \mathrm{GeV} \quad < \quad W_{\gamma p} \quad < \quad 250\ \mathrm{GeV} \quad . \tag{146}$$

For this region the acceptance $\mathcal{A}$ given by the Monte Carlo calculation is

$$\begin{aligned} \mathcal{A}_{\mathrm{direct}} &= 0.176 \pm 0.006 \\ \mathcal{A}_{\mathrm{resolved}} &= 0.266 \pm 0.008 \quad . \end{aligned} \tag{147}$$

With these values, mixed with the ratio 3 : 1 of direct and resolved component, the γp cross section for charm production can be determined

$$\sigma(\gamma p \longrightarrow c\bar{c}X) \quad = \quad 12.6 \pm 7.1_{\mathrm{stat.}} \pm 5.2_{\mathrm{syst.}}\ \mu\mathrm{b} \quad . \tag{148}$$

This result can be compared with the measurements of the several fixed target experiments, where an intensive photon beam has been collided with a fixed proton target. These measured cross sections are given in Figure 52 as a function of the center of mass energy of the γp system. The calculations of Frixione *et al.* [77] with the proton structure function MRSA[23] [78] and the photon structure function GRV-G HO[24] [74] for the charm-quark mass m_c of 1.5 GeV/c^2 are also shown.

[23] Proton structure function: Martin-Roberts-Sterling — parametrization A
[24] Photon structure function: Glück-Reya-Vogt — higher order

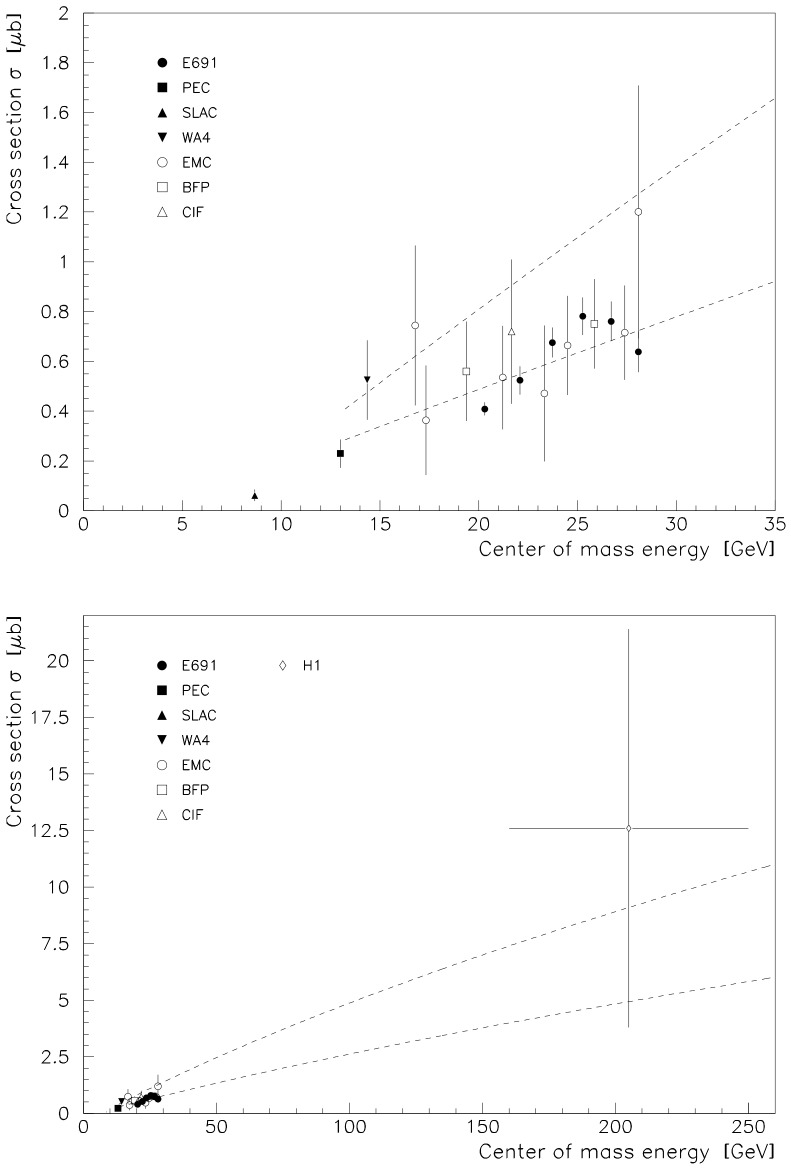

Figure 52: The total cross section for the photoproduction of a pair of charm quarks versus center of mass energy $\sqrt{s}$. The band represents the cross section calculations of Frixione *et al.* [77] with the proton structure function MRSA [78] and the photon structure function GRV-G HO [74] for the charm-quark mass m_c of 1.5 GeV/c^2. The band width is obtained by varying the renormatization scale μ between $m_c/2$ and $2m_c$. The data points are taken from the following references: E691 [22], PEC [23], SLAC [24], WA4 [25], EMC [26], BFP [27], and CIF [28]. The WA4 result is the inclusive cross section for D^0 production. The CIF data and the EMC data at 16.8 GeV, 23.3 GeV, and 28.1 GeV center of mass energies are inclusive cross sections for $D^0(\bar{D}^0)$ production.

9 Summary

The measurement of the production cross section of charm quarks presented in this analysis is based on tracks measured with the central jet chambers of H1. The data analyzed correspond to a total integrated luminosity of 319 nb^{-1} and was taken in the run period of 1993.

The determined value for the charm production cross section is

$$\sigma\,(ep \longrightarrow ec\bar{c}X) \quad = \quad 1.62 \pm 0.87_{\mathrm{stat.}} \pm 0.62_{\mathrm{syst.}}\ \mu\mathrm{b} \quad . \tag{149}$$

This value is in agreement with the theoretical calculation of the perturbative QCD made by Ellis and Nason [14].

The γp cross section can be determined for a certain center of mass energy range of the γp system from the ep cross section. For the range of

$$160\ \mathrm{GeV} \quad < \quad W_{\gamma p} \quad < \quad 250\ \mathrm{GeV} \tag{150}$$

the photon flux factor is integrated over the corresponding y range Q^2 range. A value of

$$\int_{y_{\min}}^{y_{\max}} F_{\gamma/e}\,(y)\ \mathrm{d}y \quad = \quad 0.0256 \tag{151}$$

is obtained. With this value the cross section of photoproduction of a pair of charm quarks is calculated for the center of mass energy (150) of the γp system

$$\sigma\,(\gamma p \longrightarrow c\bar{c}X) \quad = \quad 12.6 \pm 7.1_{\mathrm{stat.}} \pm 5.2_{\mathrm{syst.}}\ \mu\mathrm{b} \quad . \tag{152}$$

This value is compared with fixed target experiments which measure at a lower center of mass energy of the γp system. The result (152) is a factor of two higher than from the Monte Carlo calculations expected.

Appendix

A Pipeline

Figure 53 explains the basic principles of a pipelined trigger. The digitized data are fed into a pipeline, a serial-in-serial-out shift register. If the setup and the hold times, the time the data has to be stable at the input of a flip-flop before and after the relevant clock edge, are short in comparison to the time between two consecutive clock edges, logic circuits may be included between any two registers of the pipeline. If the pipeline is long enough, these logic circuits can sum up the whole trigger logic, delivering the L1-Keep signal. This signal is used to gate the clock of the pipeline of the original digital detector data. At a L1-Keep signal the readout starts and will find the data corresponding to the trigger decision in the last register of the stopped data pipeline. If no trigger occurs, the pipelines keep running and a decision of the next bunch crossing is delivered one clock cycle later.

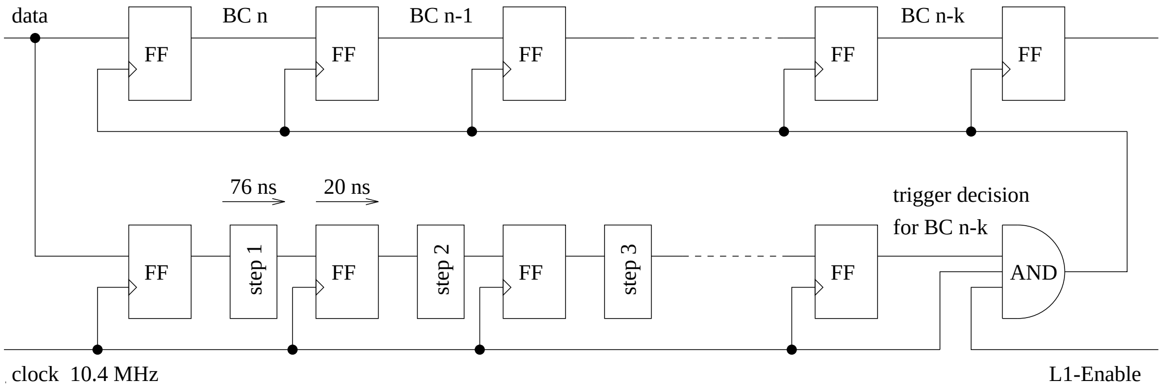

Figure 53: Scheme of a pipelined trigger. The logic functions of the pipelined trigger are distributed between the registers of the shift register. The L1-Enable signal is the inverted L1-Keep signal and stops the shifting of the pipeline.

For the drift chamber r-φ trigger the scheme is more complicated because the trigger logic has to wait for all information from the drift chambers. In addition it needs information from several bunch crossings to make a decision. To save decision time the data are not shifted at each clock edge. This is possible as long as the information belonging to a bunch crossing is kept together. As soon as the information of two consecutive bunch crossings starts to overlap due to propagation delays within the logic circuits, it has to be divided by a synchronization step.

The pipeline structure used in the drift chamber r-φ trigger is a serial-in-parallel-out shift register and is shown in Figure 54.

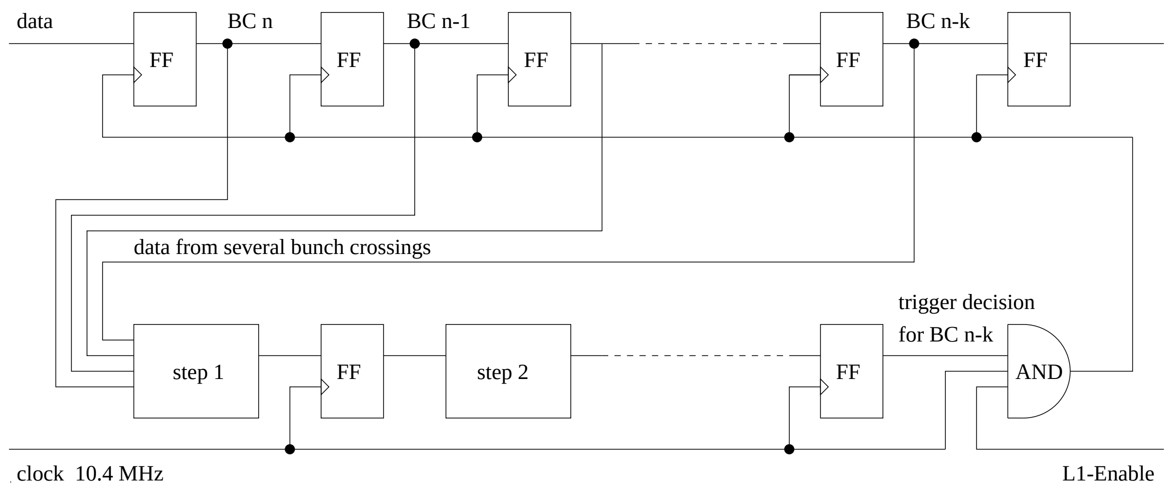

Figure 54: Scheme of the pipeline of the drift chamber r-φ trigger. The logic functions of the trigger are distributed between the registers of the shift register. To save time some of the registers are missing thus the calculation time of the individual functions can be extended over the time between two consecutive bunch crossings. A further extension is the usage of information of several bunch crossing times. This is a consequence of the long drift time of the central jet chambers. The L1-Enable signal is the inverted L1-Keep signal and stops the shifting of the pipeline.

B Trigger Hardware

B.1 Discriminator

The analog central jet chamber pulses are converted to digital signals by the discriminators mounted on adapter cards, which are plugged into the front of the FADC cards. Because the measurement of the drift distance is done by measuring the drift time, the discriminators need a good time resolution. Therefore the differential signals from both ends of the wire are shaped, amplified and discriminated separately and then 'ORed'. The earlier of the two signal from a wire defines the signal at the output of the discriminator.
The discrimination is carried out in six steps:

- The input signals are decoupled and terminated.

- In the next step the signals are integrated in a RC-term with a resistor $R = 100\ \Omega$ and a capacity $C = 200$ pF. The integration constant τ is 22 ns. This is done to suppress the noise from the FADC cards, which are clocked with 104 MHz to store the analog pulse shapes of the chamber signals.

- The integrated signals are passively differentiated with another RC-term. This time constant τ is 26 ns.

- Due to the input capacity and the feed-back of the amplifier, there is also an active differentiation term. The time constant of the differentiation is 5 ns. The gain depends on the slope of the signal due to the differentiation. For a chamber signal with a rise time of 20 ns the gain is about 7.3.

- In the next step the signal is discriminated. The thresholds are provided from the receiver cards and lie in a range of -1 V to $+1$ V. The output of the discriminator is active so long as the signal is above threshold.

- The last step is a logic OR of the two digital signals, which derive from each end of the wire.

The walk of the whole discriminator system is 6.5 ns for pulses with a height between 50 mV and 1000 mV and a threshold of 50 mV [60] (see also Table 20). The thresholds used during data taking in 1993 were between 35 mV and 40 mV. The walk in the data was therefore smaller than the numbers given in Table 20.

One adapter card consists of discriminators for eight wires. One threshold value is provided from the receiver card for all discriminators on an adapter card.

B.2 Receiver Card

The receiver card consists of the synchronization, the logic to control the thresholds for the discriminators and the logic to provide test patterns for the trigger system.

threshold	[mV]	50	50	50	50	50	50	50	50	50
pulse height	[mV]	50	100	150	200	300	400	500	750	1000
time difference	[ns]	+1.5	0	−1	−2	−2.5	−3	−3.5	−4	−5

Table 20: Measurement of the time shift of the discriminator output as a function of the pulse height for a fixed threshold of 50 mV [60]. The time shift is normalized to the time shift of a pulse with a pulse height of 100 mV.

The signals from the adapter cards are distributed to the receiver cards over 150 twisted pair cables each with 26 lines. As well as the discriminated chamber signals, the thresholds and also the ground lines are transferred over this cable.

The threshold can be steered over the VME interface. A digital to analog converter (DAC) provide a voltage between −10 V and +10 V. With a potentiometer the voltage is lowered by a factor of ten to the working region −1 V to +1 V, which is transferred to the discriminators. This voltage can be steered in steps of about 1 mV. The accuracy of the DAC is much better, but the whole system is stable only to 1 mV.

Each receiver card has 29 input signals from the chambers. With a jumper bar it is possible to exchange any combination of two channels. At the same place, unused cable lines from the adapter cards to the receiver card are terminated. There is also the possibility to introduce delay lines for groups of wires, which belong to the same cable, to compensate for different propagation delays through the cables. Until now they have not been used.

The synchronization is done in XILINX logic cell arrays (LCA). The receiver card is fed with a 10.4 MHz clock from the clock card. On the board the clock frequency is doubled. Both the 10.4 MHz as well as the 20.8 MHz clock are used in the LCA to synchronize the 29 input signals according to their layer as shown in Table 12. The logic circuit of the synchronization is shown in Figure 55.

The digital chamber signals are synchronized with the 10.4 MHz or 20.8 MHz clock. The output is a signal, which is only 96 ns or 48 ns long corresponding to the synchronization frequency. Also pulses shorter than a clock period are synchronized and are not lost. Only if there are two pulses in a clock period will they be lost. But this is most unlikely due to the integration time before the discrimination. After a synchronized signal has been produced the channel is dead for the time the analog signal is above threshold.

The synchronization time varies slightly between the different channels on the receiver card. This is due to propagation delays of the signals and the clocks on the card. Also a shift between the 10.4 MHz and the 20.8 MHz clock resulting from the clock doubling gives a similar contribution. To quantify this variation the time difference between the significant edge of the input signal and the significant edge of the synchronized output signal of one channel was measured. This measurement was done for each channel with the same input signal which had a fixed phase difference to the synchronization clock. The measured time differences for each channel are given in Table 21. The time differences are normalized to their mean value. In Figure 56 the distribution

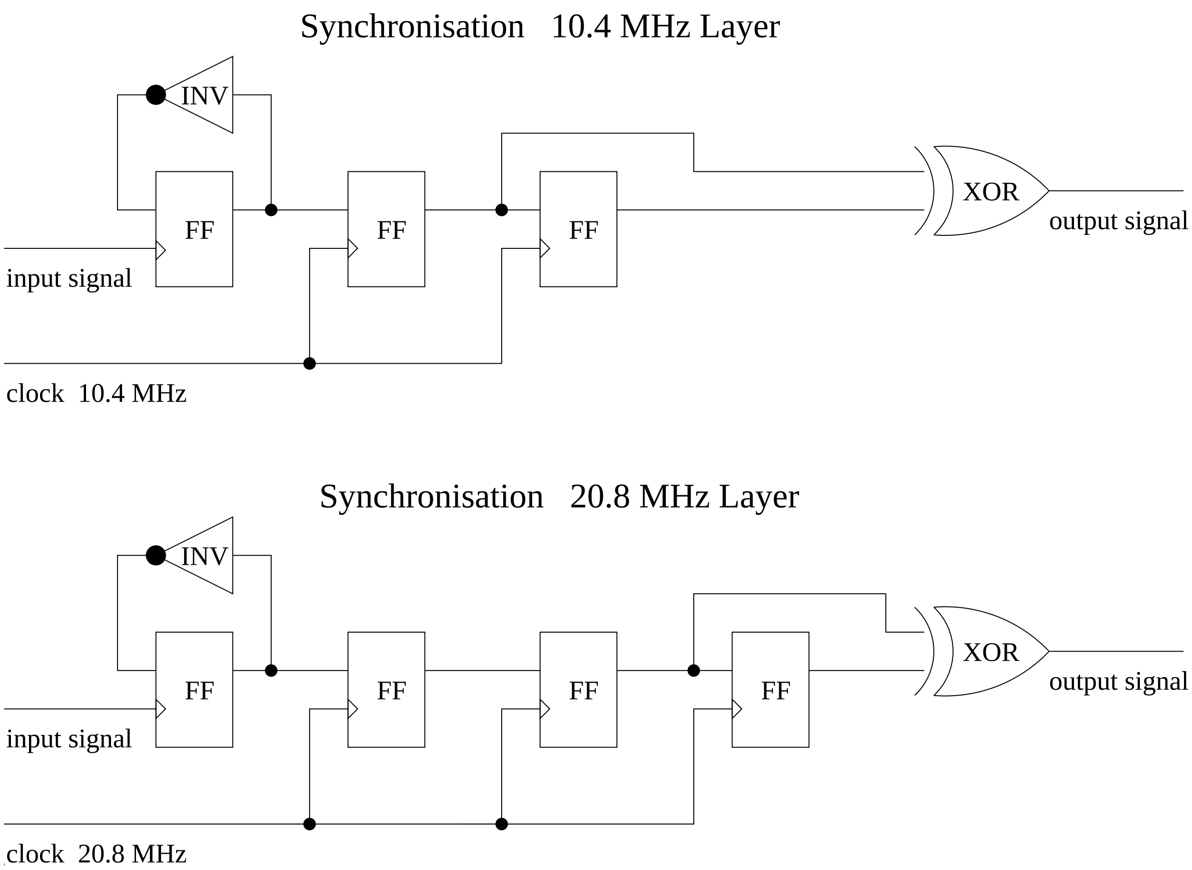

Figure 55: Logic circuit of the synchronization for layers synchronized at 10.4 MHz and 20.8 MHz. To achieve the same propagation time for the signals synchronized at 10.4 MHz and 20.8 MHz the 20.8 MHz synchronization needs an additional flip-flop.

of the measured values is shown.

It is possible to switch off single wires permanently. Broken or noisy wires can be masked this way.

Another major part on the receiver card is the logic to provide the trigger with test patterns. The patterns are stored in four memories, containing 8 bits, with 12 address inputs. They can be loaded over the VME interface. 29 of these 32 bits are used for the 29 wires each receiver card processes. The time information is stored with the addresses. During a test run the addresses of the memories are increased every 96 ns and a new pattern is fed into the trigger. The address counters are started simultaneously in all receiver cards. Due to the 12 address lines of the memories, it is possible to store 4096 bunch crossings for all 29 wires on each receiver card.

The patterns are fed into the trigger after the synchronization. This is a disadvantage, because the phase to the 10.4 MHz clock is different for signals originating form patterns and from chamber hits when they leave the receiver card or arrive on the SRL1 card respectively. In a new design this should be changed.

channel	1	2	3	4	5	6	7	8
time difference [ns]	−0.6	0.6	4.5	0.2	0.7	0.5	−3.1	−1.2
channel	9	10	11	12	13	14	15	16
time difference [ns]	−2.0	−2.3	−2.0	−3.3	−3.7	−3.1	3.3	−3.3
channel	17	18	19	20	21	22	23	24
time difference [ns]	−0.7	8.1	1.1	−0.5	−0.7	−1.4	−0.9	1.5
channel	25	26	27	28	29			
time difference [ns]	2.5	−1.6	−2.3	5.7	3.7			

Table 21: Measurement of the synchronization time as a function of the 29 channels of a receiver card. The differences are due to propagation delays on the card and in the XILINX LCA. The channels 1, 3, 17, 19, 24, 25 ,28, and 29 are synchronized with 20.8 MHz.

The memories storing the patterns are too slow to allow the addresses to be changed every 48 ns. Therefore the 20.8 MHz layers cannot be tested completely, because there are always two 48 ns bits generated instead of one bit. This can be solved easily by exchanging the memories for faster ones.

B.3 SRL1 Card

The SRL1 card is the heart of the drift chamber r-φ trigger, because it contains the track finding logic. The card is a printed circuit board of 14 layers of size 36 cm $\times$ 46 cm. It consists of the following parts:

- data pipelines.
- track finding logic.
- readout logic.
- VME interface to load the configuration of the XILINX chips.
- control logic for the XILINX chips.

The SRL1 card has to be programmable because the track finding logic has to be adjustable to changing chamber conditions. Therefore XILINX logic cell arrays (LCA) are chosen to implement the logic.

Each of the 15 SRL1 cards process a 15^{th} of the φ plane. The card has 92 input signals from the receiver cards which are stored in as many pipelines with parallel outputs. The pipelines are 24 clock cycles deep. The first part is used for waiting for the maximum drift time and is fed the track finding logic. In the second part the information is stored until a trigger decision is taken. In the case of a positive decision, the pipeline is stopped and the corresponding data are ready to be read-out and can be used for a level 2 trigger or for debugging purposes to verify this decision.

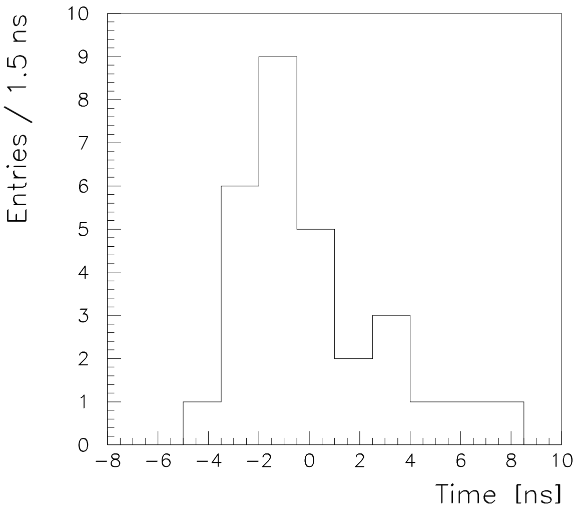

Figure 56: Distribution of the synchronization time in the receiver cards. The time differences are normalized to their mean value.

The shift registers are implemented in 39 XILINX LCAs. There are two kinds of shift registers because of the two synchronization frequencies in the receiver cards. Corresponding to their synchronization the data are shifted in pipelines with a frequency ν of 10.4 MHz or 20.8 MHz. To avoid a 20.8 MHz clock line the 20.8 MHz shift registers are derived from two 10.4 MHz shift registers which are shifted against each other by 48 ns. Because the track finding algorithm is clocked with 10.4 MHz, the 20.8 MHz shift registers have to be synchronized at their parallel outputs with flip-flops with a frequency ν of 10.4 MHz. To have the same propagation delays for all shift registers, the 10.4 MHz shift registers are also synchronized at their outputs. The outputs in the second part of the shift registers are not synchronized but gated, because the clock already has stopped when they are read-out. Parts of the shift register layout are shown in Figure 57.

The outputs of the first part of the shift registers, containing the information of the last 960 ns of the drift chamber, put up the bit map the track finding logic is using. To reduce the bit map some parallel outputs of the pipelines are 'ORed' together in the shift register LCAs. These are mostly the outer 20.8 MHz shift registers, because the granularity is not needed for the first level trigger. So in layers 20 and 29 always two bits are 'ORed' together, and in layer 31 even three bits.

The track finding logic is implemented in two times 21 XILINX LCAs. Each of the 21 LCAs are processing a 30^{th} of the azimuth plane. The roads for the positively or negatively charged particles of two reference wires are always implemented in a LCA. Only the roads of the reference wires 2 and 3 are placed in 3 LCAs due to the many roads. Each LCA has three outputs for found tracks, each one for the high and the low transverse momentum range and one for the time information. In the XILINX LCA for each road, four of the inner five drift bits and four of the outer five drift bits are searched. If a whole road is found, the corresponding transverse momentum bit of the road is set. If the reference bit is also found the time information bit is set. This information is given to the two XILINX LCAs which are called the local clustering unit.

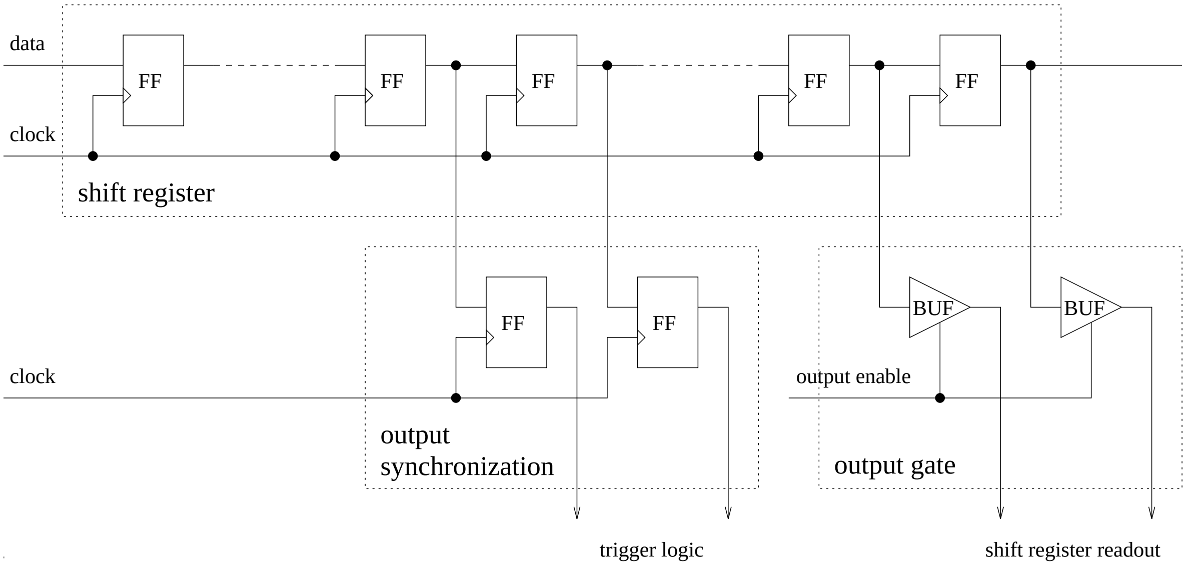

Figure 57: Schematic view of the shift register, the output synchronization for the trigger logic and the output gates for the shift register readout.

The roads of the positively and negatively charged particles are clustered separately to three azimuth ranges and two curvature ranges. In addition the time information is collected. The 14 signals are transferred as the output of the SRL1 cards over the passive backplane to the L1L2 card every 96 ns.

The track finding logic depends strongly on the central drift chamber parameters drift velocity and Lorentz angle. The SRL1 cards are built such that they can adapt to at least 10 % changes from the design parameters of the drift chamber. A change in both parameters has about the same effect; the maximum drift time of the chamber changes. A problem occurs if the maximum drift time exceeds a certain value. The whole information of the drift chamber is spread over a longer time period and the pipelines get too short to store all information and inefficiencies occur.

The XILINX LCAs are loaded by a bit stream from the control program over a VME connection. The chips provide a pin with the information of their state. If they are still programmed the output of this pin is high. This signal from all XILINX LCAs is collected together into one signal and made visible by a LED on the front plate. This information can also be read-out and is monitored by the control program.

B.4 L1L2 Card

The L1L2 card controls the whole trigger. It obtains all control signals from the STC crate and provides the output for the central level 1 trigger (CTL1). It stores all data from the trigger and gives the front end processor permission to read-out the data for the central data acquisition (CDAQ). It is of the same size as the SRL1 card and is made from 9 printed circuit board layers. The card consists of the following parts:

- data memory.

- trigger element logic.
- trigger control unit.
- connection to the CTL1.
- connection to the CDAQ.
- connection to the higher level triggers.
- VME interface to load the configuration of the XILINX chips.
- control logic for the XILINX chips.

The L1L2 card receives the 210 trigger bits from the SRL1 cards. The bits are stored in the data memory. At the same time they are passed over a row of connectors to the L2L3 card and are processed in XILINX LCAs to obtain the trigger elements. Therefore the data are processed in two different paths. One is calculating the multiplicities the other the topology of the event. To get the multiplicities of the event the data are fed to four XILINX LCAs for each transverse momentum range separately. There the 45 azimuth ranges are added. These numbers are sent to another XILINX LCA, which calculates the multiplicities listed in Table 22. To find the topology of the event the data are fed to four other XILINX LCAs. This time three azimuth ranges are collected together. In this granularity of 15 segments any possible topology can be programmed. This calculation is done in a further XILINX LCA. In addition in a third path the time information bits are collected in a XILINX LCA. The multiplicity outputs are compared with thresholds loaded over the control program and stored in registers. There outputs are passed to an analog switch box as well as to the other trigger elements. The L1L2 card provides 16 different trigger elements. They are listed in Table 23. In 1993 only eight lines were connected to the CTL1. With this switch box it is possible to connect every combination of 8 trigger elements to the first 8 output pins and almost every combination to the 16 output pins. This switch box is also programmed by the control program.

A large XILINX LCA controls all processes on the board. It obtains two clock signals from the delay card, one for the processes on the L1L2 card and one for the communication with the SRL1 cards. From the CTL1 over the STC crate it obtains also the L1-Keep signal. All control signals on this board derive from this signal. Over this unit all registers and memories can be accessed. During data taking the card is fed every 96 ns with 210 trigger bits. At every cycle the unit increases the addresses of the ring memory and stores the actual address. After any L1-Keep the data flow is stopped and the unit starts the shift register read-out. It selects a SRL1 card which sends its shift registers in six cycles. After the sixth cycle the next SRL1 card is selected. The bits are stored in the same memory as the trigger bits but in higher addresses. Unfortunately the trigger bits and the shift register bits do not arrive with the same phase relating to the incoming clock. The control unit shifts therefore all relevant signals by 20 ns before the shift register readout starts. The shift register readout takes about 9 μs, almost half of the L2 decision time.

track multiplicities	
tracks with	$p_t > 420$ MeV/c
validated with the corresponding prompt bit of the mask	
tracks with	$p_t > 420$ MeV/c
positively charged tracks with	$p_t > 420$ MeV/c
negatively charged tracks with	$p_t > 420$ MeV/c
tracks with	420 MeV/$c < p_t <$ 800 MeV/c
tracks with	$p_t > 800$ MeV/c
positively charged tracks with	420 MeV/$c < p_t <$ 800 MeV/c
positively charged tracks with	$p_t > 800$ MeV/c
negatively charged tracks with	420 MeV/$c < p_t <$ 800 MeV/c
negatively charged tracks with	$p_t > 800$ MeV/c

Table 22: Track multiplicities calculated by the drift chamber r-φ trigger.

symbol	description
DCRPhi_T0	at least one tracks with $p_t > 420$ MeV/c validated with the corresponding prompt bit of the mask.
DCRPhi_Ta	at least one track with $p_t > 420$ MeV/c.
DCRPhi_Tb	at least two tracks with $p_t > 420$ MeV/c.
DCRPhi_Tc	at least three tracks with $p_t > 420$ MeV/c.
DCRPhi_TPos	at least one positively charged track with $p_t > 420$ MeV/c.
DCRPhi_TNeg	at least one negatively charged track with $p_t > 420$ MeV/c.
DCRPhi_TLow	at least one track with 420 MeV/$c < p_t <$ 800 MeV/c.
DCRPhi_THigh	at least one track with $p_t > 800$ MeV/c.
DCRPhi_TPL	at least one positively charged track with 420 MeV/$c < p_t <$ 800 MeV/c.
DCRPhi_TPH	at least one positively charged track with $p_t > 800$ MeV/c.
DCRPhi_TNL	at least one negatively charged track with 420 MeV/$c < p_t <$ 800 MeV/c.
DCRPhi_TNH	at least one negatively charged track with $p_t > 800$ MeV/c.
DCRPhi_Topo1	two opposite lying tracks, one positively charged, one negatively charged, with six empty sectors between.
DCRPhi_Topo2	two tracks with at least three sectors between.
DCRPhi_Topo3	three tracks with at least somewhere four empty sectors next to each other.
DCRPhi_Topo4	one negatively track and two empty neighbour sectors at both side.

Table 23: Selectable trigger elements provided by the drift chamber r-φ trigger.

After the L2-Keep signal of the CTL1, the front end processor starts to read-out the data from the L1L2 card. For this purpose the control unit changes the access mode of the memories. During data taking all memories were written with 210 bits at the same time. In the readout mode only 16 bits can be read over the VME bus. The control unit selects all memories, one after the other and calculates with the address stored in the register the memory address to get the correct bunch crossing. Due to special steer signals data which belong to bunch crossings before and after the nominal one can only be read-out. Of course it is also possible to read-out the shift register bits.

As well as in the SRL1 card the XILINX LCAs are loaded by a bit stream over a VME connection and the status of the chips is visible on a LED and is monitored by the control program.

B.5 Readout Control Chip

The readout control chip on the L1L2 card controls the transfer of the data from the SRL1 cards to the L1L2 card as well as their readout over the VME bus. In addition it provides all control signals, which are necessary to steer the trigger settings on the L1L2 card. The logic is implemented in a XILINX LCA.

The control chip has the following input signals:

- 19 addresses from the VME bus.
- 6 address modifiers from the VME bus.
- 16 data lines from the VME bus.
- 10.4 MHz clock.
- L1-Keep signal.

It has the following output signals:

- 25 latch signals.
- 14 memory select signals.
- 4 cell signals.
- 6 cycle signals.
- 13 RAM address lines.
- Read/$\overline{\text{Write}}$ signal.
- Backplane enable signal.
- Trigger bit read signal.

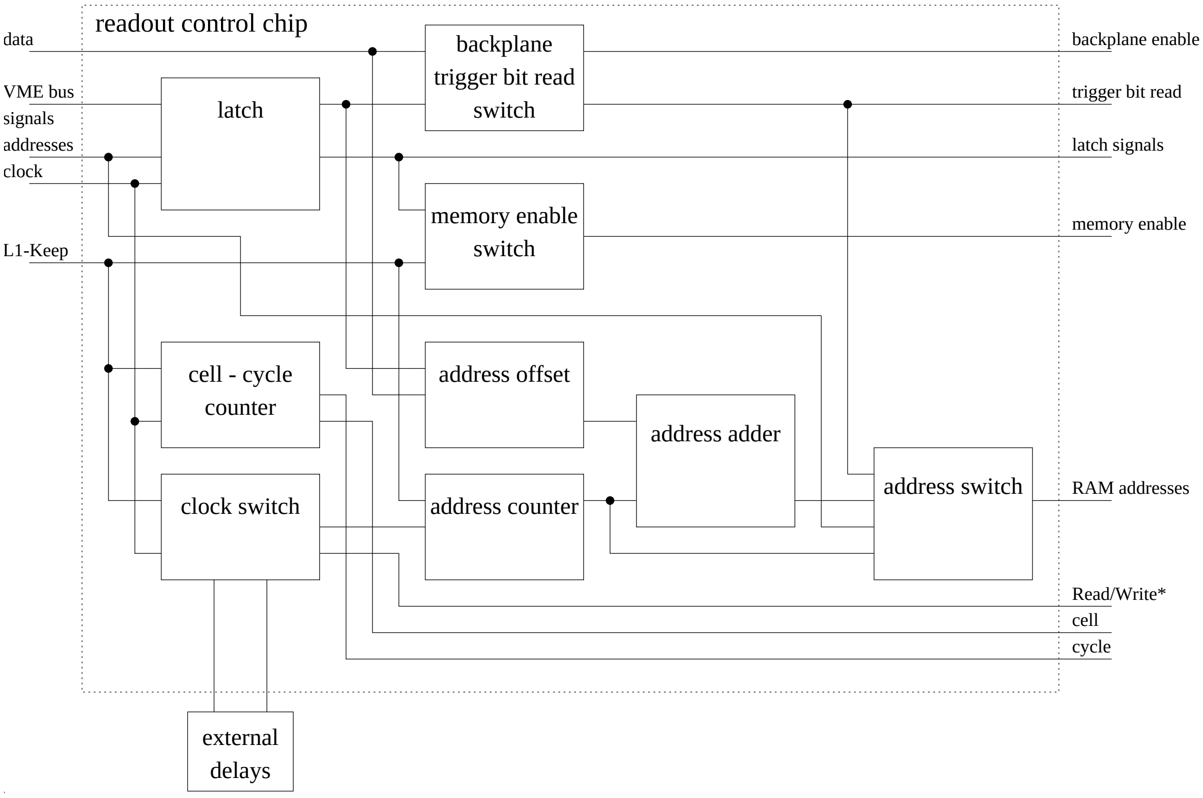

Figure 58: Schematic overview of the readout control chip. The input signals are fed from the left side. The output signals provided by the readout control chip are shown on the right side.

In addition there are four input lines and four output lines, which are connected by adjustable delay lines on the board to shift clock signals in units of 10 ns. A schematic overview of the readout control chip is given in Figure 58.

With the latch signals, which are controlled by the least significant addresses and the data lines, the backplane can be enabled, the readout mode can be selected and an address offset can be stored. The backplane has to be disabled during loading the XILINX LCAs. The address offset is needed to indicate the correct address where the 210 trigger bit readout has to start.

During triggering, before a L1-Keep signal occurs, the chip provides the addresses and the Read/$\overline{\text{Write}}$ signal for the memories where the 210 trigger bits for each bunch crossing are stored. The addresses are produced by the RAM clock. The Read/$\overline{\text{Write}}$ signal and the RAM clock are fed through two of the four external delay lines. Due to the 210 bits wide data bus from the SRL1 cards to the L1L2 card all memories are enabled and written at the same time. The actual written memory address is stored as pointer to the memory address at occurrence of a L1-Keep signal.

After a L1-Keep signal the pipeline is stopped and the control chip starts the shift register readout. The RAM clock and the Read/$\overline{\text{Write}}$ signal are shifted by 20 ns using the other two external delay lines. This step is taken because the trigger bits and the shift register bits arrive with different phases relating to the incoming clock. Again all memories are enabled and written at the same time. With the cell signals the SRL1 cards are selected for the shift register transfer. With the cycle signals six cycles are counted before the next SRL1 card is selected.

At the SRL1 card the cell signals are fed in a shift register, which generates five output enable signals (see Figure 57). The sixth cycle is a dummy cycle, which is needed to select the next SRL1 card.

After the L2-Keep signal the front end processor is allowed to read-out the transferred data on the L1L2 card. It selects the readout mode with the trigger bit read signal. In the trigger bit readout mode the control chip calculates the correct memory address by subtracting the stored address offset from the stored last written address, and selects the correct memory. Due to the 16 data lines of the VME bus only two memories can be read-out at the same time. For the shift register readout the front end processor has to change the readout mode. In this mode the processor can access the memories directly. No address calculation is needed because the shift register bits are always stored at the same addresses.

B.6 L2L3 Card

The L2L3 card is the interface between the drift chamber r-φ trigger and the higher level triggers. It passes the 210 trigger bits to the PQZP bus system, which distributes the bits to the L2 triggers and to the L3 processor memory. It would also be possible to transfer the shift registers, which arrive later in the data stream, to the higher level trigger, but the amount of data would cause too large dead times. The card is of the same size as the L1L2 card and is connected to it by four 96 pin connectors. The card provides as output the 210 trigger bits as differential ECL signals to be compatible with the PQZP bus system. The signals are passed over 14 twisted pair flat cables with 40 conductors in each. Because there is no -5.2 V voltage in this crate the card has three DC-DC converters[25] to transform $+5$ V to -5.2 V. It is possible to pass the 210 trigger bits over another row of four 96 pin connectors to a printed circuit board yet to be designed which can extend the trigger.

B.7 Delay Card and Clock Card

The delay card provides the receiver cards, the SRL1 card and the L1L2 card with clock signals, one clock line for every receiver crate and two clock lines and the L1-Keep signal for the L1L2 card. One of the clock lines is passed through the L1L2 card over the passive backplane to the SRL1 cards. The other clock is used on the L1L2 card itself. The delay card gets the signals from the fanout card for the drift chamber r-φ trigger. As already mentioned the time of synchronization is very important for the performance of the trigger. In the receiver crates, the time of synchronization has to be shifted with respect to the collision time in the SRL1 cards and L1L2 card to take over properly the bits from the previous cards. So the card was upgraded from 1992 to 1993 to steer all delays in steps of 2 ns. The steering is done over a VME interface.

[25] Direct Current - Direct Current converter

In the receiver crates the clock signal is taken over by the clock card, which splits the line into five. Each of them feeds three receiver cards with a clock over wire-wrapped lines on the backplane to avoid different propagation delays to the several receiver cards.

C XILINX Logic Cell Arrays

XILINX logic cell arrays (LCA) are fully programmable chips. They are based on a number of input/output blocks (IOB) associated with pins and configurable logic blocks (CLB). The IOBs are located peripherally, the CLBs on a matrix in the center of the chip. All these blocks can be connected with each other by several types of programmable routing sources.

The configuration of the chip is stored in a kind of static RAM lying underneath the user-visible collection of CLBs, IOBs and interconnections. A sketch of such a layout of a LCA is given in Figure 59.

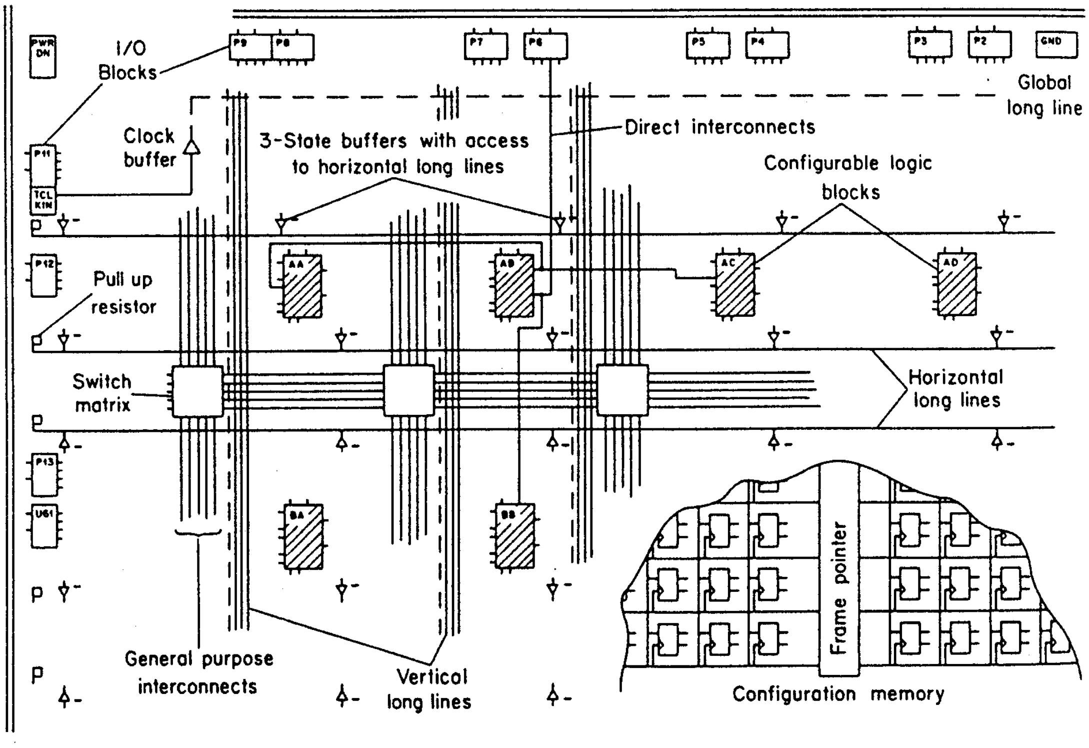

Figure 59: XILINX logic cell array (LCA) [61]. The functionality of the configurable logic blocks and interconnections in a XILINX LCA can be programmed by an appropriate configuration bit stream into the underlying memory.

The chips used for this trigger belong to the XILINX 3000 series. Table 24 gives an overview of the available devices. All of them are available in different packages and speed grades.

There also exist a XILINX 2000 series with slightly simpler structure and a XILINX 4000 series with significantly more interconnect resources.

Each CLB has a structure as shown in Figure 60. The five inputs are fed to a combinatorial block with two feed-back lines Q_x and Q_y. The function F and G are either equal, in which case they can provide any function of five of the seven inputs, or independent functions of almost any set of four input variables. There also two

device	number of gates	number of CLBs	number of IOBs	number of program data bits
XC3020	2000	64	64	14779
XC3030	3000	100	80	22176
XC3042	4200	144	96	30784
XC3064	6400	224	120	46064
XC3090	9000	320	144	64160

Table 24: Available devices of the XILINX 3000 series [61].

registers, which can operate either as flip-flop or as latches. They get their inputs from D_{in}, F or G. The outputs X and Y can be programmed to be either Q_x or F and Q_y or G respectively.

The IOBs are also programmable either to be input, output or bi-directional connection with tri-state output. The polarity is selectable. The implemented register can be programmed to be either a flip-flop or a latch. The characteristic of the input can be selected to be either CMOS or TTL compatible. Some IOBs may not be connected to an external pin, depending on the package used, in which case they can be used as an internal register.

Each CLB has direct interconnections to its four intermediate neighbouring CLBs. These are very high-speed links with only one switch transistor (programmable interconnect point, PIP) in between. There are three vertical long-lines between any two columns of CLBs. In larger LCAs two of them are split into connectable half-length lines. Horizontally there are two long-lines crossing the entire die between any rows of CLBs. Tri-state buffers connected to them allow busses to be implement. These long-lines allow signals to travel fast over a greater distance. An additional global long-line can be connected to all clock inputs of all CLBs and IOBs to allow a fast clock distribution over the entire chip. Five general purpose interconnect lines run between any two columns and rows of CLBs. At the crossing points switch matrices allow almost any desired connectibility.

The XILINX chips are available in speed grades of 50 MHz, 70 MHz, 100 MHz and 125 MHz. The maximum delay through a CLB gets smaller with higher speed grades. So values from 14 ns for 50 MHz chips down to 7 ns for 125 MHz chips can be achieved. Due to the delay occurring on the signal interconnections and the various switching transistors, a propagation delay estimate was found to be 20 ns per CLB for a 70 MHz version.

As the configuration memory of the XILINX consists of static RAM, it needs reloading after each power cycle. Several procedures are possible. The least flexible one uses serial ROM connected to the XILINX. Upon power up, all necessary steering signals are provided from the XILINX to read its configuration from the ROM. For the drift chamber r-φ trigger the ability to change the configuration is desirable. For such applications the chips can be loaded by a bit stream over a computer interface. The configuration bit streams of the XILINX chips are stored as files on the hard disk of a

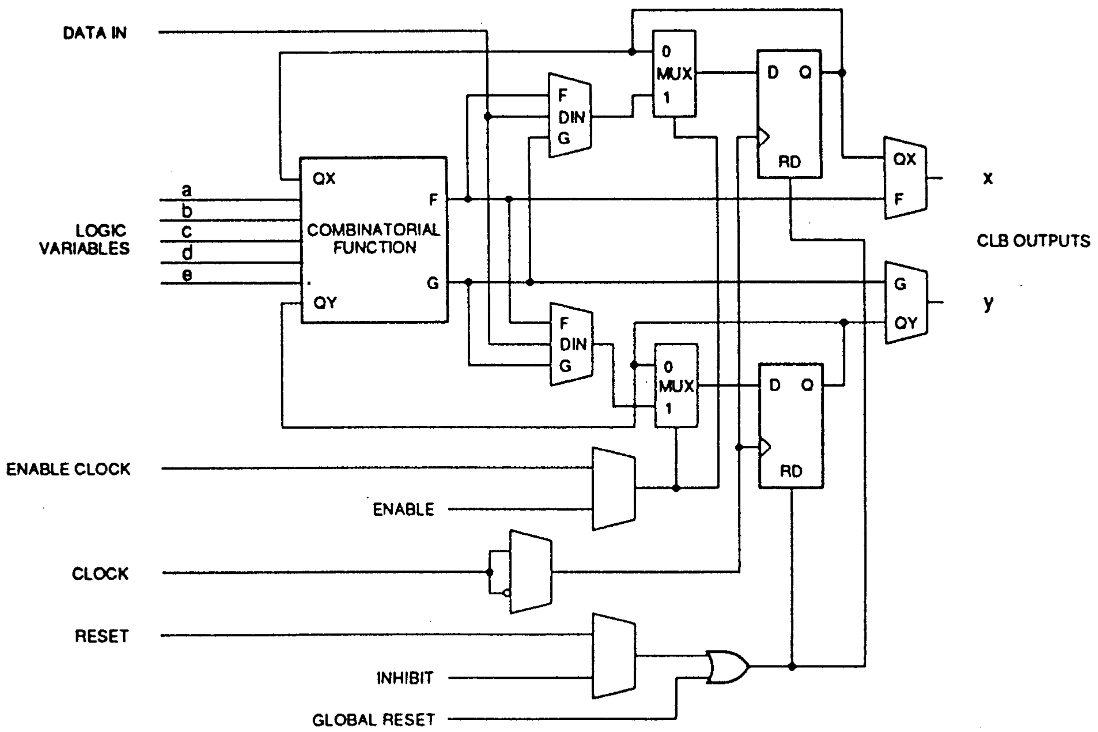

Figure 60: Configurable logic block (CLB) [61]. It can be programmed to perform any function of the five input variables. Two output registers are available.

computer and can be downloaded after deleting the old configuration.

D Error Calculation of Efficiencies

The efficiency ϵ is usually determined from a data sample of N events of which n pass the user's criteria as

$$\epsilon = \frac{n}{N} \quad . \tag{153}$$

This is incorrect. If one assumes the exact efficiency to be ϵ then the probability to observe n accepted events becomes a Binomial distribution

$$P_\epsilon(n) = \begin{pmatrix} n \\ N \end{pmatrix} \epsilon^n (1-\epsilon)^{N-n} \quad . \tag{154}$$

For an accepted number of events n_{obs} one can define the probability distribution for the efficiency ϵ as follows

$$\epsilon \equiv \frac{n_{\mathrm{obs}}}{N} \tag{155}$$

$$P(\epsilon) = \frac{P_\epsilon(n_{\mathrm{obs}})}{\int_0^1 \mathrm{d}\epsilon\, P_\epsilon(n_{\mathrm{obs}})} \quad . \tag{156}$$

Using

$$\int_0^1 \mathrm{d}x\, x^n (1-x)^m = \frac{n!\, m!}{(n+m+1)!} \tag{157}$$

one gets for the averaged value of ϵ

$$\overline{\epsilon} \equiv \int_0^1 \mathrm{d}\epsilon\, \epsilon P(\epsilon) = \frac{n+1}{N+2} \quad . \tag{158}$$

And similarly for the average of ϵ^2

$$\overline{\epsilon^2} \equiv \int_0^1 \mathrm{d}\epsilon\, \epsilon^2 P(\epsilon) = \frac{\int_0^1 \mathrm{d}\epsilon\, \epsilon^{n+1}(1-\epsilon)^{N-n}}{\int_0^1 \mathrm{d}\epsilon\, \epsilon^n (1-\epsilon)^{N-n}} = \frac{(n+2)(n+1)}{(N+3)(N+2)} \quad . \tag{159}$$

And hence for the standard deviation σ_ϵ

$$\sigma_\epsilon \equiv \sqrt{\overline{\epsilon^2} - \overline{\epsilon}^2} = \sqrt{\frac{n+1}{N+2}\left(\frac{n+2}{N+3} - \frac{n+1}{N+2}\right)} = \sqrt{\frac{(n+1)(N-n+1)}{(N+3)(N+2)^2}} \quad . \tag{160}$$

List of Figures

List of Tables

References

[1] J.D. Bjorken, Phys. Rev. 163 (1967) 163.

[2] A. Blondel and F. Jacquet, Proc. of "Study of an ep Facility for Europe", Ed. U. Amaldi, DESY-79-48 (1979) 391.

[3] J.J. Sakurai, Ann. Phys. 11 (1960) 1;
M. Gell-Mann and F. Zachariasen, Phys. Rev. 124 (1961) 953;
T.H. Bauer *et al.,* Rev. Mod. Phys. 50 (1978) 261.

[4] G. Wolf and P. Söding, in "Electromagnetic Interactions of Hadrons", Eds. A. Donnachie and G. Shaw, Vol. 2, p. 1, 1978.

[5] C.F. Weizsäcker, Z. Phys. 88 (1934) 612;
E.J. Williams, Phys. Rev. 45 (1934) 729.

[6] H1 Collaboration, T. Ahmed *et al.,* Phys. Lett. B299 (1993) 374.

[7] ZEUS Collaboration, M. Derrick *et al.,* DESY-94-032 (1994).

[8] A. Donnachie and P.V. Landshoff, CERN-TH 6635 (1992).

[9] H. Abramowicz *et al.,* Phys. Lett. B269 (1991) 458.

[10] G. Ingelman *et al.,* in Proc. HERA Workshop, Ed. R.D. Peccei, DESY, Hamburg (1988), Vol. 1, p. 3.

[11] C.D. Callan and G. Gross, Phys. Rev. Lett. 22 (1969) 156.

[12] J. Blümlein *et al.,* in Proc. HERA Workshop, Ed. R.D. Peccei, DESY, Hamburg (1988), Vol. 1, p. 67.

[13] A.M. Cooper-Sarkar, R.C.E. Devenish and M. Lancaster in Proc. HERA Workshop, Eds. W. Buchmüller and G. Ingelman, DESY, Hamburg (1991), Vol. 1, p. 155.

[14] R.K. Ellis and P. Nason, Nucl. Phys. B312 (1989) 551.

[15] R.K. Ellis and Z. Kunszt, Nucl. Phys. B303 (1988) 653.

[16] A. Ali and D. Wyler in Proc. HERA Workshop, Eds. W. Buchmüller and G. Ingelman, DESY, Hamburg (1991), Vol. 2, p. 669.

[17] G.A. Schuler, Nucl. Phys. B299 (1988) 21.

[18] S. Catani, M. Ciafaloni and F. Hautmann, Phys. Lett. B242 (1990) 97;
J.C. Collins and R.K. Ellis, Nucl. Phys. B360 (1991) 3.

[19] S. Narison, Phys. Lett. B197 (1987) 405.

[20] W.A. Bardeen *et al.,* Phys. Rev. D18 (1978) 3998; W.A. Bardeen and A.J. Buras, FERMILAB-PUB-79/31-THY, (1979).

[21] M. Diemoz *et al.,* CERN-TH 4751, 1987;
J.V. Allaby *et al.,* Phys. Lett. B197 (1987) 281.

[22] TPS Collaboration, J.C. Anjos *et al.,* Phys. Rev. Lett. 62 (1989) 513.

[23] Photo Emulsion Collaboration, M.I. Adamovich *et al.,*
Phys. Lett. B187 (1987) 437.

[24] SFH Photon Collaboration, K. Abe *et al.,* Phys. Rev. D33 (1986) 1.

[25] WA4 Collaboration, D. Aston *et al.,* Phys. Lett. B94 (1980) 113.

[26] EMC Collaboration, J.J. Aubert *et al.,* Nucl. Phys. B213 (1983) 31;
EMC Collaboration, J.J. Aubert *et al.,* Phys. Lett. B167 (1986) 127.

[27] BFP Collaboration, A.R. Clark *et al.,* Phys. Rev. Lett. 45 (1980) 682.

[28] CIF Collaboration, M.S. Atiya *et al.,* Phys. Rev. Lett. 43 (1979) 414.

[29] M. Drees and K. Grassie, Z. Phys. C28 (1985) 451.

[30] NA14/2 Collaboration, M.P. Alvarez *et al.,* Z. Phys. C60 (1993) 53.

[31] Particle Data Group, L. Montanet *et al.,* Phys. Rev. D50 (1994) 1173.

[32] CLEO Collaboration, P. Avery *et al.,* Phys. Rev. D43 (1991) 3599.

[33] CLEO Collaboration, B. Bortoletto *et al.,* Phys. Rev. D37 (1988) 1719.

[34] CLEO Collaboration, J.P. Alexander *et al.,* Phys. Lett. B303 (1993) 377.

[35] ALEPH Collaboration, D. Decamp *et al.,* Phys. Lett. B266 (1991) 218.

[36] ZEUS Collaboration, "The ZEUS Detector",
Status Report 1993, DESY, Hamburg (Feb. 1993).

[37] H1 Collaboration, I. Abt *et al.,* DESY-93-103 (1993).

[38] HERA-B Collaboration, T. Lohse *et al.,* DESY Internal Report,
DESY-PRC 94-02 (1994).

[39] HERMES Collaboration, DESY Internal Report, DESY-PRC 93-06 (1993).

[40] P. Robmann, Ph.D. Thesis, University of Zürich, unpublished, 1994.

[41] K. Müller *et al.,* Nucl. Instr. Meth. A312 (1992) 457.

[42] J. Bürger *et al.,* Nucl. Instr. Meth. A279 (1989) 217.

[43] K. Müller, Ph.D. Thesis, University of Zürich, unpublished, 1994.

[44] W.J. Haynes, CERN Yellow Reprt, CERN 90-06 (1990);
W.J. Haynes, DESY-92-129 (1992).

[45] H1 Collaboration, DESY Internal Report, DESY-DRC 92-129 (1992).

[46] S.P. Denisov *et al.,* Nucl. Phys. B61 (1973) 62.

[47] A.J. Campbell, Proc. of IEEE 7$^{\text{th}}$ Conf. Real Time, Juelich, Germany (1991), p. 207.

[48] J. Fent *et al.,* H1 Internal Report H1-04/91-172 (1991).

[49] H. Krehbiel, H1 Internal Report H1-09/92-239 (1992).

[50] A. Mavroidis *et al.,* H1 Internal Report H1-08/93-308 (1993).

[51] S. Eichenberger *et al.,* Nucl. Instr. Meth. A323 (1992) 532.

[52] R.A. Eichler *et al.,* H1 Internal Report H1-04/87-61 (1987).

[53] T. Wolff *et al.,* Nucl. Instr. Meth. A323 (1992) 537.

[54] H.J. Behrend and W. Zimmermann, Proc. Int. Conf. on Computing in High Energy Physics, Tsukuba, Japan (1991), p. 237.

[55] E. Brettel *et al.,* MPI Munich Report H1-MPI-140 (1990).

[56] J. Ban *et al.,* H1 Internal Report H1-07/92-235 (1992).

[57] J. Tutas, Ph.D. Thesis, RWTH Aachen, unpublished, 1991.

[58] T. Ahmed *et al.,* Proc. Int. Conf. on Computing in High Energy Physics, Annecy, France (1992).

[59] A.I. Lebedev *et al.,* H1 Internal Report H1-05/88-86 (1988).

[60] T. Wolff, Ph.D. Thesis, ETH Zürich, unpublished, 1993.

[61] XILINX, The programmable Gate Array Company, 2100 Logic Drive, San Jose, CA 95124, USA.

[62] C. Beigbeider and D. Breton, H1 Internal Report H1-02/93-269 (1993).

[63] H. Krehbiel, "The Fast Card of the Subsystem Trigger Controller", User's Manual, unpublished, 1990.

[64] J. Olszowska, "The Slow Card of the Subsystem Trigger Controller", User's Manual, unpublished, 1990.

[65] H. Krehbiel, "The Extended Fanout Card of the Subsystem Trigger Controller", User's Manual, unpublished, 1991.

[66] H. Krehbiel, "The Triggerbits Card of the Subsystem Trigger Controller", User's Manual, unpublished, 1992.

[67] VME Bus Specification, IEEE Standard 1095.

[68] Creative Electronics System SA, VMV Bus One Slot VIC 8250, Geneva, Switzerland, 1990.

[69] Creative Electronics System SA, Fast Intelligent Controller FIC 8330/8232, Geneva, Switzerland, 1987/1992.

[70] I. Abt, H1 Internal Report H1-05/93-290 (1993).

[71] T. Sjöstrand and M. Bengtsson, Comp. Phys. Commun. 43 (1987) 367; H.-U. Bengtsson and T. Sjöstrand, Comp. Phys. Commun. 46 (1987) 43; T. Sjöstrand, CERN-TH-6488 (1992).

[72] Bo Andersson, G. Gustafson and T. Sjöstrand, Phys. Lett. B94 (1980) 211; Bo Andersson *et al.,* Phys. Rep. 97 (1983) 31.

[73] M. Glück, E. Reya and A. Vogt, Z. Phys. C53 (1992) 127.

[74] M. Glück, E. Reya and A. Vogt, Phys. Rev. D46 (1992) 1973.

[75] R. Luchsinger and C. Grab, Comp. Phys. Commun. 76 (1993) 263.

[76] H1 Collaboration, T. Ahmed *et al.,* DESY-95-024 (1995).

[77] S. Frixione *et al.,* CERN-TH-7527 (1994).

[78] A.D. Martin, R.G. Roberts and W.J. Sterling, preprint RAL-94-055, (1994).

Acknowledgments

I am very grateful to all my colleagues of the H1 collaboration. Without them it would not be possible to realize such a work. Especially I would like to thank

- Prof. Dr. Ralph Eichler for giving me the chance to work within the H1 collaboration.
- Prof. Dr. Felicitas Pauss for accepting to be co-examiner.
- Josef Riedlberger for the productive team-work and the many discussions about physics and other subjects.
- Christoph Grab for his support in the analysis through his knowledge and experience.
- Thom Wolff for his extended introduction in electronics and the hours of exciting work in the electronic trailer of the H1 experiment.
- Ueli Straumann for his moral and technical support in critical periods.
- Marco Arpagaus for sharing good and bad times during this work and for the many discussions about all different kind of subjects.
- the part of the H1 collaboration from the University of Zurich, especially Katharina Müller, Peter Robmann, Hanspeter Beck and Christian Dollfus, for the pleasant atmosphere in and outside the office in Hamburg.
- Urs Meyer for his help in designing the logic circuit boards.
- Urs Langenegger and Thomas Schietinger for their support in the analysis.
- my parents for their moral support and Yvonne Negus for her patience and love.

This list is far too short to mention all the friends and colleagues which helped in many ways to get this work completed.

Curriculum Vitae

Name	Roland Bernet
Date of birth	July 5, 1964
Place of birth	Schaffhausen, Switzerland
Nationality	swiss (from Alberswil/LU)

1971-1977	Primary School, Neuhausen
1977-1979	Secondary School, Neuhausen
1979-1984	Kantonsschule Schaffhausen, Schaffhausen
1984	Eidgenössische Matura typus C, Schaffhausen
1984/1985	On service (RS) in Swiss Army
1985-1990	Study of Physics at Abt. IX of the Eidgenössische Technische Hochschule in Zürich (ETH Zürich)
1990	Diploma in Experimental Physics at the ETH Zürich
since 1990	Graduate Education in Experimental Physics at the Eidgenössische Technische Hochschule in Zürich (ETH Zürich)